Three-dimensional image analysis of high resolution confocal microscopy data of the Drosophila melanogaster brain

Chloé Isabelle Murtin

N°d'ordre NNT : 2016LYSE081

THESE de DOCTORAT DE L'UNIVERSITE DE LYON
opérée au sein de l'INSA-Lyon

Ecole Doctorale EEA N° accréditation
Electronique, Electrotechnique et Automatique

Spécialité de doctorat :
Discipline : Ingénierie pour le vivant

Soutenue publiquement le 20/09/2016, par :
Chloé Isabelle Murtin

Traitement d'images de microscopie confocale 3D haute résolution du cerveau de la mouche Drosophile

Devant le jury composé de :

Dieterlen, Alain	PU Université de Haute Alsace	Rapporteur
Daul, Christian	PU Université de Lorraine	Rapporteur
Loménie, Nicolas	MCHDR Université Paris-Descartes	Examinateur
Ito, Kei	PU Université de Tokyo	Co-directeur de thèse
Rousseau, David	PU CREATIS Université Lyon 1	Directeur de thèse
Frindel, Carole	MCU CREATIS INSA Lyon	Co-encadrante
Bessereau, Jean-Louis	DR INSERM, IMNG, Université Lyon 1	Invité
Epicier, Thierry	DR CNRS, MATEIS INSA-Lyon	Invité

TABLE OF CONTENTS

PART 1
ABSTRACT

PART 1 ABSTRACT

The brain has for a long time attracted the fascination of scientists and philosophers. However, as the main organ of our nervous system and due to its extreme complexity, the brain investigation is, even nowadays, a challenge for all neuroscientists. Direct analysis of the human brain is hampered from complex technical and ethical problems, and scientists quickly opted for indirect research using animal models. Among them, the fruit fly Drosophila melanogaster has been one of the most popular to investigate a variety of fields from genomics to neurosciences. Many tools have been developed to manipulate the fruit fly genome, offering opportunities to investigate other fields such as developmental and functional neurosciences leading to many discoveries, which, under certain conditions, can be extrapolated to human research. Those tools include the insertion of transgenic genes to drive or inactivate the expression of proteins in specific cells of the fruit fly. In particular, this technology enables the expression of fluorescent proteins in the cytoplasm or membrane of certain neurons. This fluorescence can be captured by a confocal microscope to reconstruct three-dimensional images of the labeled neurons.

The brain of an adult fruit fly is a complex network of about 100,000 neurons projecting in a 600-µm wide, 300-µm tall, and 160-µm thick volume. Its cell bodies are mainly located at its surface (outer part) whereas the neurites innervate the inner part (synaptic neuropil). The fly brain features a wide variety of neurons that can be categorized by the types of neurotransmitters released in synapses. Among all those categories, we will focus on two specific neuron types: the octopaminergic and dopaminergic neurons and their connections. Octopamine, is an endogenous trace amine exclusively found in invertebrate organisms. In insects, this molecule mediates a wide range of functions. A Drosophila melanogaster brain counts around 100 octopaminergic neurons and their organization is well conserved among invertebrate organisms proving their importance. On the other hand, dopamine is a neurotransmitter and neurohormone found in both vertebrates and invertebrates. This molecule plays major roles in the human brain and body, and dysfunctions of the dopamine system can lead to serious diseases

such as Parkinson's disease or schizophrenia. Octopaminergic and dopaminergic neurons appear to be determinant in the correct operating of the central nervous system and a precise and systematic analysis of their evolution and interaction is necessary to understand its mechanisms.

Interestingly, unlike most other neurons, those two types monoamine neurons feature very complex structures with many thin branches that are densely spread in the whole brain, multiplying the connections with other neurons. Because of this complexity, three-dimensional images of very high resolution (0.2µm square voxels) are necessary to characterize their morphology. Confocal microscopy is a powerful tool that can be used to obtain a stack of serial section images of the signal distribution by illuminating the sample point-by-point within its volume with a laser beam. The fluorescence emitted from each illumination position is recorded as the signal level of each voxel. However, even though the specimens are made sufficiently transparent, they are never completely clear and optically uniform. Thus, the excitation light and the light emitted from the fluorescent objects are attenuated, refracted and scattered by the sample tissue, especially in thick samples. The light coming from deeper parts of the sample is partially affected and the signal is blurred by random refraction and scattering of the light ray, significantly reducing the image quality in those regions because less photons will reach the photodetectors causing a diminution of sensitivity and increase of the noise to signal ratio. Moreover, as the laser beam goes through the sample, the neighboring regions of the focus point are slightly photobleached leading to a diminution of the signal intensity and a loss of contrast. In conclusion the image quality in laser scanning microscopy techniques decreases with the depth from the sample surface and deeper objects appear blurry, sometimes fused with their neighbors if the focal plane is deeper than 100 µm.

Octopaminergic and dopaminergic neuron branches spread in the whole 160µm-thick fly brain, deeper than the 100-µm theoretical limit over which the confocal scanning microscopy image will not be clear enough for high-resolution study. Several workaround techniques have been employed to overcome this problem. Because our specimen is thinner than 200 µm along z-axis, we can record the images from both sides of the samples: from the front toward the center and

from the other side. For taking such set of images, the sample is mounted between two thin cover slips, and the image stacks are captured from both sides by flipping the sample after the first scan. Both image volumes must be a little bit thicker than half of the brain to ensure overlap of the two stacks. Using these overlapping sections from both images as a guide, they can be concatenated, or stitched. Although various programs have been developed for stitching such volume data, they compensate only translation and rotation around the optical axes (z). Straightforward concatenation is often not possible, because the small rotations that occur when the sample is flipped involves not only the rotation around the z axis but also around x and y (tilting). Before stitching the front and back stacks, they must be registered in such a way that each neuronal fiber appears contiguous at the boundary of the two stacks, because a gap in the final image will affect neuron tracing and further study.

To address this problem we implemented an algorithm to compute the best relative position of each stack and compensate the tilting around x- and y-axes, and developed a plug-in module for the industry-standard platform for three-dimensional image manipulation called FIJI/ImageJ. Our technique involved the computation of local features called SIFT (scale invariant feature transform) to achieve a robust registration of big image stacks. The SIFT technique, introduced by D. Lowe in 1999 is a computer vision algorithm detecting and describing local feature vectors in images. The set of feature vectors of two similar images will also be similar, and matching those features is equivalent to an image comparison. The location of those similar features can be used as landmarks to compute a transformation model (translation and rotation) between the two images. The SIFT algorithm can be summarized in three steps; feature extraction when the locations of the feature vectors are extracted, feature matching when the comparable vectors between the two images are identified, and transformation model computation when the coordinates of the features of one image stack is aligned to those of the other stack.

The algorithm we developed based on this technique is a four-step procedure that can be iterated until satisfying results. First, the common part of the neighboring (front and back) stacks is extracted, then the rotation and tilt are fixed progressively around z-axis, x-axis and y-axis by

comparing cross-sections of similar positions within the overlap along the three cross-section planes.

The overlap extraction can easily be done under a simple assumption: the transformation, especially tilting induced by the image acquisition is small enough to keep a good similarity between image slices. Under this hypothesis, we developed two methods to determine the size of the overlap. In the first one, referred as “slice-by-slice”, the last slice of the front stack is then compared to all the sections of the back stack. The slice showing the strongest similarity (highest number of matching SIFT feature vectors) is selected as the boundary of the overlap. Within this common part, the cross-sections of the volume data at the same depth are compared and a first transformation model of rotation around the optical axis (z-axis) and translation along y-axis and z-axis is computed and applied to the back stack. Similarly, the cross-sections parallel to the (y, z) plan of the roughly registered back stack, are compared with the one of the front stack located at the same position. A new transformation model of rotation around x and translation along the other axes is computed and concatenated to the first one. Finally, the rotation around y and the remaining translation are identified by comparing the cross-sections parallel to (x, z). This way, the back stack is progressively matched to the front stack, and several iterations can improve the continuity of the final alignment.

However, because the limitation of imaging depth in confocal microscopy and the photobleaching that occur during image stack acquisition, the intensity and image quality of the corresponding optical sections in two overlapping stacks often appear somewhat different. Even though SIFT is in principle robust against inconsistent luminosity in the two images, in practice standardizing, even roughly, the brightness and contrast between the two stacks often gives better registration results. We therefore developed another software module that compensates brightness and contrast of serial section images within the stacks. Because the deeper slices usually appear darker than the upper ones it is often necessary to increase the intensity of the signal of each section of the image stack non-uniformly. For doing this we set two intensity correction values, one for the first slice and the other for the last, and the intermediate slices are

enhanced using interpolated parameters between those two values using one of the three transition curves, following a constant, linear or exponential law.

Precision of our SIFT-based image registration algorithm should be validated for finding the best parameters required for registration. However, because we can never know the precise amount of rotation in real samples, we have to make a mock pair of image stacks one of which is made from the same stack with the other but is rotated arbitrarily with known angles. Simple extraction and rotation of an image substack is not suitable for this purpose, because image clarity and noise level depending on the distance from the cover slip should also be simulated. To this purpose we created a simulator that generates artificial images that mimic laser scanning image stacks. It is known that confocal microscopes induce a noise in the data that follows a Gamma law of shape k and scale θ. We computed the empirical parameters along z-axis of the noise of our microscope by fitting a Gamma low to five real images, in the signal (fibers) and in the background, separately for the front and back stacks. A binary stack of tubular structures of neurites, generated by applying a threshold filter to a real image stack, was then cut into two overlapping substacks, and average values along z of those parameters were used as noise filter to reproduce realistic confocal three-dimensional images of fibers. The back stack was rotated and tilted at pre-defined angles before filtering. The resulting pair of image datasets were submitted to our registration algorithm and we found that the front and back substacks were correctly aligned after only two iterations of SIFT comparison.

Using this technique, we can now generate image stacks of the entire fly brain with very high optical resolution, which is suitable for analyzing fine and complex neural fiber branches such as those of the octopaminergic and dopaminergic neurons. We aimed at comparing the projections in the brains under different circumstances and performed two experiments. The first one, referred to as “age-dependency analysis” analyzes the morphological evolution of the octopaminergic and dopaminergic neurons over time by qualitatively and quantitatively comparing their arborization and connectivity patterns in the brains of young flies (5 day-old) and old flies (30 day-old). The second one, the “activity-dependency analysis”, examines the effect of

activity-dependent structural plasticity in the neural networks of monoamine cells. To this purpose we inactivate octopaminergic or dopaminergic neurons by cell-type specific expression of the inward-rectifier potassium ion channels called Kir2.1, which has the particularity to be opened at a resting membrane potential. This causes a massive flux of potassium through the membrane inducing its hyperpolarization. We have taken seven datasets of octopaminergic and dopaminergic neurons and their pre-synaptic sites of young and old flies as well as old files that are raised with and without cell-type specific neuron inactivation.

We could show differences between those neurons under various conditions. The qualitative analysis of the fiber aspect could not highlight clear differences for the age-dependency experiment (experiment 1) for both octopaminergic and dopaminergic neurons (5 days vs 30 days). Octopaminergic neurons seem to be less subject to the effect of time or inactivation than dopaminergic neurons which degenerate quickly after inactivation but also, at a slower pace, within time. Moreover, dopaminergic neurons are crucial for Drosophila melanogaster, who cannot survive more than a few days after inactivation. This suggests that the function of these neurons cannot be ensured by any other type of neurons. If no statistical differences were shown between the number of pre-synaptic sites of young and old sample (5 and 30 days), the inactivation of either neuron type have a big influence on the synapse number especially for older flies. Indeed, we could notice an average 20% decrease of octopaminergic sites compared to the control at 30 days (but no differences at 5 days). Dopaminergic pre-synaptic sites decrease is even more drastic and is visible immediately after birth. Similarly fibers appear highly degenerated in this phenotype whereas differences are not obvious for octopaminergic fibers. The behavior analysis supports those statements. 30 day-old octopaminergic deficient flies are showing abnormal behavior patterns such as no climbing, flying or jumping and shaking legs.

PART 2
INTRODUCTION

PART 2 INTRODUCTION

Comprehensive and systematic analysis of the connections between many brain regions and between numerous neurons within them, the so-called connectomics study, has become a key endeavor for understanding how complex neural network achieves sophisticated computational functions of the brain (Takemura et al. 2013, Shih et al. 2015). To this aim projection patterns of the neurons of each type and distribution of their synaptic sites should be revealed at great detail across the entire volume of the brain specimen.

1. BIOLOGICAL CONTEXT: STATE OF NEUROSCIENCES RESEARCH ADVANCES

The brain is the main organ of the nervous system in the huge majority of organisms. It has many functions including the reception, processing, and storage of information. That information is used in all cognitive action, consciously or not. The ultimate goal of neurosciences is a complete understanding of the biological mechanisms driving such behavior.

Since the philosophic revolution initiated by Platon (428 BC. – 348 BC.), who separated the soul in three parts and placed one of them, *psychikon*, in our brain, this one has been thought being the main seat of the soul as it is clearly involved in our consciousness. Hippocrates, often identified as the father of medicine, also developed and believed in the cerebrocentrism theory: the soul is located in the brain and, for all of these reasons, the brai investigation started relatively early in the History of medical sciences. Indeed, the Greek doctor Galien (129 – 216), was already performing brain dissections on animals. However, discovery stagnated until Renaissance after the Church lifted the ban on dissection. The philosophic and religious conceptualization of the brain progressively switched to an anatomical and physiological understanding.

As the main organ of our nervous system, the brain investigation remains, even nowadays a challenge for all neuroscientists. Various approaches exist for research concerning this organ, from the study of the brain as an object composed of interconnected cells (neuroanatomy) to its study as a complex abstract organ that can be affected by inner or outer factors (psychology). We will specially focus on the former; even if the limits between the different fields of neurosciences seem more and more blurry. Neuroanatomy appear at the beginning of the 18th century but is really on the rise at the middle of the 19th century, pulled by innovative techniques such as cells staining or advanced in histochemistry.

2. INTEREST OF DROSOPHILA MELANOGASTER MODEL

However, because the straightforward human body investigation is hampered by complex technical and ethical problems, scientists quickly opted for indirect research using animal models. Among them, Drosophila Melanogaster (fruit fly) has been one of the most popular to investigate a variety of fields from genomics to neurosciences for more than 100 years.

Initially, the fruit fly was chosen for maintenance and scientific practical reasons. Indeed, because of their inexpensive diet, a large number of fruit flies can be easily kept in the narrow space of the laboratory allowing large database of flies of various genotypes. Due to their short reproduction and life cycle, a big amount of data can be obtained in a short period which makes any experiment highly reproducible. Moreover, Drosophila melanogaster has only four large chromosomes where genes can be accurately mapped and can be easily manipulated including doing gene insertion. If humans have more genes than the fly, they both have about the same number of gene families and their sequences are often so well conserved that many human genes can be mapped to Drosophila melanogaster ones which make them particularly useful for the genetic research. For all those reasons, many tools have been developed to manipulate the fruit fly genome, offering opportunities to investigate other fields than genetics such as developments, morphogenesis or neurosciences leading to many discoveries, which, under certain conditions,

can be extrapolate to human research. Those tools include the insertion or deletion of genes or part of genes to drive or inactivate the expression of proteins in specific cells of the fruit fly.

3. DROSOPHILA MELANOGASTER

The brain of an adult fruit fly *Drosophila melanogaster* is a complicated network of about 100,000 neurons projecting in a 600-µm wide, 300-µm tall, and 160-µm thick volume. It cell bodies are mainly located at its surface (outer part) whereas the neurites innervate the inner part and form the synaptic neuropil. The central part of the brain, or cerebrum, is a subset of about 30,000 neurons symmetrically arborizing in each side of the midline. All neurons composing the network of the fruit fly central brain arise during neurogenesis by a multitude of asymmetric divisions of only a hundred of neural stem cells called neuroblasts. These neuroblasts divide asymmetrically to give birth to a family of clonally associated neurons. Progeny of some neuroblasts composes specific brain components such as the Antennal Lobe (AL) or the Mushroom Body (MB).

Most neuroblasts have two phases of proliferation. The first one occurs in the early to midembryonic stage and the second one in the early larval to early pupal stage. The former produces neurons of the primary (type I) lineage and the latter the secondary (type II) lineage. Even if most neuroblasts are type I, eight type-II cells were found. Their daughter cells are called the ganglion mother cells (GMCs) and each of them divides only once again to generate two neurons. In another hand, the type-II neuroblasts first give birth to intermediate neural progeny to generate a large number of various neurons whose arise after several divisions.

The set of clonally related neurons and their specific arborisations is called a clonal unit. A clonal unit can be seen as a building block to construct the neural network. In this study 96 clonal units were found. 94 of them were clearly identified as clonal units including 80 with a unique cluster of cell bodies of their neurons and 14 with multiple clusters located in different part of the fly brain, whereas 2 are still considered as potential clones. These clonal units contain multiple types of neurons that can produce various transmitters. In the fly brain, these clonal units are unique

in term of cell bodies location and projection pattern except for a few nearly identical clones. This variety depends on several factors such as the birth order of the neurons and the fate determination and may be correlated with the neuroblast identity determined by a unique combination of expressed genes during embryonic stage. This clonal unit organisation is believed to be conserved across the Insecta.

The mosaic analysis with a repressible cell marker (MARCM) technique developed by Lee and Luo in 1999 allows labeling the progeny of single neuroblasts and then highlighting the clonal unit organization visualization. A combination of cytoplasmic reporters such as DsRed or GFP can label the fiber but do not give any information about the direction of the propagation of the electric signal. An estimation of this information can be found by using synaptic vesicle-targeted fusion reporters (pre-synaptic marker).

A strong correlation between the functional architecture of the fly brain and the clones can be shown. The most obvious is probably the association between the sensory pathway and the clonal units such as the ones of the primary olfactory centers located in the AL and the MB or in higher olfactory pathways. However, clones do not arborize exclusively in the sensory or motor centers: 38 of them arborize in other neuropils. The clonal units can be characterized by several common features. First, the cell bodies of the neurons belonging to the same clonal unit form a packed cluster in the cell body rind (cortex) from which the neural fibers arise as a few tight bundles. Each bundle can project differently to innervate different neuropils. Thus, the innervation pattern can vary a lot in term of complexity but this complexity does not show any correlation with the number of neurons within the clonal unit which is rather varied. Some clones arborizes in several different neuropils whereas others are limited to one or a few neighboring neuropils. In another hand, some neuropils contain many different clonal units whereas others contain a few. Most of the clones are also connected with projection neurons.

The different parts of the brain can exchange information through many fiber bundles. These bundles are made by a tight association of a few clones or a unique clone suggesting a strong

correlation between the fiber bundles and the clonal units. This association can appear as soon as the neurons emerge from the cell body cluster or deeper in the neuropils. The polarity of the orientation of these neurons within these fiber bundles can be either the same or opposite even if the fibers projecting in the same direction are more common.

The diffuse neuropils are the regions other than the AL, the MB and the cortex (CX) and take their name due to the homogeneous appearance when they are study using classic labeling methods. Even if their functions and structures are not very known yet, the same clonal unit organization was found.

The entire set of neural projections within the brain is called projectome whereas the connectome refers to the map of connections positions between neurons. Neural subgroups (clonal units) show different projection patterns as well as the fine projection pattern of single neurons in each subgroup can also differ. It was found that several neuropils show lots of connections with their neighbors serving as hubs whereas others have much fewer connections. Moreover, a hub neuropil tends to be connected to the others by a large clonal variety of connections. We can feature three types of neuropil connections: the connections between two neuropils mediated by the projection neurons with symmetric distribution of the presynaptic sites, the ones with a presynaptic site only at one end and the ones mediated by local arborizations. The first ones can participate to directional or unidirectional communications whereas the second ones are important for the directed information flow. The third ones are involved in specific communications between communities.

Le location points of those neural communications, called synapses, are not homogeneous within the brain especially between specific types of neurons. A comprehensible map of the repartition of the synaptic sites appears then necessary to track the information exchange inside the brain. Such map is called connectome.

The fly brain shows a variety of neurons that can be categorized by type of neurotransmitters released in synapses. Among all those categories, we will focus on two specific neuron types: the octopaminergic and dopaminergic neurons and their connections (Fig. 2.1).

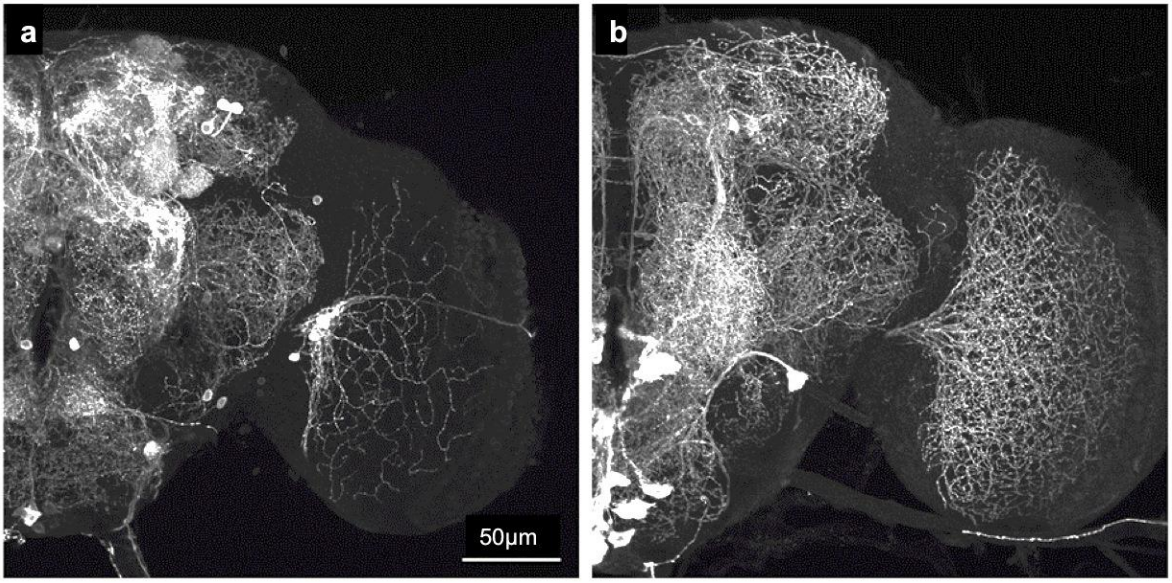

Figure 2.1. Spatial arborization of dopaminergic neurons (a) and octopaminergic neurons (b) of the adult Drosophila melanogaster brain. 3D reconstruction images of the entire stack after front and back substacks are registered and merged. 1600 x 1600 x 800 voxels, voxel resolution = 0.2 x 0.2 x 0.2 µm. Scale bar = 50 µm.

4. OCTOPAMINERGIC AND DOPAMINERGIC NEURONS

Octopamine, or β,4-dihydroxyphenethylamine (Fig. 2.2, left), is an endogenous trace amine exclusively found in invertebrate organisms. In insects, this molecule shows a wide range of functions. Indeed, it has been proven that octopamine act as a neurotransmitter, a neurohormone and a neuromodulater. Octopaminergic neurons present a very complex structure paired with a dense arborization spreading in the entire central nervous system. *Drosophila melanogaster* counts around 100 octopaminergic neurons and their organization is

well conserved among invertebrate organisms proving their importance. Indeed, those neurons are involved in high energy consuming behaviors such as jumping or flying.

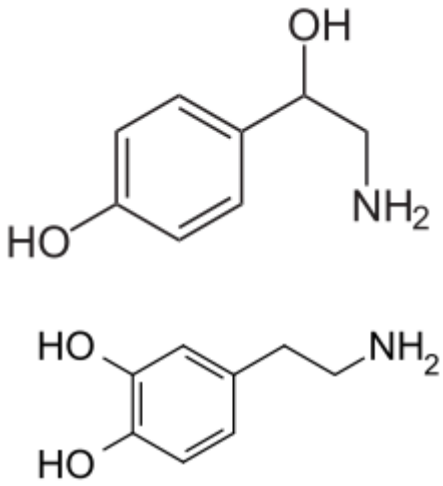

Figure 2.2. Representation of octopaminergic (top) and dopaminergic (bottom) molecules

4-(2-Aminoethyl)benzene-1,2-diol (Fig. 2.2, right), widely known as dopamine (DA), is a neurotransmitter and neurohormone found in many organisms (vertebrates and invertebrates). This molecule plays major roles in the human brain and body and dysfunctions of the dopamine system can lead to serious diseases such as Parkinson's disease or schizophrenia. In *Drosophila melanogaster*, similarly to octopamine, dopamine is involved in reward learning.

Octopaminergic and dopaminergic neurons appear to be determinant in the correct operating of the central nervous system and a precise and systematic analysis of their evolution and interaction is necessary. We investigate this problem through two distinct experiments referred as "age-dependency analysis" (also called experiment 1) and "activation-dependency analysis" (or experiment 2).

5. HOW TO VISUALIZE NEURONS?

Fluorescent microscopy is a powerful tool for visualizing and thus studying the projection patterns of neuronal fibers and synaptic connections sites of the octopaminergic and dopaminergic neurons. Neuronal structures such as axons and pre- and postsynaptic sites can be visualized using fluorophore-conjugated antibody labeling or targeted-expression of fluorescent proteins (Brand & Perrimon 1993). Upon excitation at particular wavelength of light,

fluorophores absorb specific wavelength of light and then emit light at slightly longer wavelengths in response. Using combinations of multiple excitation wavelength ranges and filters to restrict emission light, distribution of various neuronal objects can be recorded in the same specimen (Jefferis et al. 2012). Such proteins spread along cytoplasm to see the fibers and transported to the presynaptic sites to show the connectome. One can drive their expression using the Gal4-UAS system or the LexAop-LexA system.

a. The Gal4-UAS and LexA-LexAop System

The Gal4-UAS system is biochemical method used to analyze and control the expression and function of a gene. This technique was invented by Andrea Brand and Norbert Perrimon in 1993 and is now commonly used. The transcription of a gene is activated by proteins binding a short DNA sequence of the promoter region located in the upstream section of the gene called UAS (Upstream Activation Sequence). Those proteins named Gal4 are encoded by the gene GAL4 (Fig. 2.3.a). Similarly, a gene expression will be driven by LexAop in presence of LexA (Fig. 2.3.b).

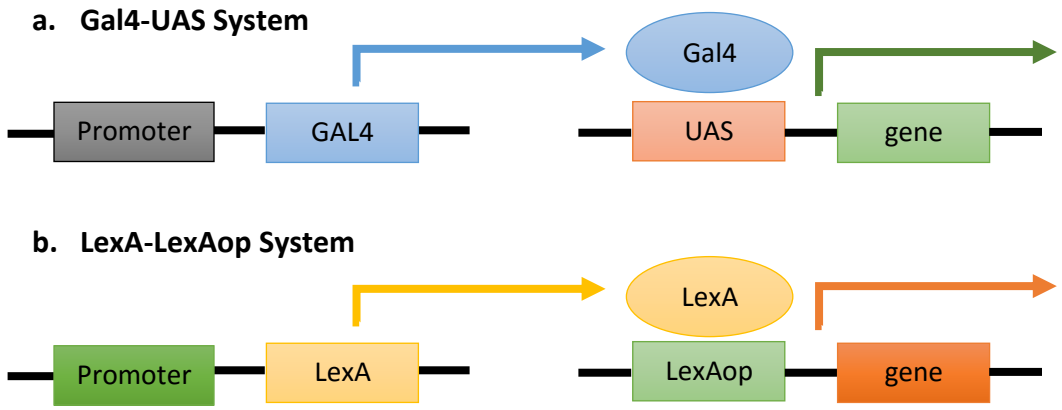

Figure 2.3. Comparison of the Gal4-UAS System (a) with the LexA-LexAop system (b) used to drive the expression of genes within specific types of cells

Using this system, it is possible to visualize neurons if the gene expressed is the one of a fluorescent protein. This way, DsRed, a red fluorescent protein gene, can be placed under the control of UAS. If Gal4

binds UAS, DsRed will be expressed and the neuron will be dyed in red. Similarly, if GFP is inserted after LexAop, the neuron cytoplasm will appear green in presence of LexA.

However, this system is not specific. Indeed, all cells containing Gal4 or LexA will be labelled. To be sure that fluorescent proteins are expressed in a particular cells Gal4 and LexA are themselves placed under the control of the promoter of a molecule present only in the targeted type of cells. For example, if we want to express Gal4 only in dopaminergic neurons and LexA only in octopaminergic neurons, their genes must be inserted after the promoter of proteins found in those two types of neurons only. We chose to use the promoter of two proteins specific to the chemical pathway of dopamine and octopamine synthesis. Tdc2 (Tyrosine decarboxylase 2) is an enzyme which transforms L-Tyrosine into p-Tyramine, the precursor of octopamine, but do not participate dopaminergic synthesis. Conversely, TH forms L-Dopa from L-Tyrosine to synthetize dopamine but is not involved to octopamine pathway (Fig. 2.5). Because of their specificity, the promoter of Tdc2 and TH are good candidates to drive the expression of Gal4 and LexA and consequently DsRed and GFP in octopaminergic and dopaminergic neurons (Fig. 2.4).

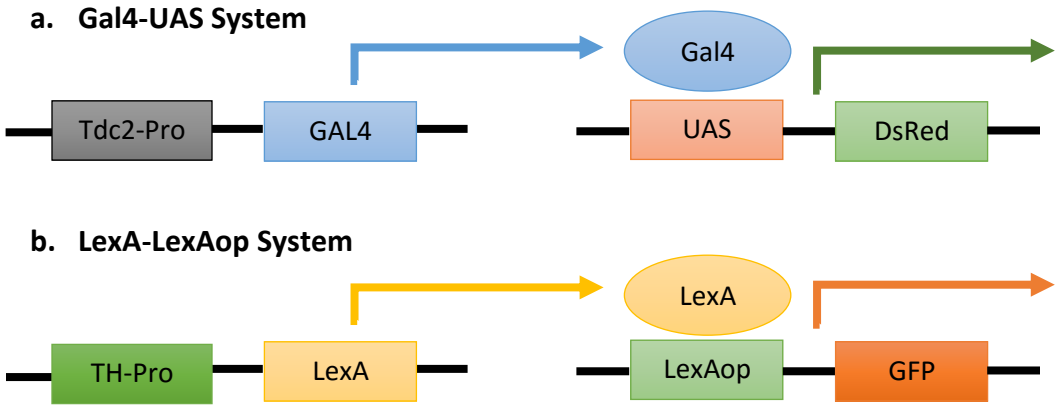

Figure 2.4. Gal4-UAS System (a) and LexA-LexAop system (b) for neuron vizualisation. Those systems respectively drive the expression of DsRed (red fluorescent protein) in octopaminergic neurons and GFP (green fluorescent protein) in dopaminergic neurons.

By associating Tdc2 with Gal4, both will be express at the same time in the cell. Because Tdc2 is an enzyme specific to the octopaminergic neurons, Gal4 will also be expressed only in octopaminergic neurons. In presence of Gal4, UAS activate the expression of genes under its

control: DsRed. In conclusion the octopaminergic neurons only will present the red fluorescent protein. Similarly, we combine TH and LexA so that when TH is expressed in dopaminergic neurons, LexA will be too, driving the transcription of genes under LexAop control, GFP, labelling the dopaminergic neurons in green.

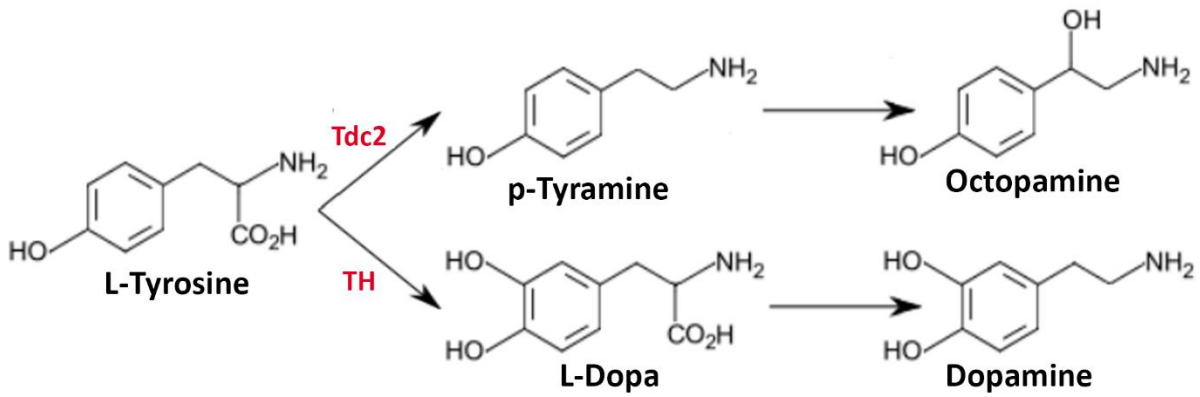

Figure 2.5. Synthesis pathway of octopamine and dopamine

b. CROSSINGS

Drosophilia melanogaster has four pair chromosomes: one pair of gonosome (X or Y) and and three pairs of autosomes (called second, third or fourth chromosomes). To visualize neurons of the *Drosophila* brain, the DNA of the fruit fly must carry genes driving the expression of fluorescent proteins whose emission wavelength can be detected by a fluorescent microscope.

Formally the names of genes (genotype) of Drosophila melanogaster are written for the four chromosomes separated with a semi-comma, ";":

gene1;gene2;gene3;gene4

with gene1 on chromosome 1, gene2 in chromosome 2, gene 3 in chromosome 3 and gene 4 in chromosome 4.

Because the fourth chromosome is really short and does not contain many genes, it will be omitted in this study.

We saw in the previous paragraph that, to be able to visualize neurons, they must be labelled by fluorescent proteins such as DsRed and GAL4 driven by the Gal4-UAS and LexA-LexAop system. Besides the gene encoding for the fluorescent proteins, the fly must also carry the ones necessary at those systems. This is achieved by crossing different lines carrying one or several of those genes.

In order to make sure that all required genes are present at the same time, they will be associated with balancers and other dominant genes modifying the phenotype of the insect such as eye color, wing shape… By screening those features among the flies, one can guess their genotype.

As an illustration of this procedure, let's detail it for one of the experiments (Annexes, Table 2.1). In this experiment we want to specifically visualize octopaminergic and dopaminergic neurons and their pre-synaptic sites to study their projection pattern as well as their interaction over time (so called experiment 1 or age-dependency analysis). The dopaminergic neurons will be specifically labelled in green using the GFP fluorescent protein and the octopaminergic neuron in red by DsRed. We set DsRed under the control of UAS and GFP under the control of LexAop, as described in the previous paragraph.

In order to achieve such labelling, the fruit fly must carry all of the necessary genes (UAS, GAL4…). To this purpose, we cross one male and one female of two *Drosophila* lines of known genotypes (Table 2.1.a&b) which carry the required genes. Because the high number of possible crossing combinations, to make sure that the fly does not miss any of them without sequencing the genome for each sample they will also be associated with markers and balancers. Because those genes affect the fly phenotype, their genotype can be guessed via its phenotype observation. For example, TM3 Ser, gene responsible of curled wings, in the third chromosome is 'paired' with TH-

LexA for the female flies. The descendant of those females will then receive either TH-LexA or TM3 Ser. If they carry TH-LexA their wings will be straight whereas they will be curled if they don't. Straight wing flies must then be selected among the progeny because they carry TH-LexA.

The Table 2.1.a and b show the genotype of the male and female flies for each chromosome and the different combinations of genes of their gametes. All the possible eggs of the crossing as well as the resulting phenotypes are investigated in Table 2.1.c. In conclusion, after crossing only the female flies with red eyes, straight and merged wings, long bristles and a standard body size will be selected for the dissection and staining.

c. CONFOCAL MICROSCOPY AND ITS LIMITATIONS

To obtain three-dimensional information about the distribution of fluorescent signals, a stack of serial section images is required. Using confocal or two-photon laser scanning microscopy, such serial section images can be obtained without actually slicing the samples. The specimen is illuminated point-by-point within its volume using a laser beam, and for each illumination position (each voxel) the emitted fluorescence signal is recorded by a photo detector. In case of confocal microscopy, a pinhole in front of the detector cuts off out-of-focus light, and in case of two-photon microscopy only a very small region at the focal point is illuminated with high-enough density of photons to enable two-photon excitation of fluorophores. Both methods enable acquisition of optical sections that can be much thinner than 1 µm.

Although laser scanning microscopy is a powerful tool for obtaining thin optical sections (Davidovitz et al. 1969, Fritzky et al. 2013), the possible depth of imaging is limited by three factors. First, the depth for which images can be recorded is limited by the working distance of the microscope objective. Second, the amount of light that reaches photo detectors is reduced by the attenuation of both excitation laser beam and the light emitted from the fluorescence-labeled objects in thick samples because the sample tissue that is optically not completely translucent (Ito et al, 2003). We can then observe a diminution of signal intensity and signal-to-

noise ratio. Finally, even when it is still within the working distance of the lens, the image quality tend to degrade in deeper regions and objects appear blurry with a low contrast. Although new techniques such as CLARITY and Scale (Chung et al., 2013, Hama et al., 2011) can increase transparency of samples, light rays are deflected and scattered when they pass through the tissue, because they are not optically uniform. In conclusion we can notice a considerable loss in quality when the focal plane becomes as deep as 100 µm from the sample surface (Graf et al. 2010), even with high numerical aperture and long working distance (more than 200 µm) objectives (Fig. 2.6).

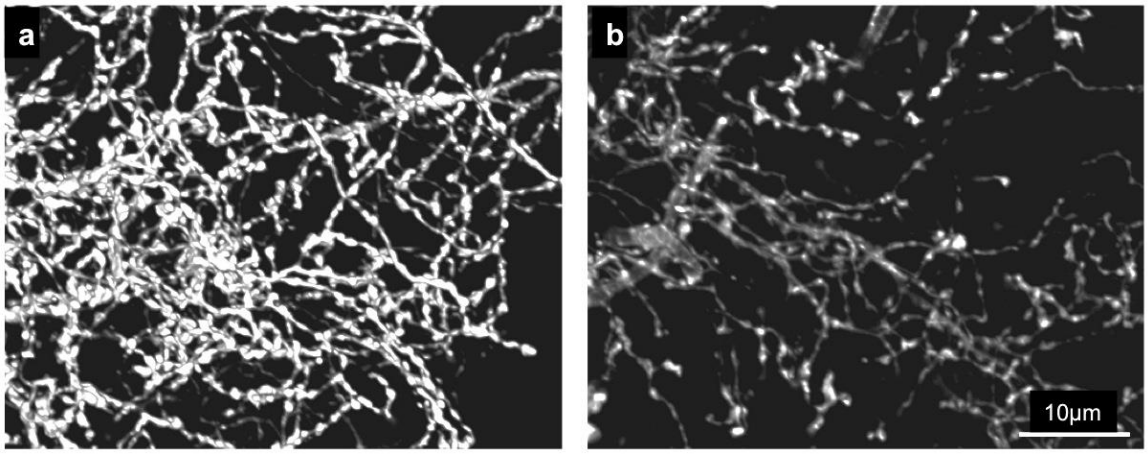

Figure 2.6. Difference in image quality along z-axis for the labelled fibers located in the area close to the sample surface (a: depth 30µm to 40µm) and further step in the specimen (b: 80µm to 90µm). 3D reconstruction of the respective subvolume. Scale bar = 10µm.

Two workaround techniques have been employed to overcome this problem. For the specimen that is thinner than about 300 µm along the optical axis (z-axis), it is possible to record the image from both sides of the sample that is embedded between thin cover slips (Ito et al. 2003). The first image substack covering the frontal half of the sample is taken from one side of the cover slip. The sample is then flipped, and the second substack is recorded from the other side. For the specimen that is even thicker, a sample can be embedded in a soft medium, and using vibratome, the surface of the sample block is physically scraped off at the thickness of about 100 µm after

taking image stacks of this region. By repeating this procedure, called two-photon tomography, in principle any thick specimen can be imaged (Ragan et al. 2012, Zheng et al. 2013).

In both approaches, image substacks should be acquired in an overlapping manner so that images of the corresponding optical sections of the sample should appear in the neighboring substacks. Using these overlapping sections as a guide, neighboring substacks can be concatenated, or stitched. However, such concatenation is not straightforward, because small rotation and translation can occur when the sample is flipped or when the block surface is cut off. Rotation can occur not only around the z-axis of the specimen but also around x- and y-axes (tilting). Moreover, because of the photobleaching that occur during image stack acquisition and different thicknesses from the sample surface, the intensity and image quality of the corresponding optical sections in two overlapping stacks often appear different.

This is why registration step is crucial for properly stitching substacks. Each neuronal fiber from neighboring stacks must appear perfectly connected to each other after stitching. A discontinuity in the final image stack would strongly affect further analysis such as neuron tracing (Cardona et al. 2013, Meijering 2010). Various attempts to create a fast and accurate registration algorithm have already been proposed and implemented on several platforms. Although these techniques can register translational shifts between the substacks and rotation around z-axis, none of them compensate for the tilting around x- and y-axes. Many techniques also become sluggish when stitching very large substacks. To address these problems, we developed a novel approach called 2D-SIFT-in-3D-Space Volume Stitching to register and stitch three-dimensional (3D) volume data using scale invariant feature transform (SIFT), which achieves robust registration of big image stacks that can mutually be tilted by at least as large as 20°. In addition, we developed a simulator that generates artificial laser scanning image stacks to validate the quality of registration quantitatively to find the best parameters required for registration, and a software module that compensates brightness and contrasts of serial section images within the stacks to achieve even and more precise stitching.

PART 3
MATERIALS AND METHODS

PART 3 MATERIALS AND METHODS

Our model system, the brain of the adult fruit fly Drosophila melanogaster, contains about 100,000 neurons in the volume that is approximately 600-µm wide, 300-µm tall, and 160-µm thick. The fly brain has been an intense focus for brain-wide analysis of neural networks and their functions (Ito et al. 2014, Shih et al. 2015, Takemura et al. 2013). A wide variety of neuron types can be visualized using cell-specific expression driver strains (Brand & Perrimon 1993). Among them the dopaminergic and octopaminergic neurons, which are known to be involved in diverse brain functions, form dense arborizations extensively in almost all the brain regions (Busch et al. 2009, White et al. 2010). Projection patterns of neuronal fibers and distribution of synaptic connection sites can be visualized by expressed proteins that are spread along cytoplasm and those that are transported to presynaptic sites, such as red fluorescent protein DsRed and hemaglutinin (HA) fused with synaptic vesicle-bound protein synaptotagmin (syt; syt::HA), respectively. Because those neurons feature complex arborizations that are much denser and finer than most other neurons (Fig. 2.1), high-resolution microscopy images are required. To this aim, images of the fluorescent antibody-labeled samples were recorded at an image resolution of 0.2 x 0.2 x 0.2 µm each, in total 1600 x 1600 pixels and approximately 800 serial sections.

1. FLY STRAIN AND CROSSINGS

a. Flies

Fruit fly Drosophila melanogaster stocks were raised on standard fly food medium at 25°C on a 12/12 light/dark cycle. The Gal4-UAS system was used to express reporter proteins that visualize the cytoplasm and presynaptic sites of specific subsets of neurons. The yeast-derived GAL4 gene encodes a transcription activator protein Gal4, which binds to the Upstream Activation Sequence (UAS) to activate transcription of the downstream gene. In this study we used TH-GAL4 and Tdc2-

GAL4 to drive expression in dopaminergic and octopaminergic neurons, and used UAS-DsRed and UAS-Syt::HA to express cytoplasmic and synaptic-vesicle targeted reporter proteins.

The combination used for the experiments are summarized below.

b. Experiment 1 (AGE-DEPENDANCY ANALYSIS)

Two genetic combination were used: in the first one (genotype 1), octopaminergic neurons were labelled in red with the fluorescent protein DsRed, their pre-synaptic sites in blue, and the dopaminergic neurons in green by GFP using the GAL4-UAS and LexA-LexAop systems. The second genotype is the opposite combination: DsRed labels dopaminergic neurons whereas GFP targets octopaminergic neurons. The dopaminergic pre-synaptic sites remain in blue (Fig. 3.1&2). The lines and crossings necessary to get those genotypes are summarized below:

Genotype 1:

♂ ♂ yw UAS-Syt ::HA UAS-DsRed; +/+; LexAop-rCD2::GFP/TM6 Sb Tb

x

♀ ♀ w; Tdc2-GAL4/CyO; TH-LexA/TM3 Ser

→ ♀ ♀ yw UAS-Syt ::HA UAS-DsRed/w; Tdc2-GAL4/+; TH-LexA/ LexAop-rCD2::GFP

Genotype 2:

♂ ♂ yw UAS-Syt ::HA UAS-DsRed; +/+; LexAop-rCD2::GFP/TM6 Sb Tb

x

♀ ♀ w; Sp/CyO; TH-GAL4 Tdc2-LexA/TM3 Ser

→ ♀ ♀ yw UAS-Syt ::HA UAS-DsRed/w; +/CyO or Sp; TH-GAL4 Tdc2-LexA/LexAop-rCD2::GFP

For the purpose of an accurate statistical analysis, seven three dimensional images of each genotypes were taken at 5 and 30 days (28 images in total), using the two step procedure described later and registered using our developed Fiji plugin.

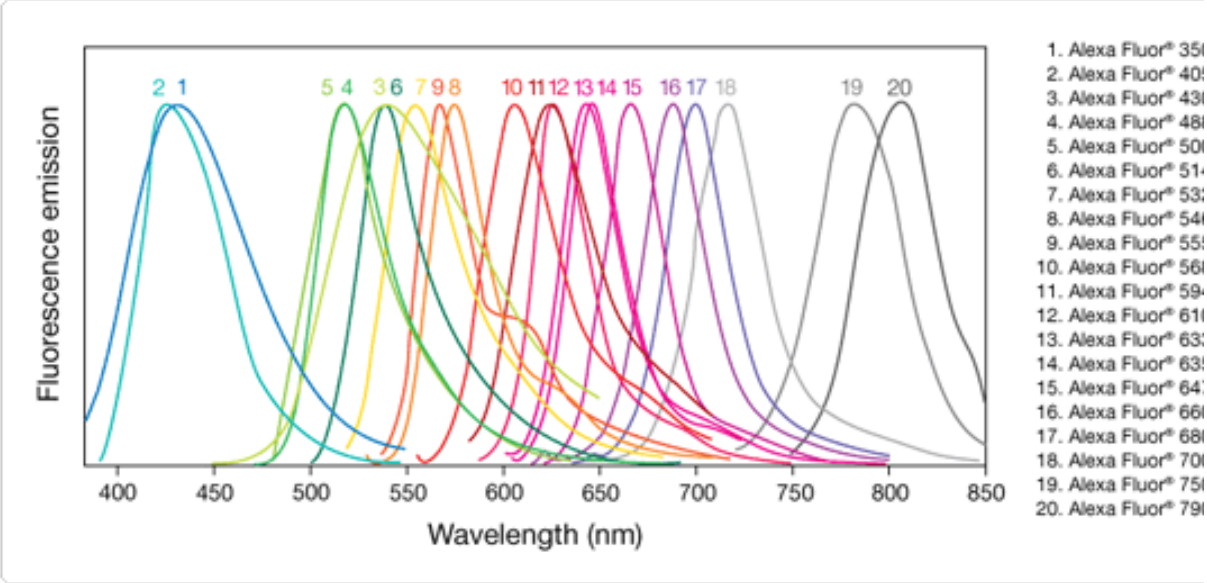

Figure 3.1. Emission spectra for Alexa Fluor® dyes.

Alexa Fluor® dye	Absorption max. (nm)	Emission max (nm)	Emission color*	Extinction coefficient**
Alexa Fluor® 350	346	442	Blue	19,000
Alexa Fluor® 405	401	421	Blue	34,000
Alexa Fluor® 430	433	541	Green/Yellow	16,000
Alexa Fluor® 488	496	519	Green	71,000
Alexa Fluor® 532	532	553	Yellow	81,000
Alexa Fluor® 546	556	573	Orange	104,000
Alexa Fluor® 555	555	565	Orange	150,000
Alexa Fluor® 568	578	603	Orange/Red	91,000
Alexa Fluor® 594	590	617	Red	73,000
Alexa Fluor® 610	612	628	Red	138,000
Alexa Fluor® 633	632	647	Far Red	239,000
Alexa Fluor® 635	633	647	Far Red	140,000
Alexa Fluor® 647	650	665	Near-IR***	239,000
Alexa Fluor® 660	663	690	Near-IR***	132,000
Alexa Fluor® 680	679	702	Near-IR***	184,000
Alexa Fluor® 700	702	723	Near-IR***	192,000
Alexa Fluor® 750	749	775	Near-IR***	240,000
Alexa Fluor® 790	784	814	Near-IR***	270,000

***** Typical emission color seen through the eyepiece of a conventional fluorescence microscope with appropriate filters.
****** Extinction coefficient at lmax in cm-1M-1.
******* Human vision is insensitive to light beyond ~650 nm; it is not possible to view near-IR fluorescent dyes.

Table 3.1. Properties of Alexa Fluor® Dyes

c. EXPERIMENT 2 (ACTIVITY-DEPENDENCY ANALYSIS)

Kir2.1 is an inward-rectifier potassium ion channels, presents in Drosophila melanogaster as well as in humans. By appropriate crossing, we placed the gene of this protein under the control of GAL4-UAS. The expression of GAL4 is itself under the supervision of GAL80[ts]. This protein, found in the yeast, is temperature sensitive due to a mutation and was cloned and introduce in Drosophila. In presence of GAL80[ts] and at a reasonable temperature (20°C), GAL4 is inhibited (Fig. 3.2.a). However, after heat shock (30°C), GAL80[ts] is inactivated and stops affecting GAL4 driving the expression of Kir2.1 leading to an over-expression of potassium channels (Fig. 3.2.b).

Kir2.1, which has the particularity to be opened at a resting membrane potential, will therefore allow a massive flux of potassium through the membrane inducing its hyperpolarization, and thus preventing neuron excitability by lowing the resting membrane potential below the threshold necessary to initiate action potentials (James & al., 2009). The affected neurons lose their firing ability.

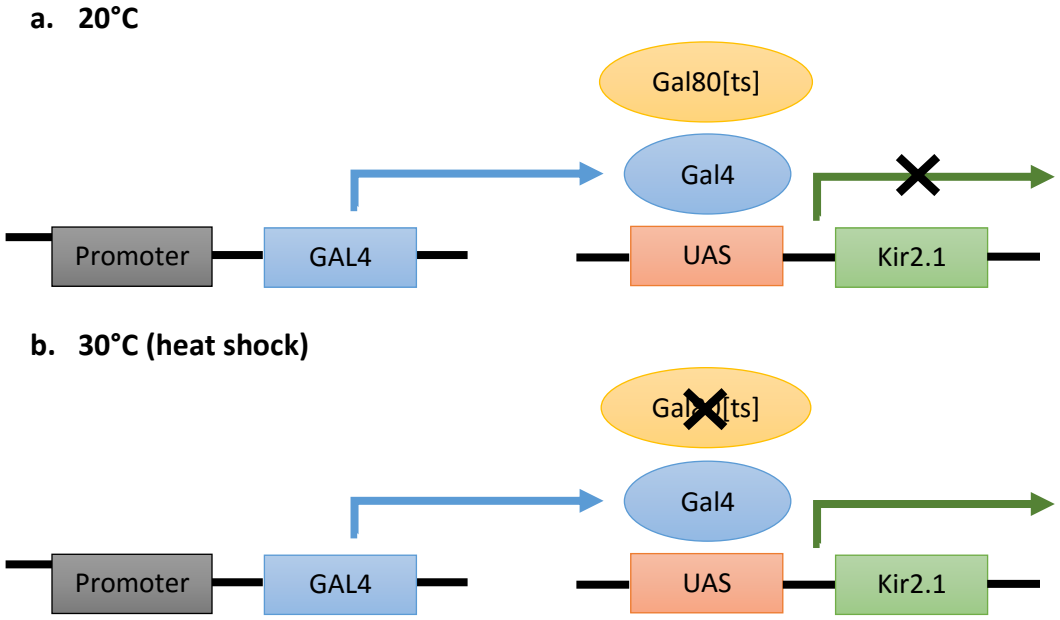

Figure 3.2. Gal4-UAS system for experiment 2

Brains, in which the neurons are inactivated are compared with a control (wild type). Four genotypes carrying a different combination of genes are then necessary: genotype 1.1 highlight inactivated dopaminergic neurons and their pre-synaptic site whereas as genotype 1.2, the control has functional octopaminergic neurons. Similarly dopaminergic neurons are inactivated genotype 2.1 but work for genotype 2.2.

Genotype 1.1:

♂ ♂ yw UAS-Syt ::HA ; UAS-Kir2.1/CyO ; tub-GAL80[s]/TM6 SB

x

♀ ♀ w; Tds2-GAL4/SM1; UAS-mCD8::GFP/TM3 Ser

→ ♀ ♀ yw UAS-Syt ::HA/w; Tdc2-GAL4/ UAS-Kir2.1; tub-GAL80[s]/ UAS-mCD8::GFP

Genotype 1.2:

♂ ♂ yw UAS-Syt ::HA ; Sp/CyO ; +/+

x

♀ ♀ w; Tdc2-GAL4/SM1; UAS-mCD8::GFP/TM3 Ser

→ ♀ ♀ yw UAS-Syt ::HA/w; Tdc2-GAL4/Sp; UAS-mCD8::GFP/+

For both the control and the inactivated neurons sample, pictures were taken at 5 days and 30 days after birth.

Genotype 2.1:

♂ ♂ yw UAS-Syt ::HA ; UAS-Kir2.1/CyO ; tub-GAL80[s]/TM6 SB

x

♀ ♀ w; UAS-mCD8::GFP/CyO; TH-GAL4/TM6B Sb Ser

→ ♀ ♀ yw UAS-Syt ::HA/w; UAS-mCD8::GFP/UAS-Kir2.1; tub-GAL80[s]/TH-GAL4

Genotype 2.2:

♂ ♂ yw UAS-Syt ::HA ; Sp/CyO ; +/+

x

♀ ♀ w; UAS-mCD8::GFP/CyO; TH-GAL4/TM6B Sb Ser

→ ♀ ♀ yw UAS-Syt ::HA/w; UAS-mCD8::GFP/Sp; TH-GAL4/+

For this genotype, we took pictures right after birth (0 days) and at 5 days. This change in the experimental protocol is due to the low surviving rate of the flies missing dopaminergic neurons. The nc82 labelling shows a normal brain perfectly similar to the control at the first glance: average size, no atrophy… However, whereas we could clearly see the octopaminergic neurons even after they have been switched off, dopaminergic neurons degenerate extremely rapidly. Indeed, in Kir2.1 neurons, only a few of them are visible despite a higher laser power used to detect week signal.

d. GENETIC COMBINATION SUMMARY

The following table, summarize the gene combination for experiment 1 and 2:

	EXPERIMENT 1		EXPERIMENT 2			
	GENOTYPE 1	**GENOTYPE 2**	**GENOTYPE 1.1**	**GENOTYPE 1.2**	**GENOTYPE 2.1**	**GENOTYPE 2.2**
GREEN	DP	OP	NC82	NC82	NC82	NC82
RED	OP	DP	OP	OP	DP	DP
BLUE	OP PRE-SYN	DP PRE-SYN	OP PRE-SYN	OP PRE-SYN	DP PRE-SYN	DP PRE-SYN

Table 3.2. Summary of genotypes for experiment 1 and 2. DP = dopaminergic neurons, OP = octopaminergic neurons, pre-syn = pre-synaptic sites.

Nc82 labelling is a 'background labelling'. Using this technique, all the synaptic sites of the brain are labelled with fluorescent labelling. Because those connexion sites are present everywhere, the whole brain appears to emit fluorescence.

2. DISSECTION AND IMMUNOHISTOCHEMISTRY

Adult female flies 5-10 days after hatching were dissected in cold PBS buffer and fixed in a solution of 10% formaldehyde in PEM buffer and kept on ice for 20 minutes. The fixative solution is refreshed and the samples were further incubated at 4°C for two hours. The sample were then rinsed twice with PBS and three times with PBT (PBS with 0.1% Triton-X) for 15 minutes each, and incubated with a solution of 10% normal goat serum (NGS) in PBT for one hour at 4°C to block nonspecific binding of antibodies. The samples were then incubated for two days at 4°C with the primary antibodies in a 10%-NGS in PBT solution, rinsed six times in PBT and blocked again for 1 hour at 4°C in a 10%-NGS in PBT. After an overnight incubation with the secondary antibodies at 4°C, the samples were rinsed again six times in PBT and twice in PBS. They are then incubated for 2 hours at 4°C in a 50% glycerol-PBS solution and overnight in an 80% glycerol-H2O solution.

However, even if GFP and DsRed show a natural fluorescence, it decreases quickly after the animal death due to protein degeneration. In order to overcome this problem, we use antibody labelling techniques to reveal the neurons by binding DsRed, GFP and HA with artificial fluorescent dyes, much more stable. Such labelling is a two-step procedure in which the sample is successively incubated with primary and secondary antibodies.

Primary antibodies do not show fluorescent properties, they respectively come from the rabbit, the mouse and the rat, and are used as anchors for the fluorescent dye conjugated antibodies. Anti-GFP (mouse, Roche #118114460001, diluted at 1:250), anti-DsRed (rabbit, Clontech #632392, diluted at 1:1000) and anti-HA (rat, Roche clone3F10#11867423001, diluted at 1:1000) are the primary antibodies used to bind reporter molecules.

To detect primary antibodies, Alexa 488-conjugated anti-rat IgG, Alexa 568-conjugated anti-rabbit IgG and Alexa 647-conjugated anti-mouse IgG in a 10%-NGS in PBT solution were used at dilution of 1:250. Those molecules, called secondary antibodies, detect primary antibodies and fixed them. Alexa Fluor® 488, Alexa Fluor® 568 and Alexa Fluor® 647 are artificial molecules able to emit fluorescence wave upon excitation of a determined wavelength (see tab.[Alexa]).

3. MOUNTING AND CONFOCAL MICROSCOPY

As discussed earlier, image quality degrades as the plane of the scanning optical section goes deeper into the specimen. Even with high-resolution objective lenses that are designed to match the refraction index of the mounting medium (e.g., oil-, silicon-, glycerol- or water-immersion objectives), image quality of the optical sections that are deeper than several tens of micrometers are not as good as those near the sample surface. Thus, even though the total thickness of the samples used here (~160 µm) is well within the working distance of the objective lens used (~280 µm), deeper half of the samples cannot be recorded with optimum resolution if they are imaged only from one side. To address this issue, we mounted the specimen between thin cover slips on both sides with a space of 200-µm thickness, and the deeper half of the sample is recorded from the other side by flipping the preparation. The two substacks, taken from the anterior and posterior sides of the brain, were then merged after flipping the volume data of the back substack.

The brain samples were mounted between long and short cover slips to make it possible to take pictures from both sides (Fig. 3.3). Polyvinyl Chloride (PVC) tape with the thickness of 0.2 mm was used as a spacer between the two cover slips to keep the space for holding the brain samples (thickness ca. 0.16 mm).

a. One-pass imaging mounting

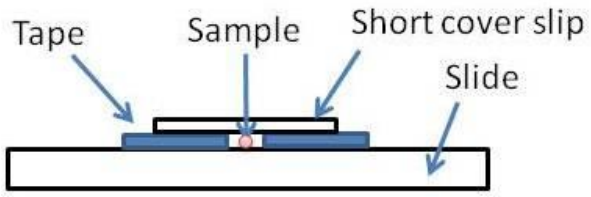

b. Two-pass imaging mounting

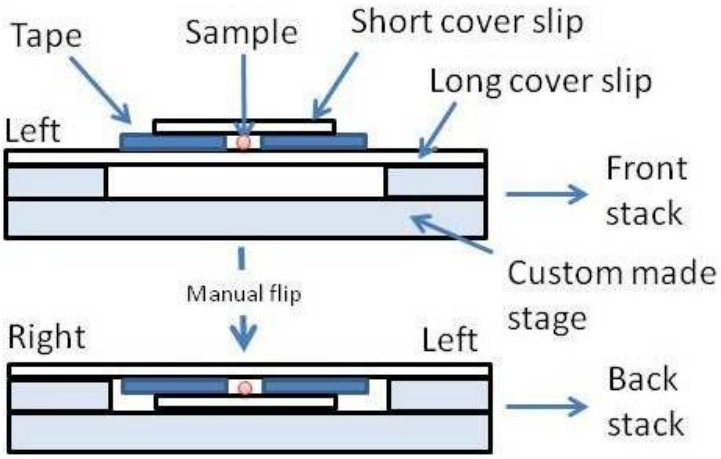

Figure 3.3. Monting differences according to the acquisition method, (a) classical one-pass imaging, (b) new two-pass imaging

This approach works well if the samples are mounted in rigid medium and if the sample after flipping can be placed exactly at 180° from the original direction. However, fluorescent samples are often mounted in a fluid substrate such as 80% glycerol, in which the specimen is not completely fixed but stay afloat. Slight rotation may therefore occur when the samples are flipped (Fig. 3.4). In addition, because of the instrumental error, the two cover slips may not completely be in parallel, causing the flip that is not exactly at 180°. Such error would not cause severe problems if the images were taken at relatively low resolution. However, to reconstruct fine neuronal fibers that are often thinner than 0.5 µm, even subtle misalignment results in discontinuity such as gaps or seams, if the substacks are concatenated without fine three-dimensional rotation.

a. **First imaging pass**

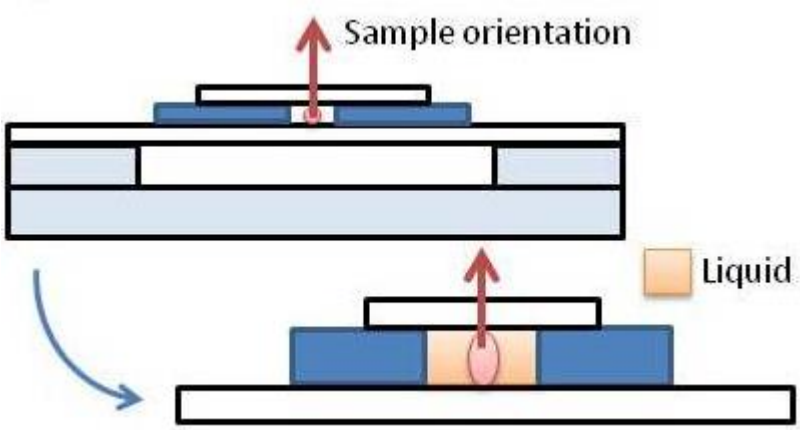

b. **Second imaging pass**

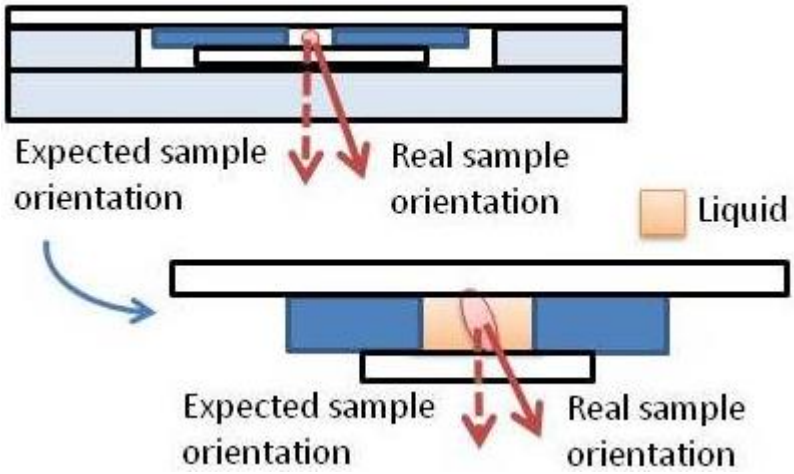

Figure 3.4. Sample rotation between the two acquisition passes. The sample is mounted between two thin cover slips, floating in a solution. After the first imaging pass (a), the sample is flipped (b). Because the sample is not fixed between the cover slips, slight rotations can occur.

3D image stacks were obtained using a confocal laser scanning microscope (Olympus FV1000 and FV1200) with a 40x silicon immersion objective (NA=1.25) at the resolution of 0.2 x0.2 µm pixels on x-y plane and 0.2 um of z focus step. The first 3D image substack was obtained by taking serial section images from the anterior (front) surface of the brain toward its mid-level. The sample was then flipped and a new substack of pictures was obtained from the posterior (back) surface toward the mid-level of the brain.

Both substacks must be slightly longer than the half-depth of the brain sample so that they should overlap at the mid-level. The back substack was flipped back using image manipulation software

to be in the same orientation as the front substack, and the two substacks were stitched so that signals in the overlapping volume should match exactly as explained in the Result section.

Part 4
Results

Part 4 Results

Connectomics study is the comprehensive and systematic analysis of the connections between the different brain regions and between numerous neurons within them. Understanding how complex neural network achieves sophisticated computational functions of the brain (Takemura et al. 2013, Shih et al. 2015) is a key of modern neurosciences research. The projection patterns of the neurons of each type and distribution of their synaptic sites should then, be carefully analyzed across the entire volume of the brain. However, octopaminergic and dopaminergic neurons show a much complex structure than any other category of neurons. Indeed, those two types of monoamine neurons feature very complex structures with many thin branches that are densely spread in the whole 160µm-thick fly brain, multiplying the connections with other neurons. Due of this extreme complexity, three-dimensional images of very high resolution (0.2µm cubic voxels) are necessary to characterize their morphology.

Because of the imaging depth limitation of confocal microscopy, we decided, to keep a constant quality throughout the sample, to separate the acquisition in two steps: the imaging is done from the front toward the sample and from the back toward the front. The images are then fused in a large stack of very high resolution (0.2µmx0.2µmx0.2µm). However, this fusion is not straightforward because of the movement of the sample between the two cover slips when the sample is flipped. An accurate registration method must therefore be developed for a precise stitching of the two images.

Using this technique, we can image at high resolution neural fibers spreading in the whole brain such as octopaminergic and dopaminergic neurons. We aim to characterize the morphology of those monoamine neurons under various conditions. First, we want to track the evolution of their projection pattern with time by comparing young (5days) and old (30days) Drosophila melanogaster. We also want to determine the effect of aging on the communication of octopaminergic and dopaminergic neurons with their neighboring neurons through the analysis

of the repartition of their pre-synaptic sites. Besides, the aging effect, we also investigated the plasticity of the fruit fly brain by switching off those neurons separately and studying the consequences on the brain.

1. A STITCHING ALGORITHM

The first step to study very extensive fibers such as dopaminergic and dopaminergic neurons is the acquisition of very high resolution images of the entire 160µm-thick brain. However, confocal microscopy has an imaging limitation of approximatively 100µm. After this limit, fibers usually appear broken up, with a low intensity or fused with their neighbor. In order to overcome this problem, we saw in the introduction that several workaround techniques has already been proposed, recording the image from both sides for thin samples or progressively scrap off the specimen surface while recording for thicker ones.

a. THE SOLUTION

No matter the chosen approach, in both cases, the substacks must be overlapping so that images of the corresponding optical sections of the sample should appear in the neighboring substacks. The overlapping slices can be used to guide the concatenation or stitching. However, this stitching is not straightforward because small rotations (around the optical axis), translations and tilting (rotation around x and y-axes) can occur when the sample surface is cut off of flipped. Moreover, the sample is imaged twice within the overlap: because fluorophore are partially emitted during the first acquisition, the sample appears darker in the second image: this phenomenon is called photobleaching. In consequence the intensity and image quality of the corresponding optical sections in two overlapping stacks often appear different. For all these reasons, a direct concatenation of two substacks often leads to discontinuities in the data (Fig. 4.1). In order to preserve the continuity of neuronal fibers at the seam of two neighboring stacks, they must be

registered. Registration is a crucial step for a proper substacks stitching because a bad neuronal connectivity in the final image stack would strongly affect further analysis such as neuron tracing.

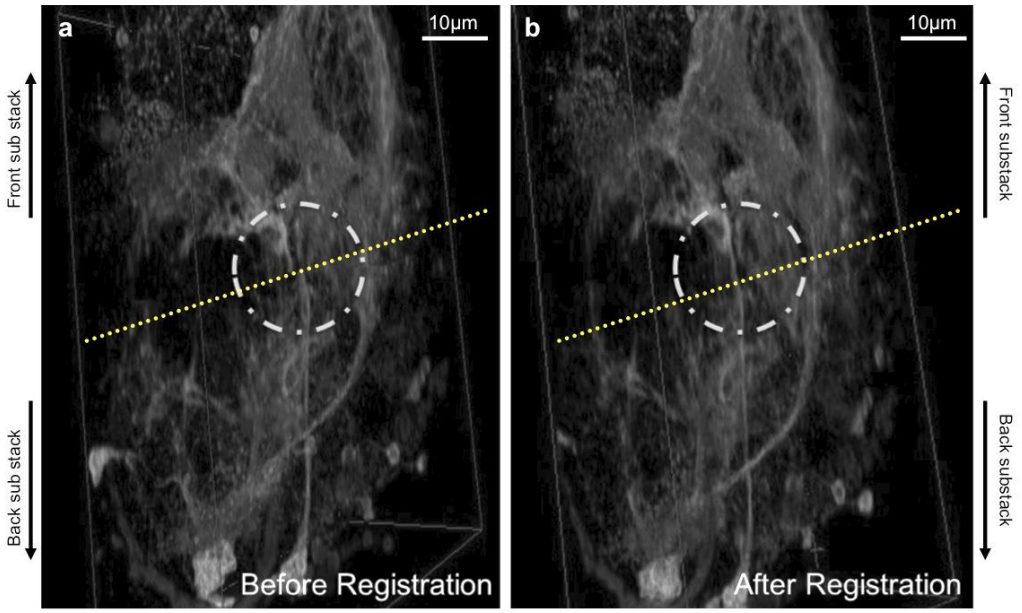

Figure 4.1. Importance of registration on 3D Stack of images to avoid discontinuity in the final 3D image stack, (a) Concatenation without fine registration. Gaps and seems are observed in the neural fibers that should be continuous at the boundary between the front and the back substacks (dotted circle), (b) Concatenation after registration. Fibers appear continuous.

b. MOUNTING

As discussed earlier, image quality degrades as the plane of the scanning optical section goes deeper into the specimen. Even with high-resolution objective lenses that are designed to match the refraction index of the mounting medium (e.g., oil-, silicon-, glycerol- or water-immersion objectives), image quality of the optical sections that are deeper than several tens of micrometers are not as good as those near the sample surface. Thus, even though the total thickness of the samples used here (~160 µm) is well within the working distance of the objective lens used (~280 µm), deeper half of the samples cannot be recorded with optimum resolution if they are imaged only from one side. To address this issue, we mounted the specimen between thin cover slips on

both sides with a space of 200-µm thickness, and the deeper half of the sample is recorded from the other side by flipping the preparation (Fig. 4.2). The two substacks, taken from the front and back sides of the brain, were then merged after flipping the volume data of the back substack.

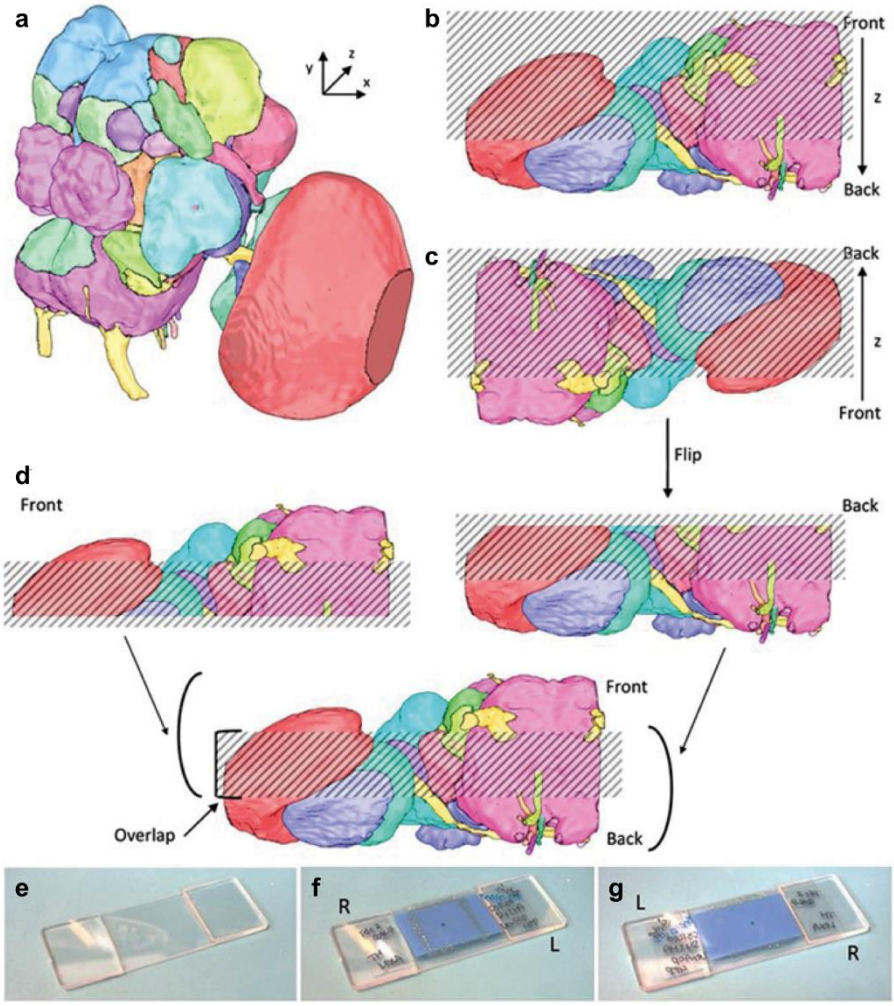

Figure 4.2. Substack acquisition, (a) A schematic view of the fly brain seen anterior-obliquely, (b) Optical sections of the front substack are acquired from the anterior end of the brain toward its mid-level, (c) After flipping the sample on the microscope stage, images of the back substack are acquired from the posterior end toward mid-level, (d) Image registration: the back substack is flipped and fused with the front one after fine tuning of relative position and angle; The sample is mounted between two thin cover slips, (e) support plate for image acquisition (f) front acquisition, (g) the sample is flipped for the back acquisition.

This approach works well if the samples are mounted in rigid medium and if the sample after flipping can be placed exactly at 180° from the original direction. However, fluorescent samples are often mounted in a fluid substrate such as 80% glycerol, in which the specimen is not completely fixed but stay afloat. Slight rotations may therefore occur when the samples are flipped. In addition, because of the instrumental error, the two cover slips may not completely be in parallel, causing the flip that is not exactly at 180°. Such error would not cause severe problems if the images were taken at relatively low resolution. However, to reconstruct fine neuronal fibers which are often thinner than 0.5 µm, even subtle misalignment results in discontinuity such as gaps or seams, if the substacks are concatenated without fine three-dimensional rotation (Fig. 4.1, left).

Many attempts of fast and accurate registration algorithms have already been made and implemented for various platforms. Most of them focus on two dimensional registration with a correction of the rotation around the optical axis and the translation along the other axes but do not propose any solution for the tilting around x- and y-axes. Those algorithms will be described later in this document.

c. IMAGE REGISTRATION WITH SIFT

A discontinuity resulting from an inaccurate stitching of the front and back stack is an issue for further processing and analyses such as neuron tracing (or segmentation). This technique identifies neurons by tracking their signal within a three-dimensional stack of images to create a reconstruction as series of interconnected lines. This reconstruction, also called trace represents the neuronal fibers as skeleton lines or cylinders, cones or spheres that include information about fiber diameter. Many algorithms has been proposed in the past years, supported by project like the DIADEM challenge (Brown et al. 2011) awarding the best tracking algorithm for a set of various data (single neurons, small networks…). However, neuron tracing remains challenging especially on network such as octopaminergic or dopaminergic neuron networks which present

a dense arborization of thin branches spreading in the whole brain, or if data has gaps or seams. A careful registration is therefore necessary to avoid such problems.

This stitching issue is not new because many samples are too thick for single acquisition and several algorithms have been developed and are available on various platforms such as the one by Preibisch et al. (2009) for the image analysis software Fiji and ImageJ. It minimizes the global pairwise registration error to compute the best registration based on phase correlation to find the translation between all image pairs. To correct the brightness differences between the two stacks due to photobleaching during acquisition, they are fused by non-linear blending. This plugin does not however fix the tilting around x and y but matches the substacks only by translation along x, y, and z axes and rotation around z-axis.

Another approach is used by Rameshy et al. (2013) for their algorithm that estimates the overlap and computes the rotation and translation around each axis between two complementary stacks using the Fourier Shift property in 2D on variable depth image intensity projections. The coefficient of correlation between the maximum intensity projections (MIPs) of each stack is computed for all possible transformation and various MIP sizes for each channel. A linear blending is then used to fuse the data and maximize the information from both stacks. This brute force approach requires computation of the cross-correlation of images according to many parameters: channels, MIP size, rotation and translation values, which is very fastidious and time consuming compared to the comparison and matching of a set of landmarks. Moreover, the algorithm is not yet implemented in full detail as a usable software tool.

To develop a more versatile tool that can register substacks along all the six degrees of freedom precisely and rapidly, we propose a new approach called 2D-SIFT-in-3D-Space, which is based on scale invariant feature transform (SIFT), and implemented it as a plugin module 2D-SIFT-in-3D-Space Volume Stitching for Fiji and ImageJ.

The SIFT technique, originally introduced by Lowe (1999, 2004), is a computer vision algorithm detecting and describing images by a set of local features characterized by their location, orientation and scale. The comparison of two set of vectors extracted from two different images is then equivalent to an image comparison and that is why this technique is often use for object recognition. In this work we propose a registration algorithm based on the extraction and matching of such features between two different images. The position in the image of similar structure can be used as landmark to compute a transformation model between the two images for an accurate registration. This type of approach is more suited when dealing with large datasets than intensity-based registration methods. Many other algorithms for local feature detection have been introduced in the literature (Lindeberg 1998, Mikolajczyk and Schmid 2005, Li and Allinson 2008), and in principle the whole pipeline presented in this work would a priori work for any local feature detection algorithms. The reasons for our choice of SIFT is not specifically linked with its scale invariance property since here the two considered images have the same pixel resolution, but because SIFT is robust in terms of rotation and intensity variations. This is specifically suited for our application since such distortions are likely to occur between the substacks to be registered due to movement of the specimen as well as photobleaching.

The SIFT algorithm is described in detail by Rey-Otero and Delbracio (2014) for a didactic description of this method, the interested reader may refers to their work whose some clues will be given below. The basic proceeding of our plugin to register two volume data substacks for 2D-SIFT-in-3D-Space can be summarized in three steps. First, the portions of the two substacks that contain overlapping image data are identified with repeated SIFT comparison between sections using the well-established, multithreaded fast 2D SIFT algorithm developed by Stephan Saalfeld (http://fiji.sc/Feature_Extraction; Fig. 4.3.b). And second, optimum degrees of translation and rotation of the substacks will be calculated (Fig. 4.3.d) for all the six degrees of freedom to achieve the best match within the overlapping volume by performing 2D SIFT comparison in the re-sliced images in three orthogonal planes (x-y, y-z, and x-z; Fig. 4.5). These two steps can be iterated to improve matching precision. Finally, using the obtained parameters, the entire substack is transformed from the original data and merged with its partner.

To achieve the goal described above, we employed a simple three step approach that can be summarized by:

1) Feature extraction (Fig. 4.3.b)
2) Feature matching (Fig. 4.3.c)
3) Transformation model computation (Fig. 4.3.d)

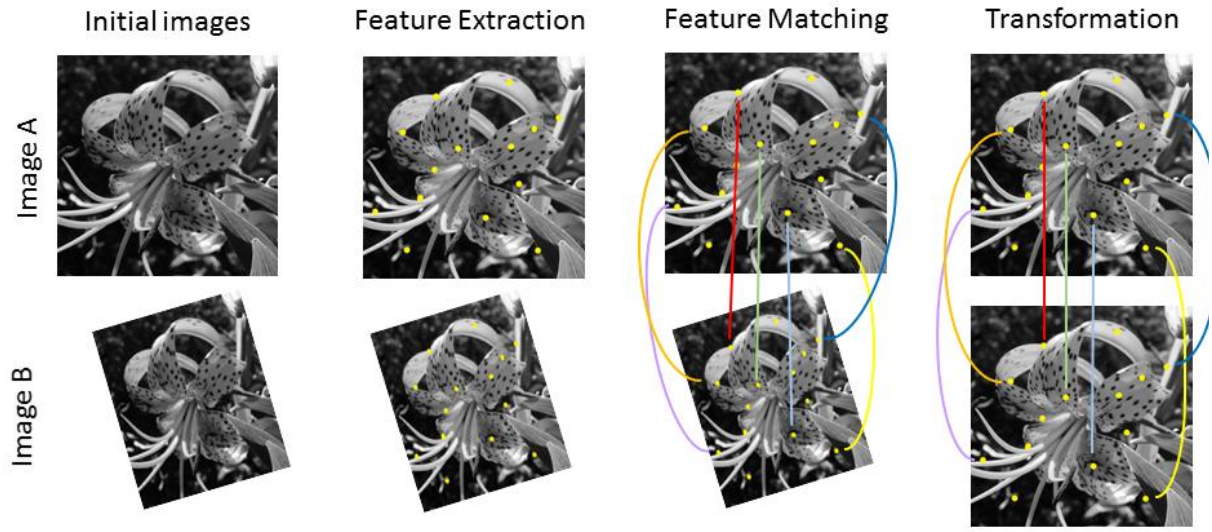

Figure 4.3. SIFT Computation algorithm, (a) Initial images: raw image (top) and the same image shifted, rotated and reduced (scale), (b) Extraction of the keypoint location and descriptor generation in both images, (c) Descriptor matching between two images despites the orientation and scale differences between them, (d) Transformation of image B against image A used as a registration template.

1) **Feature extraction:** Locations of very stable features in the two images to be registered (images A and B) are first extracted separately in both images (Fig. 4.3.b). Their coordinates are computed as the ones of the local extrema (local minima and maxima) of the DoG, difference of Gaussian, found by the subtraction of two differently blurred versions of these images. The Gaussian blur kernel is convolved repeatedly with both images to provide two sets of new images with varying degrees of blur, also called the scale (Fig. 4.4.a). The subtraction between consecutive images of those sets gives the DoG of image A and B (Fig. 4.4.b). This difference of Gaussian act then like a band-pass filter

that preserves only the spatial information between two defined frequencies. It is known that difference-of-Gaussian extrema are very stable across scale (Mikolajczyk, 2002) because of the properties of the scale-space function Gaussian kernel (Linderberg 1998). The scale-space extrema, the local minima and maxima of the three-dimensional matrix computed by piling up the DoG at each scale, define the scale at which an object as the highest response: a small object is detected at fine scale and disappear at bigger scale whereas a bigger object which cannot be detected at fine scale. And thus those locations are suitable for our purpose, because the same extremum are likely to be detected in the two images even when their sizes or orientations are not the same. In summary, keypoints are then extracted as the locations that show extrema of the scale-space difference-of-Gaussian function (Fig. 4.3.c). Low contrast and edge-located points are then discarded because of their instability against Gaussian blur. In conclusion each keypoint location is defined by three parameters: its coordinates in the image and its scale factor, which is the value of the version of the Gaussian blurred image from which it was extracted.

2) **Feature matching:** For each location of the images A and B computed in 1), a keypoint descriptor is generated (Fig. 4.3.b). It is defined as a vector of features locally describing the image properties. Because the transformation model is computed by matching these factors between the two images (Fig. 4.3.c), their values must be defined such was that two similar keypoints from both images can be matched even though one of the images is shifted, rotated, or in a different size compare to the other: the keypoint descriptor must be therefore invariant to rotation, location, image size and other variations such as shear or illumination. The keypoint descriptors are estimated in a window of 8 x 8 pixels around the DoG extrema subdivided in 16 square subzones of 4 pixels (Lowe 1999, 2004). 8 bin-histograms of the image are computed for each subzones and their values concatenated as a 16 x 8 = 128 long vector and normalize to unit length: the feature vector. The feature vectors extracted from image A are mathematically compared with the ones from image B using a nearest neighbor's algorithm and associated with the most similar one.

3) **Transformation model computation:** The matching pair of vectors coordinates (one from image A and the other from image B), are used to compute a model that transform image B to image A (Fig. 4.3.d).

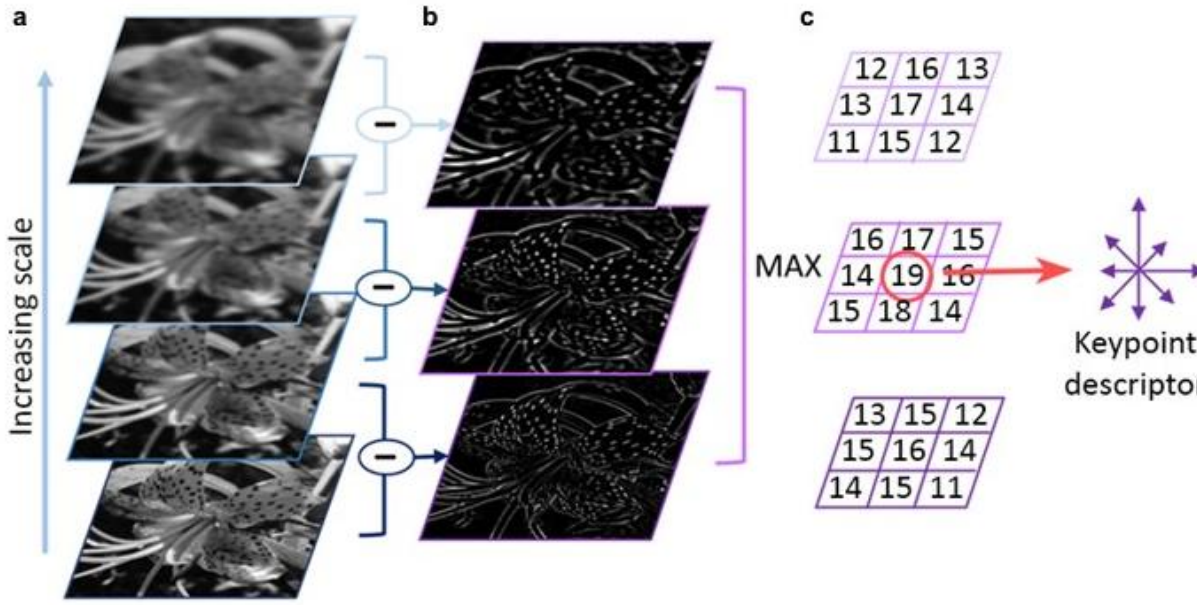

Figure 4.4. SIFT Computation algorithm. (a) Progressive blurring at increasing scales of the raw image, (b) Difference of Gaussian computation: substraction of two consecutive blurred images, (c) Local extrema computation: the extrema of DOG are known to be very stable and will be used as key point location. For each computed extremum a keypoint descriptor representing the local properties of the stable location of the image is computed as a feature vector

SIFT is particularly convenient for our problem of big image registration because the comparison is performed between a small number of vectors instead of a brute-force voxel to voxel comparison in the entire image in all possible relative positions. Indeed, common local features detected are used as landmarks to perform registration: the computation is then dramatically reduced. Moreover, SIFT is known to be robust to scale modification, translation and rotation, and is partially invariant to brightness differences and affine 3D projections.

SIFT has already been implemented in two dimension as a Fiji Plugin called Linear Stack Alignment with SIFT (developed by Stephan Saalfeld in 2008). However, this plugin has a very different purpose: it registers each slice of an image stack using the previous one as a template. This plugin is particularly useful when the slices of a stack are not aligned because of acquisition problems such as wobbling of samples or microscope stages. However, it does not compensate for possible tilting of image planes, an important aspect of our problem. We want to register two different images of the same object, which may have not only translational or rotational misalignment but also tilting misalignment.

d. REGISTRATION ALGORITHM OUTLINE

The algorithm we developed based on this technique is a four-step procedure that can be iterated until satisfying results:

1) The common part of the neighboring (front and back) stacks, also called overlap is estimated (Fig. 4.5.a).
2) The rotation around z-axis, and the translation along x and y-axes are computed and fixed by comparing cross-sections of similar positions within the overlap (Fig. 4.5.b).
3) The tilting around x-axis, and the translation along y and z-axes are computed and fixed by comparing cross-sections of similar positions within the overlap (Fig. 4.5.c).
4) The tilting around y-axis, and the translation along x and z-axes are computed and fixed by comparing cross-sections of similar positions within the overlap (Fig. 4.5.d).

We used a two steps procedure to register two volume data substacks using SIFT. First, the overlapping portions of the two substacks are identified. And second, optimum degrees of translation and rotation of the substacks are calculated for all the six degrees of freedom to achieve the best match within the overlapping volume. These two steps can be repeated to improve matching precision. Finally, using the obtained parameters, the entire back substack is transformed and merged with the front one using a linear blending.

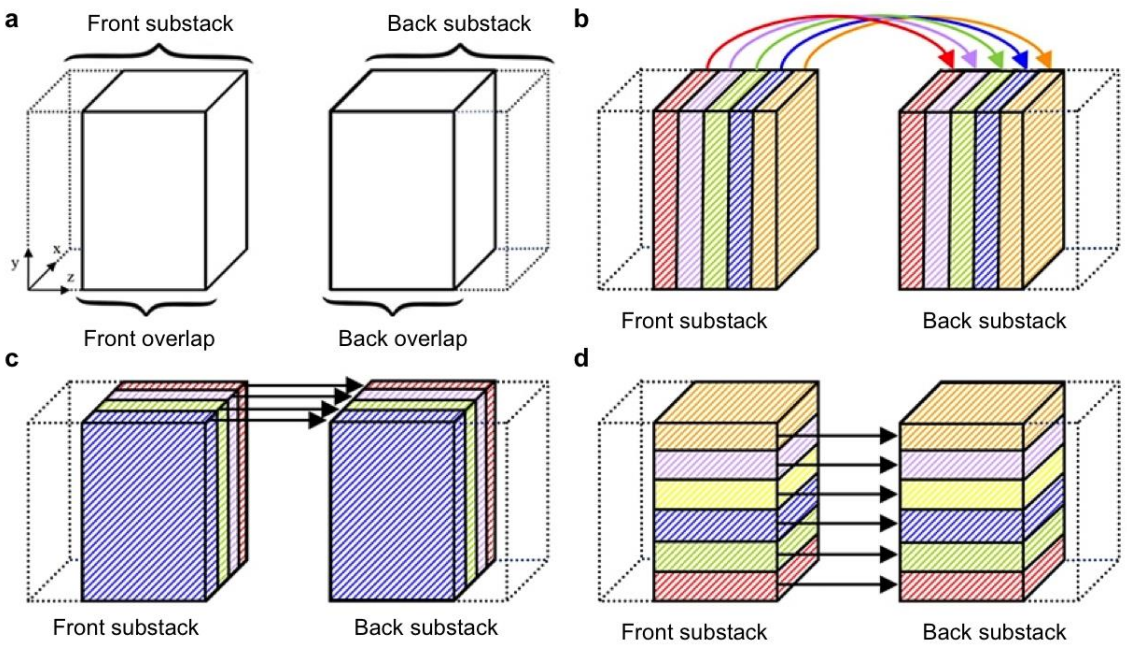

Figure 4.5. 3D registration by three consecutive 2D comparisons: after overlapping volume between substacks is identified (Fig.5), SIFT comparison is performed between spatially corresponding pairs of partial-MIP slices, first in the x-y plane, (b) and then x-z plane, (c) and finally y-z plane (d).

Step 1: Identification of the image overlap

The identification of the overlapping volumes between substacks is done under an assumption: the tilting between the planes of the two substacks is small enough to find important similarities between image slices of similar depths. Thus, instead of long and fastidious 3D comparison, a 2D comparison of section images should give good approximations.

To detect the overlapping volumes between substacks, we employed two alternative approaches so called slice-by-slice and block-by-block comparisons. The first approach, compares the last single section of one substack with all the sections of the other substack using SIFT (Fig. 4.6.a). This approach made use of the feature of our datasets that tilting between the planes of the two substacks is usually small enough to find important similarities between image slices of the corresponding depths within the overlap. A section of a substack, which is spread along the x-y

plane, is represented as a collection of local feature vectors whose positions are identified as maxima or minima of a difference-of-Gaussian function applied in a specific scale space. At each position a feature vector describing the local image region (scale, orientation, etc.) is computed (Fig. 4.6.a2). Features of the last section of the front substack extracted in this way are compared with those extracted from each section of the back substack (i.e., at different levels along z-axis) to find the best possible match using a nearest neighbor's algorithm (Fig.4.6.a3). The higher is the number of matching features between the front slice and the back slices, the more similar are the pair of slices. We plot this number according to the depth of the back slices. The maximum of the bell-shape curve defines therefore the boundary of the overlap (Fig. 4.6.a4). In practice, one can also estimate the overlapping volume beforehand and compare only the sections within that range to reduce computation time.

Slice-by-slice comparison requires long computation time when the substacks consist of numerous sections. Moreover, when the tilting between the two substacks is big, similarity between sections is often not sufficient for identifying corresponding sections. For those reasons, we developed an alternative approach, block-by-block comparison (Fig. 4.6.b). In this approach we first split the entire substack into several blocks, and make the maximum intensity projection of the sections within each block (partial MIP). SIFT comparison is then performed between the partial MIP of the last block of one substack with the partial MIP of each block in the other substack (Fig. 4.6.b1). The thickness of the blocks is determined by the parameter "splitting". For example, if the splitting parameter is set at 2, the substacks will be divided into two blocks. The partial MIP of the last block of the front substack will then be compared with the MIPs of the two back-substack blocks and the best match is selected. The selected back-substack block is further split incrementally, and compared with the equally split last block of the front substack (Fig. 4.6.b2), until the successively split blocks contain only one section (Fig. 4.6.b3&b4). The splitting parameter can be set by the user, and the effect of its choice will be discussed later.

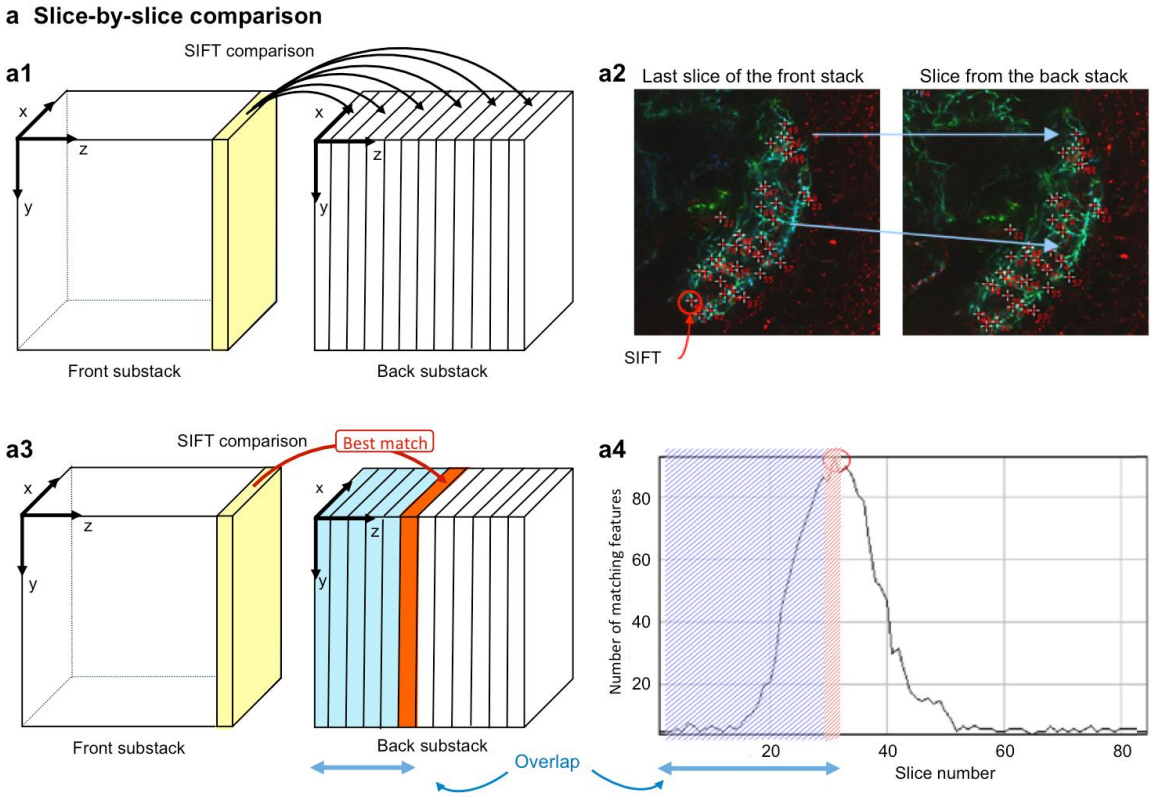

Figure 4.6. Two methods of overlap detection between substacks. (a) Slice-by-slice comparison: (a1) the last section (x-y plane) of the front substack is compared to each section of the back substack along the z-axis using (a2) SIFT comparison until (a3) the best match is found. (a4) Overlap correspondence curve, which shows the number of corresponding SIFT features identified between the last section of the front substack and each slice of the back substack. The highest peak of the curve corresponds to the position of overlap (red section in a3).

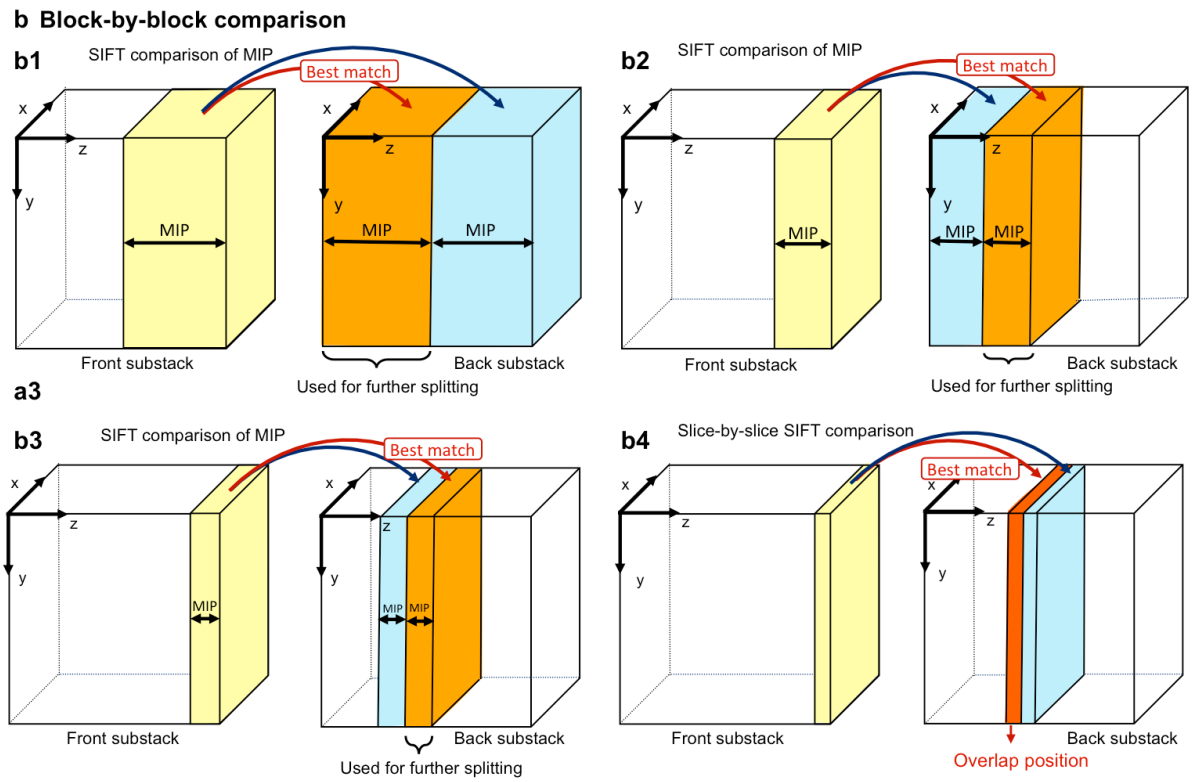

Figure 4.6. Two methods of overlap detection between substacks. ((b) Block-by-block comparison: (b1) The back substack is split into several (in this case two) blocks, and a maximum intensity projection (MIP) image is calculated for each block. They are compared using SIFT with the MIP image of the block of similar size (light orange) located in the deepest part of the front substack. The best matching block (light purple) is selected. (a2) The selected block is split again into several blocks, whose MIPs are compared using SIFT with the MIP of the corresponding thickness from the front substack to select the best-matching block (light purple). (b3) This process is repeated with decreasing thickness of blocks until each block contains only one section (b4). The position of overlap is identified as the best matching section of the back stack (red section) compared to the last section of the front substack (light orange)

Step 2: Corrections

Both slice-by-slice and block-by-block comparison identify a section of the substack that corresponds to the last section of the other substack, thereby identifying the overlapping volume between the two substacks. A precise registration is then performed using only the data of the overlapping portion. A SIFT-based comparison performed on slices of similar depth computes an

approximate transformation model of the back stack against the front stack in translation along x- and y-axes and rotation around z-axis. However, the two substacks registered in this way still contain two types of errors. First, resolution of the translation along z-axis may not be optimum, and second, rotation around x- and y-axes is not yet compensated (tilting). Comparison of single sections within the overlapping section, moreover, often do not contain enough amount of corresponding signals, so that extracted features of a section of the front substack may match with only a few features of a section of the back substack. To overcome this problem, instead of comparing single sections, we again used maximum intensity projection of several sections (partial MIP) that will erase the bias introduced by x- and y-rotation angles by flattening signals of multiple sections into one slice (Fig. 4.7).

After the overlap detection step described earlier (Fig. 4.6), we then perform three successive rounds of registration in three orthogonal planes (Fig. 4.5.b-d). First, the overlapping volumes of the front and back substacks are re-sliced along the z-axis to obtain cross-section slices in the x-y plane (Fig. 4.5.b). We then use the SIFT-based registration to the cross sections of the stacks. The partial-MIP slices of the front substack are compared with the partial-MIP slices of similar depths of the back substack (Fig. 4.8.a). Comparison between thick partial-MIP slices enable robust matching regardless of sample tilting. The model of translation in the x-y plane and rotation around z-axis of the back substack compared to the front substack is then computed by SIFT-based evaluation.

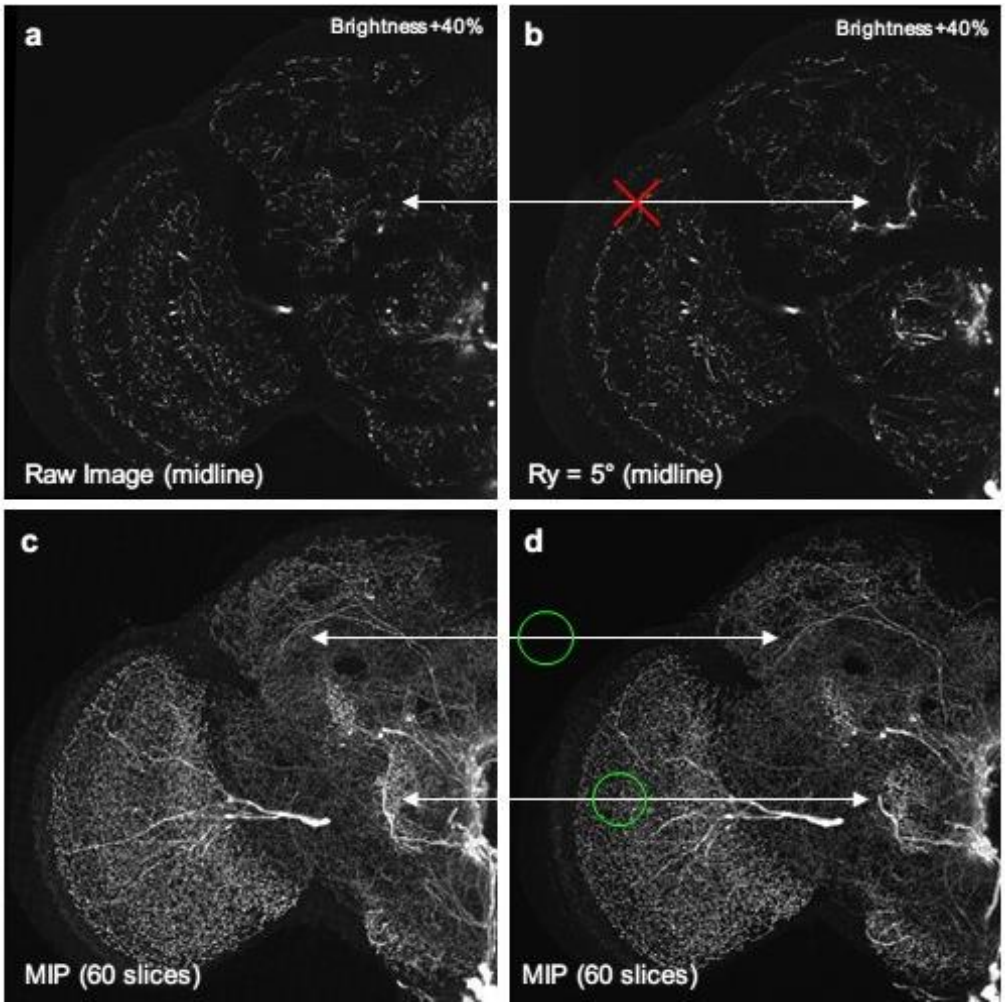

Figure 4.7. Single slices comparison vs MIP comparison, (a) central slice of a real stack, (b) central slice of the same real stack after 5 degree rotation around y, (c) partial MIP (60 slices) around the central slices of the raw stack, (d) partial MIP (60 slices) around the central slices of the rotated stack.

Second, the registered substacks are re-sliced along x-axis to obtain cross sections in the y-z plane, and partial-MIP slices are generated from these sections (Fig.4.5.c). Slices of similar depth are compared between front and back substacks to calculate translation parameter in the y-z plane and rotation parameter around x-axis (Fig. 4.8.b).

Finally, the registered substacks are re-sliced along y-axis to obtain cross sections in the x-z plane (Fig. 4.5.d), and translation parameter in the x-z plane and rotation parameter around y-axis is computed by comparing partial-MIP slices (Fig. 4.8.c).

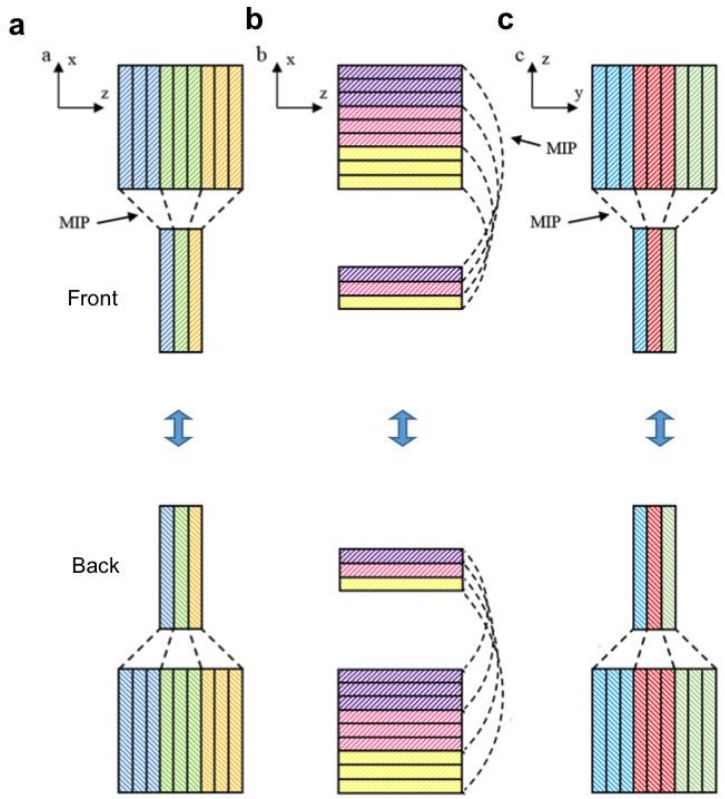

Figure 4.8. Creation of partial-MIP slices along z, x and y. Each partial-MIP slice contains more signals for feature extraction compared to thin original sections, which also results in more matching features even when sections of the front and back substacks are slightly tilted. Reduction of the total number of slices also reduced the computation time, (a) partial MIP parallel to x-y plane, (b) partial MIP parallel to y-z plane, (c) partial MIP parallel to x-z plane

Translation and rotation of the voxels of a substack involve recalculation and interpolation of voxels, causing slight degradation of spatial resolution. It is important to avoid multiple recalculations to minimize such effect. Therefore, instead of applying the calculated translation and rotation model incrementally to the substack data that are registered already in the previous step, we combined the translation and rotation parameters calculated by all the previous registration steps and applied them to the original substack data.

Because the correction of the tilting and the successive registration often modify the relative position between the two stack and then the exact position of the overlap, at the end of the registration step another round of overlap detection is performed similarly to the first one (Fig.

4.6.a) to guaranty an exact stitching between the front and back substacks. Even if the user selects the block-by-block comparisons, the last round of overlap detection is always performed using the slice-by-slice method to ensure a perfect stitching between the two stacks.

In conclusion, the 2D-SIFT-in-3D-Space registration process consists of one overlap detection step and three 2D-registration steps that are performed iteratively. First, slices in the x-y plane are compared to evaluate the rotation around z- and translation along x- and y-axes. Second, comparing in the y-z plane, rotation around x- and translation along y- and z-axes are computed. And third, comparison in the x-z plane computes parameters for y-rotation and x- and z-translation. The set of these three iterative steps can be repeated as many times as necessary to further improve the precision of registration.

e. REGISTRATION IMPROVEMENT

The usage of partial-MIP slices instead of single sections (Fig. 4.7), besides its advantage of reducing the impact of rotation of the substacks in the directions other than the studied, can also accelerate the computation time by decreasing the total number of comparison between slices and by increasing the number of feature vectors due to denser signals in each partial-MIP slice compared to single slices of the original stack. The quality of registration can therefore be improved by increasing the thickness of the partial-MIP slices, especially in the samples that present bigger rotation angles around x and y. However, one must be careful when selecting the partial-MIP size, because projecting too many sections into one slice can lead to saturated signals in too many pixels of the MIP slice image, reducing the number of detectable features.

The slice-by-slice comparison method as described before, however, works only if the tilting around x- and y-axes between the front and back substacks is very small. Otherwise, signal distribution and therefore extracted features of a section of the front substack may not match with any sections of the back substack. The effect of using partial MIP is shown in Fig. 4.9. In this sample the back substack is tilted against the front substack so that, when the two sections that

show comparable structure in the upper part of the image are selected (green circles in Fig. 4.9.a&b), the lower part appear significantly different. SIFT matching score of the slice-by-slice comparison show bimodal curve (Fig. 4.9.e) instead of the expected bell-shaped curve (cf. Fig. 6.a4). The first peak (around the 120th section in this case) corresponds to the matching of the lower part of the front and back substack images, whereas the second peak (around the 150th section) indicates a similarity at the upper part of the images.

Single section images contain so few features that reliable computation of a transformation model is not possible. Indeed, a transformation model computed from such image comparison will then tend to register the left part but will probably increase or at least not improve the shift of the right part. By using partial MIP, one can increase the similarity between two tilted substack by flattering the image as it was illustrated in Fig. 4.7. When we make partial MIPs of 50 sections within the overlap (Fig. 9.c&d, central panels), comparable features can be detected throughout the images (green dots), increasing the accuracy for computing the transformation models along x-y plane and rotation around z-axis. To compensate the rotation around x-axis, the substacks were then re-sliced with the thickness of 50 voxels and partial MIP images were generated (Fig. 4.9.c&d, left panels). In this sample tilting between the two substacks was mainly due to a big rotation around x-axis (magenta rectangles), and fixing this rotation will greatly improve the similarity between the front and back substacks. Finally, the substacks were re-sliced again with the thickness of 50 voxels to correct tilting around y-axis (Fig. 4.9.c&d, top panels). At the end of this first iteration, the similitude between the two substacks is increased drastically, as can be seen through the overlap correspondence curve (Fig. 4.9.f) that is much higher and sharper than before (Fig. 4.9.e). The procedure was repeated several times for better accuracy, but no further big changes could be noticed as the curves remained similar (Fig. 4.8.f).

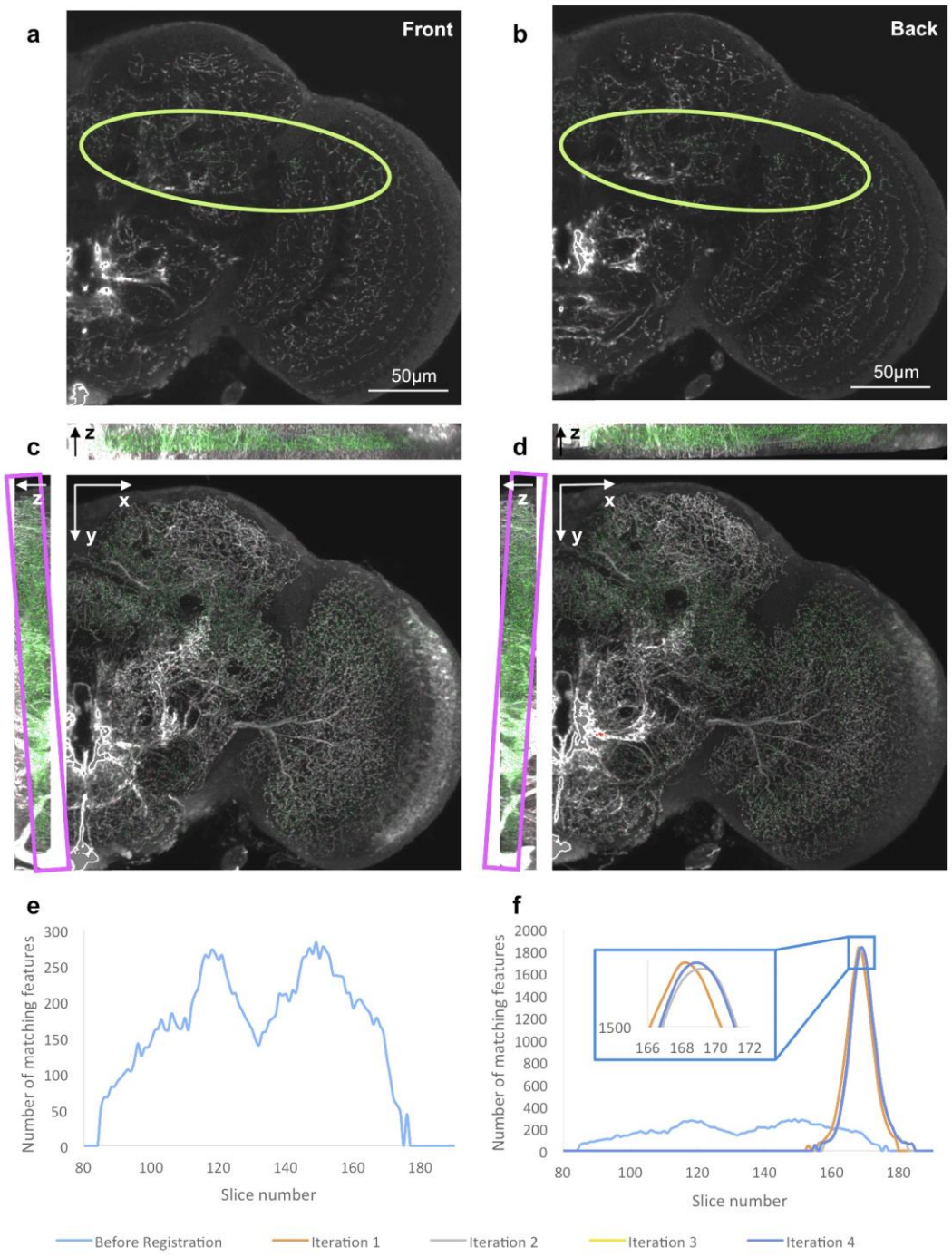

Figure 4.9. Example of SIFT registration using partial-MIP. (a, b) Single section of corresponding location in the front (a) and back (b) substacks. Matching features are identified only in a narrow space (green circle), making it impossible to register them precisely. (c, d) Partial MIP (50 slices) along the three directions from the front (c) and back (d) substacks. Magenta rectangles indicate tilted substacks. (e) Overlap correspondence curve before registration. (f) Overlap correspondence curve after 4 iterations. The curves are higher and sharper compared to the one before registration. Scale bars = 50 µm.

f. IMPLEMENTATION FOR FIJI

As mentionned before, we based our code on the implementation of SIFT in 2D given in the Fiji/ImageJ plugin called Linear Stack Alignment with 2D SIFT (developed by Stephan Saalfeld in 2008 and published in 2009 (Preibisch et al.)). This plugin aligns each 2D section of an image stack using the previous one as the reference. It can be used, for example, in the cases when serial optical sections in a substack are not aligned exactly because of the wobbling of samples or microscope stages during image acquisition, or when the serial section preparations are not aligned before image acquisition, such as in paraffin sections or transmission electron microscope images. It does not compensate for possible tilting of image planes, though. By contrast, our goal is to register and stitch two independent substacks in 3D because these substacks may have not only translational or rotational misalignment but also tilting misalignment.

As an implementation of 2D-SIFT-in-3D-Space, we developed a Fiji/ImageJ plugin module called 2D-SIFT-in-3D-Space Volume Stitching (Fig. 4.10). The interface of this plugin is divided into seven categories: Image selection, overlap detection method, additional channels, 3D registration parameters, SIFT parameters, filtered image selection, and fusion method.

The first section determines the two substacks to be registered and the direction in which they should be concatenated. Although in this paper we primarily describe the method for stitching front and back substacks along z-axis, the plugin can also be used for stitching two substacks that are aligned side by side in the horizontal (x-y) plane.

The second section determines the overlap detection method. Block-by-block comparison is default, because it is faster and works well for most cases (discussed later). In case of block-by-block comparison the number of substack split should be set. For slice-by-slice comparison estimated size of overlap (in the number of sections) should be set to limit comparison of unnecessary sections.

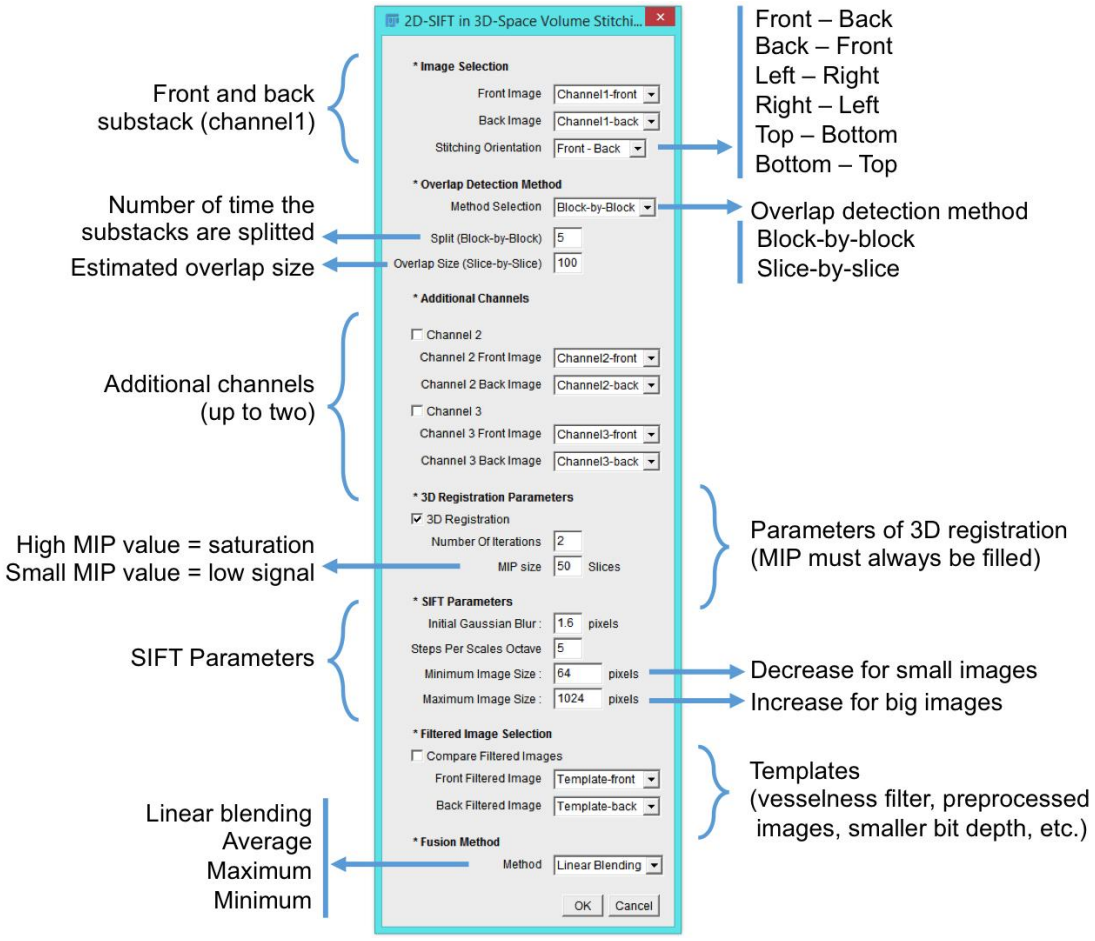

Figure 4.10. Control panel of the *3D-SIFT Volume Stitching* plugin, implemented for ImageJ/Fiji. The complementary front substack and back substack are selected in Image Selection as well as the overlap size if known. Additional channels specify other channels of the same substacks to be stitched. Parameters of 3D registration panel includes the number of iterations (number of zxy registration) and the size of the partial-MIP. SIFT parameters panel specifies initial Gaussian blur, the number of successive blur (Steps Per Scales Octave) and the maximum and minimum image size. If needed, check the Use Template box to select the template files – the substacks of manipulated images that are used for SIFT matching but not for the final image stack (front and back).

The third section is for multi-channel images. Many laser scanning microscope images feature signals of multiple channels. Image substacks of all the channels should be registered and stitched in the same way, but registration of some channels may be more difficult than others. The plugin allows users to register the substacks using the data of the channel that contain more features

and are therefore easy to register, and apply the same registration parameters to the registration of other channel data.

The fourth section more specifically focuses on the modality of registration: 3D (rotation around x-, y- and z-axes and translation along x-, y- and z-axes, 3D by default) or 2D (rotation only around z-axis and translation around -x, y- and z-axes, i.e., no tilting compensation), the number of time the algorithm will loop (number of iterations), and the partial MIP size (see the previous chapter). In our samples partial MIP of about 50 sections (corresponding to 10-µm thickness) provided the best results for the images of neuronal fibers, and about 20 sections for the images of continuous-looking background labeling such as those with the nc82 antibody (Wagh et al., 2006), which labels synaptic neuropils broadly according to the density of synaptic active zones.

The SIFT parameters are defined in the fifth section. Following its original implementation (Saalfeld 2008; Saalfeld et al. 2010) we provide three key parameters: initial sigma of the Gaussian law used to blur the image, steps per scale octave (the number of times the image will be blurred), and the image size (minimum and maximum).

The plugin also allows users to use preprocessed (filtered) images instead of original stack images to calculate registration parameters with SIFT comparison (sixth section). The transformation model will be computed by comparing the preprocessed images, but the resulting model will be applied to the original data. To use this feature, check the “Compare Filtered Images” box and specify the file names of the preprocessed images. Applying various filters to the original front and back substacks may improve registration. For example, one can use a vesselness filter to enhance tubular structures of neuronal fiber images, local contract filter to enhance faint signals, or denoising filter to eliminate misleading signals. Another effective way of using preprocessed images is to perform registration in 8-bit images instead of original images with larger bit depth (e.g., 12-bit or 16-bit), which will significantly reduce computation time. However, stitching of such preprocessed images may not be scientifically pertinent for further study, because it may affect signal intensity and distribution as well as bit-depth resolution. To provide users with

flexibility of choice, final concatenation can be performed either with the preprocessed data or unprocessed raw image stacks.

Finally (seventh section), several methods are provided for computing the intensity of the voxels in the overlapping part from two substacks.

2D-SIFT-in-3D-Space Volume Stitching and Progressive Intensity is written in Java and function as plugin modules of Fiji/ImageJ. The source code of this plugins is available via Github (https://github.com/cmurtin/2D-SIFT-in-3D-Space). Simulation of confocal microscope noise was performed using Matlab (Natick, Massachusetts). The script code and experimental data for simulation are available via http://jfly.iam.u-tokyo.ac.jp/confocal_simulator/.

Our plugin can efficiently perform very fine adjustments and precisely register small objects such as neuronal fibers and presynaptic sites. Fig. 4.11 shows the performance of our registration algorithm for two stacks of neurons of the optic lobe of the Drosophila brain at a voxel resolution of 0.2 x 0.2 x 0.2 µm. The front substack (Fig. 4.11.a, shown in green in Fig. 4.11.c) was registered and superposed to the back substack (Fig. 4.11.b, shown in magenta in (Fig. 4.11.c). In the overlaid image (Fig. 4.11.c), green and magenta cast should appear on the opposite sides of the objects if two stacks are out of alignment. The lack of such cast attests perfect registration. (Note: green or magenta cast that appears on the entire object is caused by the voxel intensity differences between front and back substacks.)

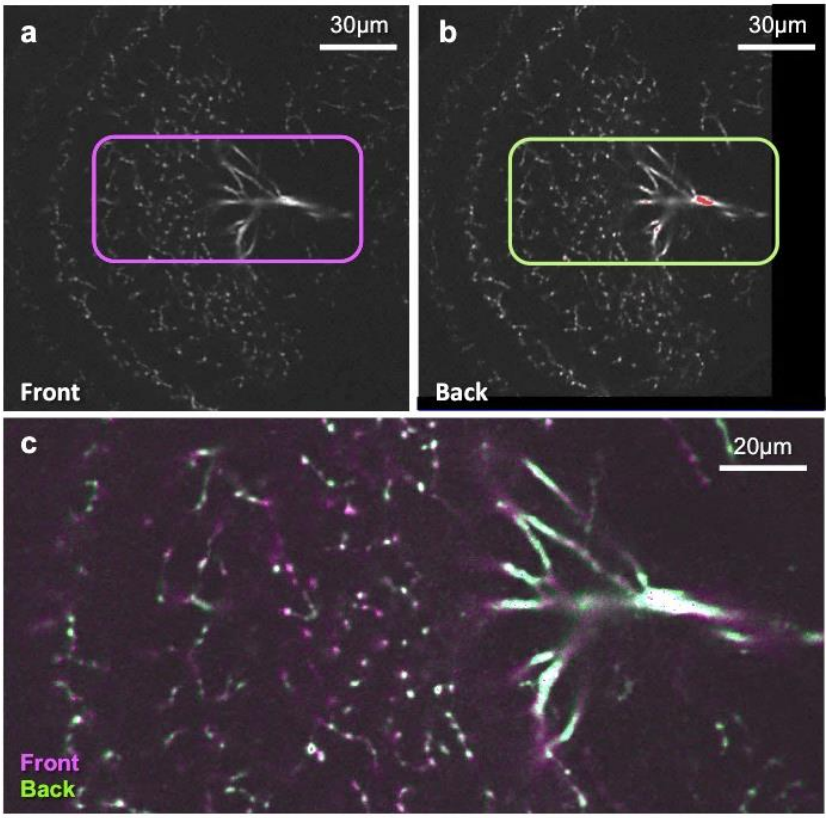

Figure 4.11. Registration and superposition of a section from the front substack (a, green) and its corresponding section from the back substack after registration (b, magenta) of the octopaminergic neurons of the Drosophila Melanogaster optic lobe (voxel resolution 0.2 x 0.2 x 0.2 µm), (c) Close-up view of the superposition of the two sections (rectangles in upper panels). Scale bars = 30 µm (a,b), 20 µm (c).

2. ALGORITHM VALIDATION

Visual examination of the 2D-SIFT-in-3D-Space Volume Stitching results appears to be very good, as shown in Fig. 4.11.c. However, this is not enough to assess the accuracy and efficiency of our plugin which requires a quantitative analysis to evaluate its precision. Raw data cannot be used for this purpose because the relative shifts between the two stacks are unknown. The quantitative evaluation of its precision we need a set of sample image substacks for which degrees of rotation and tilting are precisely known. Such quantitative comparison is difficult, because laser-scanning image stacks obtained from real samples contain uncontrollable factors such as noise and signal attenuation, making it difficult to register them precisely even with human eyes.

Quantitative evaluation may in principle be possible, when one takes a single image stack, divides it into two substacks with certain overlap, rotates one of them at given degrees, and subjects the two substacks to the registration software to see whether it will rotate the pre-rotated substack back at the same rotation angles. This approach, however, does not work because the divided substacks have near-identical image quality, making precise registration much easier, whereas the two substacks obtained from real samples often appear considerably different: The last section of the front substack generally appears less sharp than the corresponding section in the back substack, because the former is much further from the sample surface than the latter. Two substacks of real images are then considerably different and make a precise registration much more difficult. In conclusion, simple extraction and rotation of an image substack is not suitable for this purpose, but uncontrollable factors such as noise and signal attenuation should also be simulated.

To address this issue we created an in silico simulator of laser-scanning microscopy images (Fig. 4.12):

1) Generation of two overlapping three-dimensional image stack of binary tubular structures (neuronal fibers).
2) Rotation of the back substack with given angles.
3) Noise filtering to simulate the one of laser scanning microscopy depending on the depth from the front and back sample surfaces.

Figure 4.12. In silico simulation of confocal microscopy images. (a) Overview of the process. First, binary mask of the signal portion is generated from a real dataset of laser scanning microscopy. The mask appears sharp and bright regardless of the depth of the section in the sample. Next, computed noise in the signal (fibers) and background according to the depth in the virtual sample is convoluted to the binary masks. Finally, the signal and background images are merged. (b) Real data. (c) Binary mask of the signal structure. (d) In silico simulation of the section image if it is placed at 30 µm from the surface. (e) The same section if it is placed at 90 µm from the surface. Note that the signal appears darker and more blurred and background noise appears higher in (e) compared to (d), which is consistent with the image degradation in real confocal microscopy image stacks.

(f) Generation of virtual substacks from a single image stack. A single image stack (in this example the thickness of 300 sections = 120 µm) is divided into two overlapping substacks (with the thickness of e.g., 250 sections = 100 µm). Noise simulation is then applied to the front substack from front to back to simulate the imaging from the frontal side, and from back to front to the back substack to simulate the imaging from the back side. Different levels of noise will be applied to the same section (red line) according to the distance from the front and back sample surface.

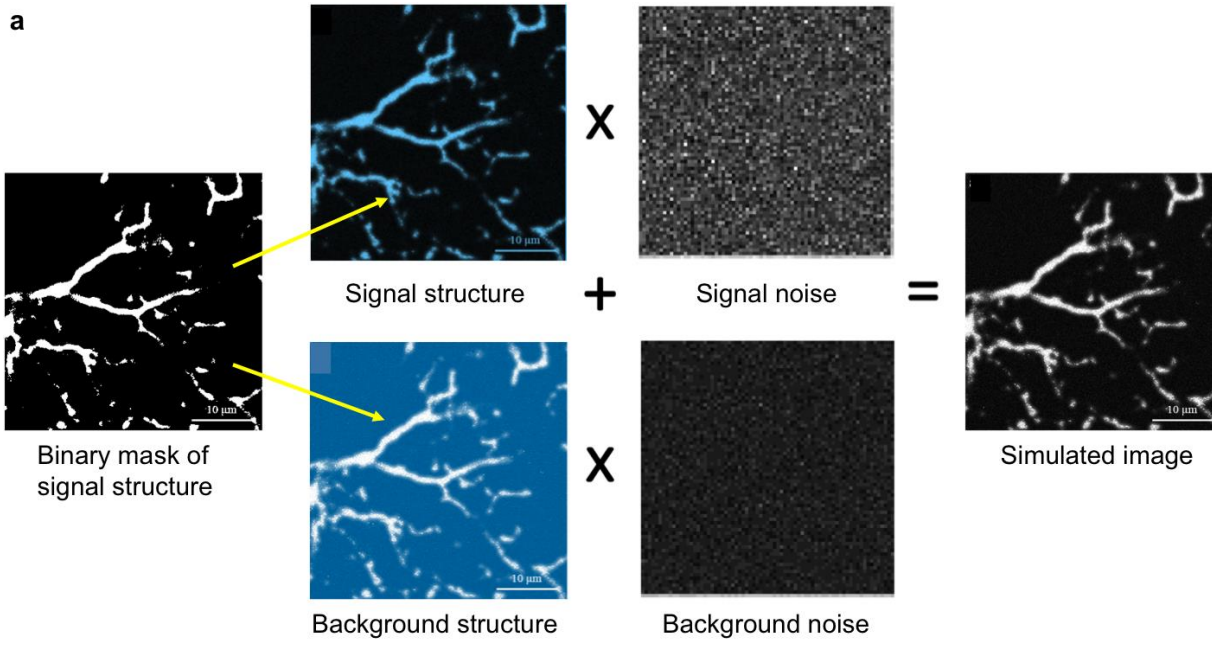

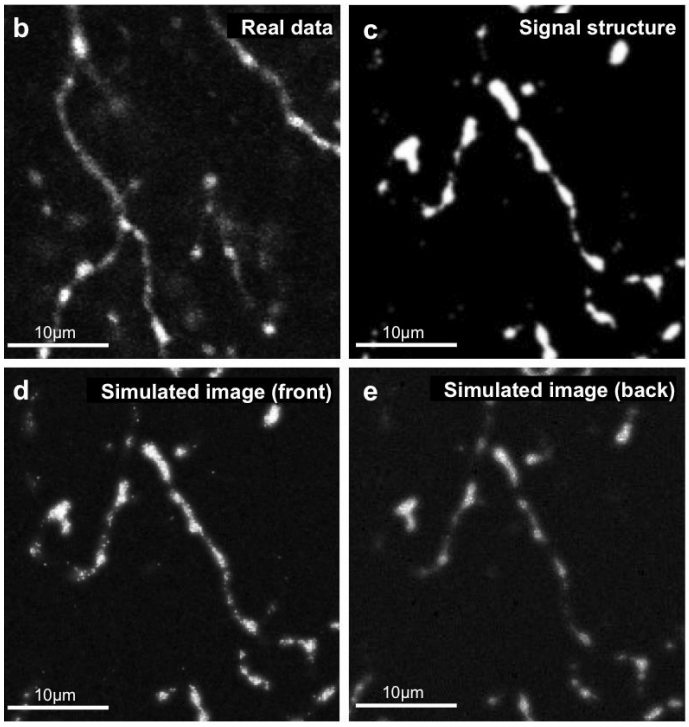

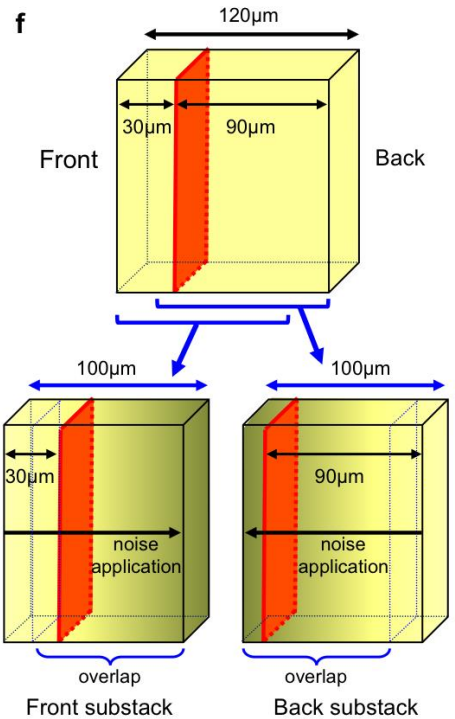

a. BINARY MASK GENERATION

In order to create 3D binary mask of tubular structure we first took a set of real laser-scanning images of neuronal fibers (Fig. 4.12.b&Fig. 4.14.a) and made binary-segmented image with no noise by thresholding and smoothing the real image data (Fig. 4.12.c&a, left, Fig. 4.14.b) using the Li thresholding algorithm (Li et al. 1993), which has empirically been giving the best fiber segmentation on our data. Li algorithm is also known as minimum cross-entropy thresholding, and has the particularity to automatically choose the threshold value for each section of the stack which is very useful for our data since the intensity signal decreases with depth. For this it minimizes the cross entropy between the original image and its thresholded version

b. NOISE FILTERING

To develop such a simulator, we first have to understand the nature of noises in our microscopy data. Because the neuronal fibers labeled in our samples occupy a very small volume in the entire brain, the number of voxels with high-intensity signals is rather small. The voxels other than that of neuronal fibers, i.e., the backgrounds, tend to have intensity that is slightly higher than zero, causing background noise (Fig. 4.13). It is known from a previous study (Herberich et al. 2012) that the noise of a 3D image stack acquired by fluorescent microscopy follows a Gamma law of shape k and scale θ:

$$f(x;k;\theta) = \frac{x^{k-1}e^{-\frac{x}{\theta}}}{\theta^{k}\Gamma(\mathrm{k})} \; for\; x > 0 \; and \; k, \theta > 0$$

Importantly, the parameters k and θ of the gamma law are not the same in the signal and in the background and also differ depending on the depth. Thus, we must estimate those parameters for two different parts of the image: the signal (in our case neuronal fibers) and the background. To this end, we have to first segment the image stack into corresponding parts.

For this purpose we made a binary mask of the fibers by thresholding each section of a real image stack of the brain (Fig. 4.14.a) as described in the previous section. The values over this threshold comprise the signal and the mask values were set to 1 to these voxels, whereas the values under the threshold belong to the background and the mask values were set to 0 (Fig. 4.14.b). The fiber signal is then extracted by multiplying this mask with the original intensity values of voxels (Fig. 4.14.c), whereas the background signal is obtained by the multiplication of the inverse of the binary mask and the original voxel values (Fig. 4.14.d).

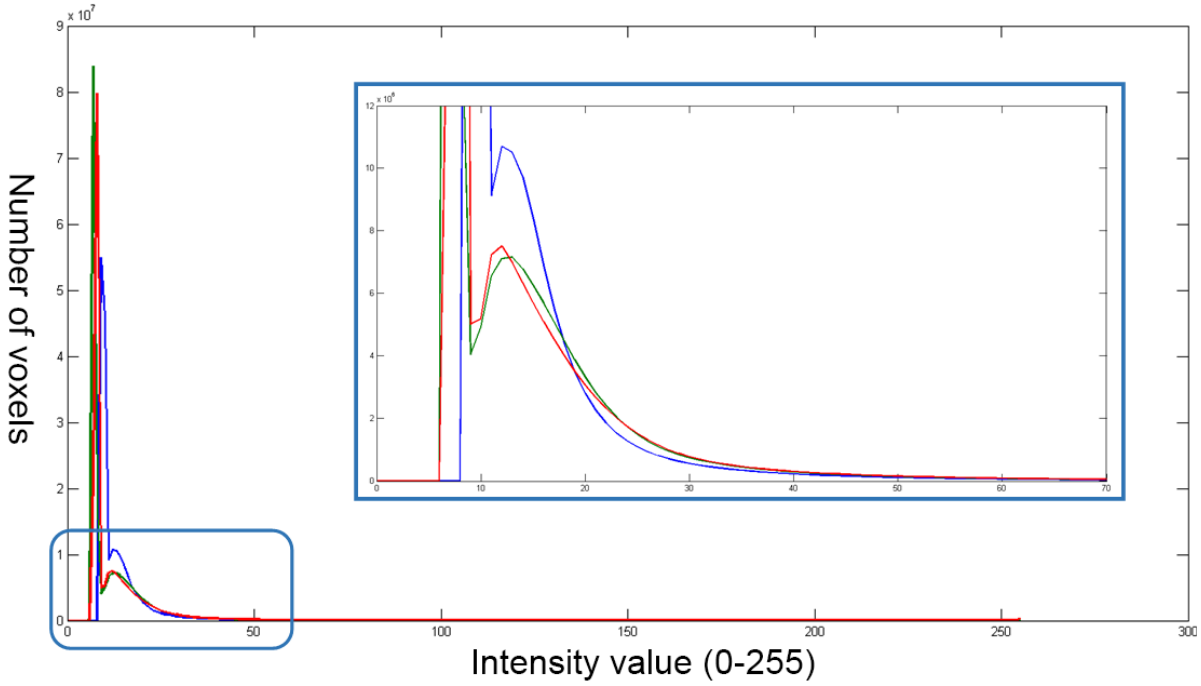

Figure 4.13. Intensity histogram of three image stacks of the Drosophila Melanogaster brain taken by confocal fluorescent microscope. The number of voxels below intensity value 10 is extremely high due to the background noise.

To evaluate the nature of the noise observed in our datasets, we fit a gamma distribution and estimated the law parameters shape (k) and scale (θ) for the thresholded signal and background images throughout the sections of the front and back substacks of five different brain samples (Figs. 4.15-18) using a Matlab script. Because the sections near the surface of our samples tend

to contain saturated images of large and round cell bodies, which affect the evaluation of noise evolution in the signals of neural fibers, we discarded the first 50 sections (corresponding to 10 μm) of each substack from evaluation.

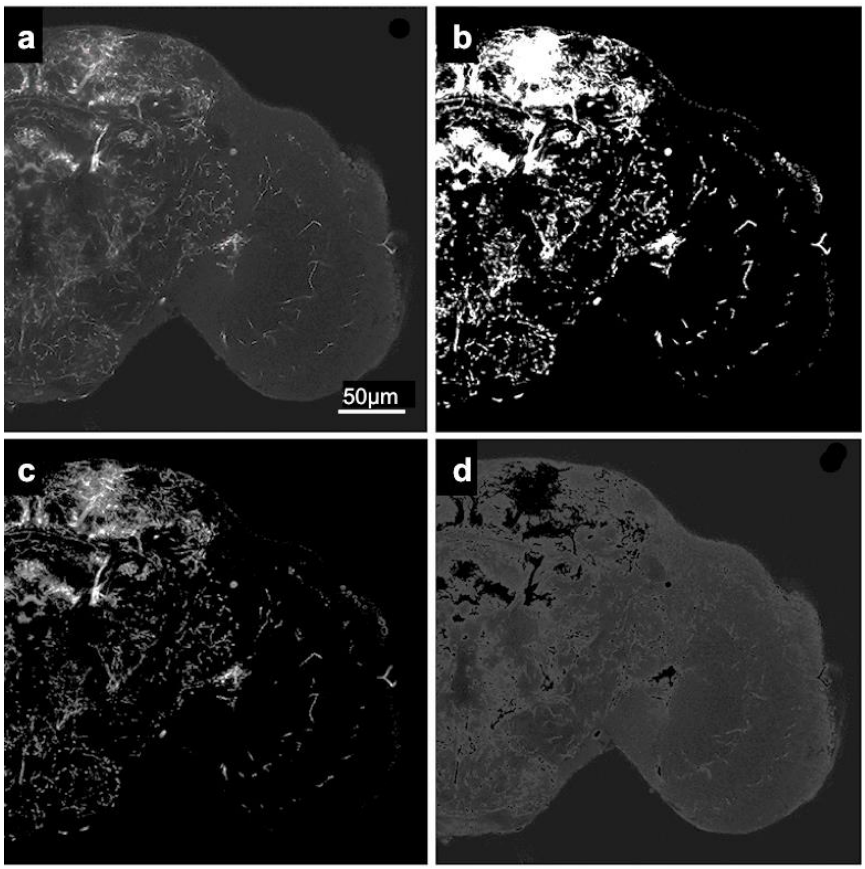

Figure 4.14. Noise estimation example for an image of octopaminergic neurons in the Drosophila brain. Image intensity is enhanced to show dark noises. (a) Original image. (b) Binary image (threshold = 25). (c) Signal segmentation (image within the binary image mask b). (d) Background segmentation (signal outside the binary image mask b).

We repeated this process to evaluate the noise in the signal and background portions of the back substacks of the same samples (Fig. 4.18). We again discarded the first 50 sections from evaluation because of the saturated signals of many cell bodies.

By analyzing the curve of the two parameters for the four different modalities (front vs back and signal vs background), it is obvious that the noise of a confocal microscope behave very differently depending on the object.

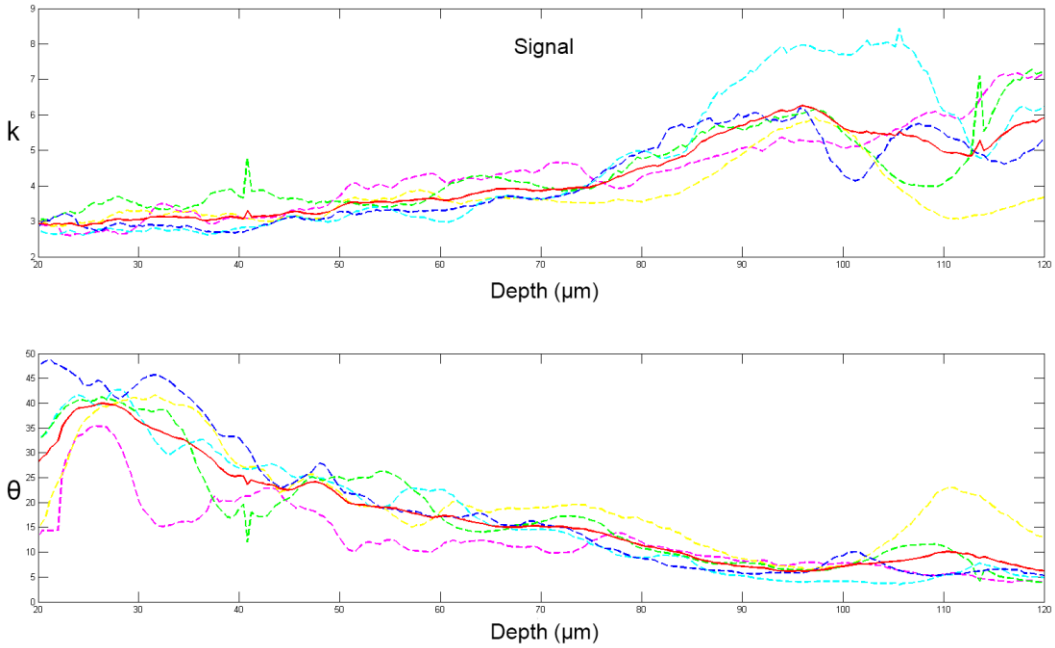

Figure 4.15. Evolution of the parameters k (top panel) and θ (bottom panel) of the gamma law of the microscope noise in within the thresholded portion of the neural fiber signals in the front substacks of five different brain samples and there average (red). The first 20 µm, which contains mostly the image of round cell bodies, are excluded from evaluation.

In the thresholded portion of the neuronal fiber signals of the front stack, the two parameters k and θ show a symmetric evolution: k is increasing, whereas θ is decreasing with the depth (Fig. 4.15). Because the scale parameter θ indicates the statistical dispersion of the Gamma distribution, the smaller θ is, the less the distribution is spread out. The decrease of θ with the depth is coherent with the global decrease of the signal intensity observed in deep layers of the image stacks. The experimentally estimated average value of θ is globally rather stable within the sample except at the beginning and the very end of the image stacks. We also can notice that, in (Fig. 4.16), the standard deviation (dashed blue) is relatively close to the average (red) traducing consistency within our samples except at the beginning and the very end of the image stacks which can be explained by the quality of our image stack: in the upper (shallow), the signal is saturated and bottom (deep) parts of the samples tend to show a low signal intensity.

Whereas θ characterized the statistical dispersion of the Gamma distribution k indicates the shape of the distribution: the increase of the shape parameter k with the depth traduces the

convergence of the shape of the Gamma distribution towards a Gaussian. The standard deviation becomes broader in the sections deeper than 100 µm which means that the estimation of this parameter in deep layers of the stacks seems less accurate than those in the layers near the surface (Fig. 4.16) because of higher average and bigger fluctuation in the curves of k of each sample.

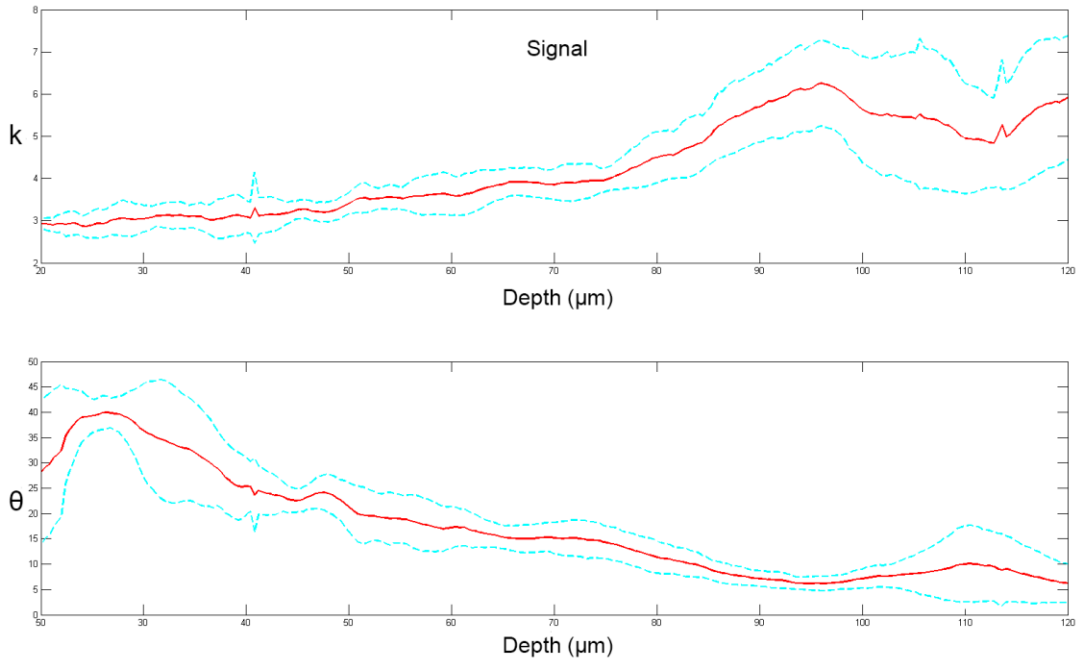

Figure 4.16. Evolution of the average and standard deviation (n=5) of the parameter k (top panel) and θ (bottom panel) of the gamma law of the microscope noise in the signal within the front substack after removing 20 µm (cell bodies).

The evolution tendency in the background portion of the k and θ parameters is similar than in the signal: k increases while θ decreases with depth (Fig. 4.17). However, the values of k and θ appear to be very different. Indeed, k is much smaller in the signal than in the background, thus the background noise tends to be Gaussian in the whole stack. On the contrary, θ is more than 10 times smaller in the background compared to the signal, which means that the distribution is much less spread out, which is logical since the voxel values in the background are much smaller than in the signal.

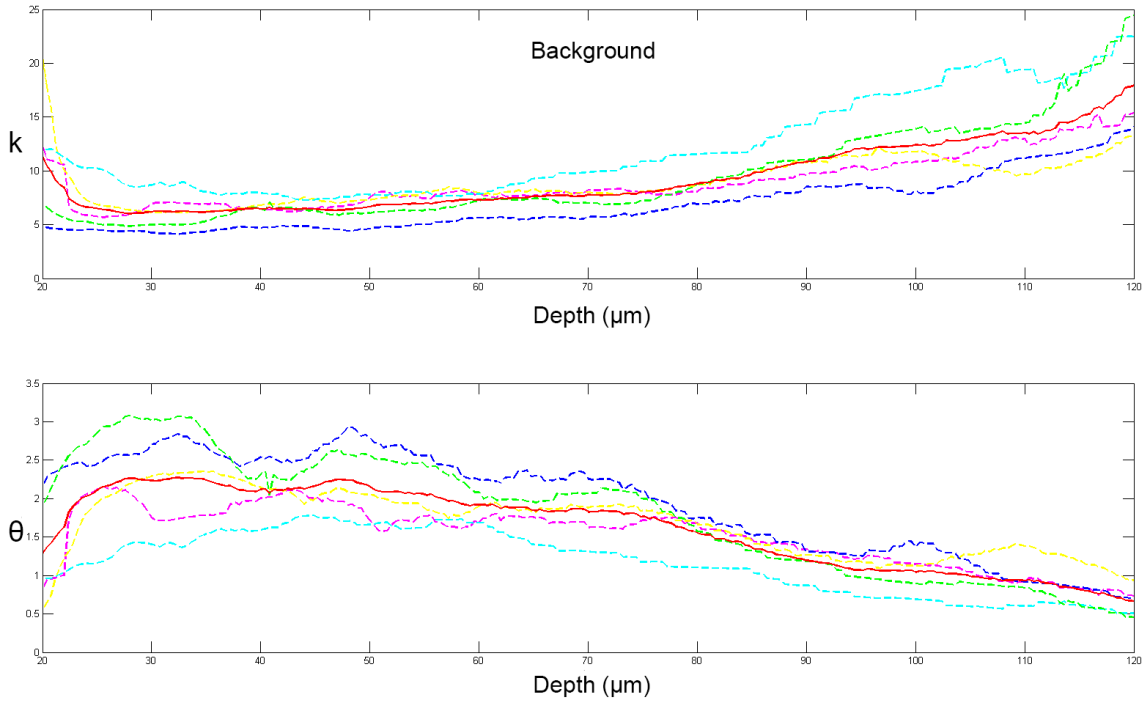

Figure 4.17. Evolution of the parameters k (top panel) and θ (bottom panel) of the gamma law of the microscope noise within the background portion of the front substacks of five different brain samples and there average (red) after removing the first 20 µm.

Finally, we computed the noise in the signal and background portions of the back substacks of the same set of samples (Fig. 4.18) after discarding the first 50 sections from evaluation because of the saturated signals of many cell bodies like in the front stack.

The graphs again show similar profiles in that k increases while θ decreases with depth for both signals and backgrounds. As in the front substacks, k is much smaller in the signal whereas θ is significantly smaller in the background.

This fitting was performed using a matlab script that computes k and θ in each section of each raw dataset in the four described situations.

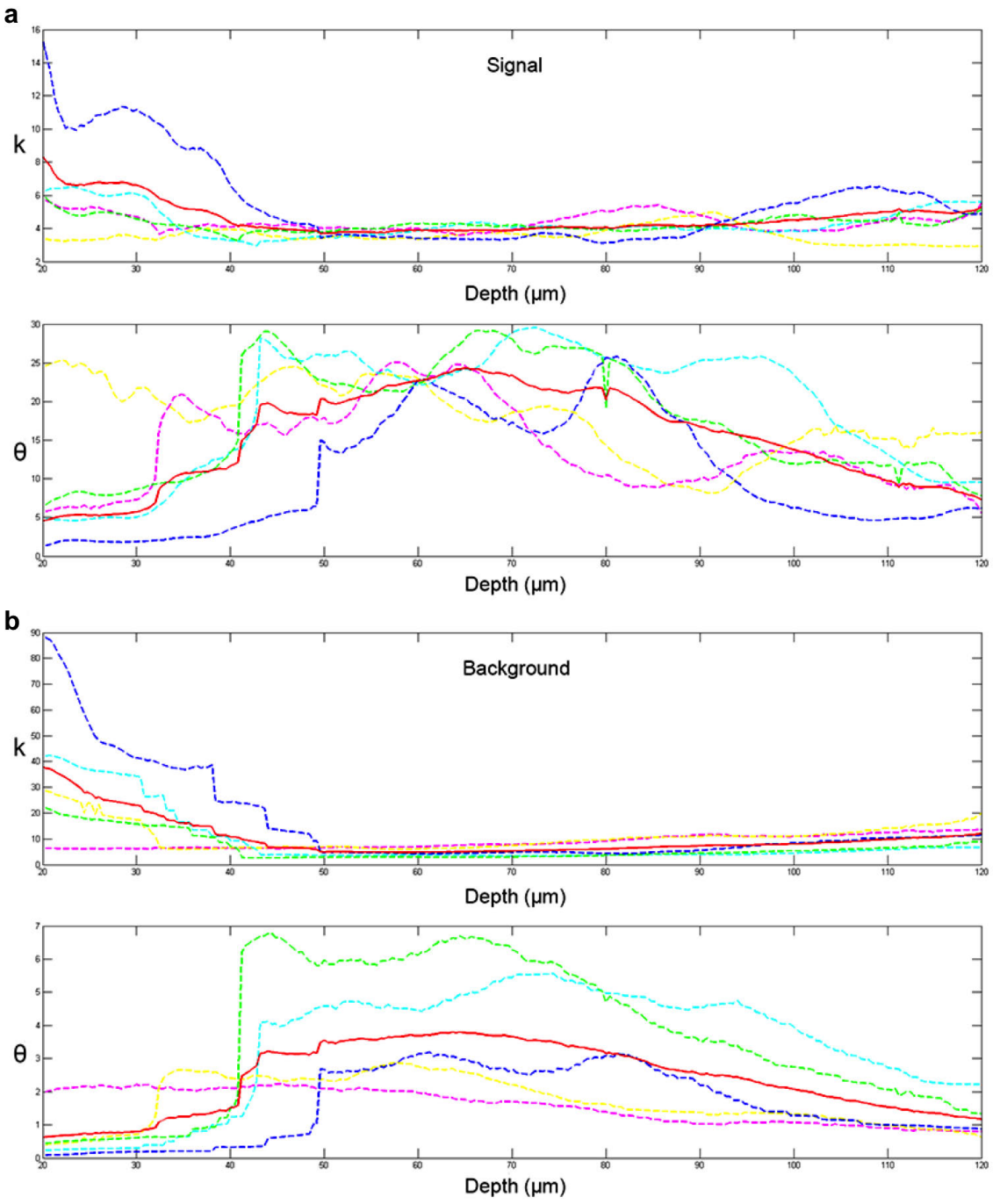

Figure 4.18. Evolution of the parameters k (top panel) and θ (bottom panel) of the gamma law of the microscope noise within the signal, (a) and background, (b) of the back substack for 5 different brain sample after removing removing 20 µm (cell bodies).

c. IN SILICO DATA GENERATION

Using above information we generated the simulation of a laser-scanning microscopy virtual 3D image stack (Fig. 4.12). We took a down-sampled stack of 800 x 800 voxels and 300 sections of the real brain sample (resolution 0.4 x 0.4 x 0.4 µm, 120 µm thickness), segmented the neuronal fiber signal, and cut the stack into two substacks with the thickness of 175-250 sections from front and back, which yield overlap of 50-200 voxels between substacks, respectively.

The average (red line) of the fitting curves (dashed curves) of five different pairs of 3D stacks was chosen as the values of k and θ parameters through depth for four situations: signal of the front substack (Fig. 4.15, red line), background of the front substack (Fig. 4.17, red line), and signal and background of the back substack (Fig. 4.18, red lines). Using those values estimated through the depth, empirical gamma noise filter of our microscope can be estimated using a noise generator such as gamrnd (k, θ) of Matlab that randomly generates numbers from the gamma distribution defined by the two parameters of the law k and θ. Four different filter stacks representing the noise of our laser scanning microscope, the front stack signal, the front stack background, the back stack signal and the back stack background are then generated by drawing random numbers using the gamma "noise" generator using corresponding parameters for each slice of the stack.

We then take a real laser scanning images of neuronal fibers (front stack, Fig. 4.12.b) and made structure of the signals without noises by thresholding (Li algorithm) and smoothing them (Fig. 4.12.c). From this stack, we took 800 x 800 x 300 voxels stack (resolution 0.4µmx0.4µmx0.4µm), and cut it into two overlapping substacks (so called front and back substacks), each with the size of 800 x 800 x 250 (one with the first 250 and the other with the last 250 sections, with 200 sections of overlap, Fig. 4.12.f). The back stack was rotated with given angles. We then filtered the different object (signal and background) in the front and back stack using four types of simulated noises described above. Addition of simulated noise provides relatively clear image if the section is recorded at shallow depth (Fig. 4.12.d) and more blurred image if it is recorded at deep layers (Fig. 4.12.e), which fit well with the real images of brain samples.

Addition of depth-dependent noise simulates the situation when the same part of the brain is imaged from different sides of the sample. Here we simulate a brain sample with the thickness of 120 µm (Fig. 4.12.f, top). After applying increasing levels of depth-dependent noise to the substack data (Fig. 4.12.f, bottom), the section of the brain that is 30 µm away from the front surface of the sample appears relatively clear in the front substack (Fig. 4.12.d), but more blurred in the back substack because it is 90 µm away from the back surface (Fig. 4.12.e). These fit well with the real images of brain samples. By rotating and translating the virtual sample data and applying noise simulation thereafter, we can create tilted substacks with known parameters to examine whether the registration software could yield successful compensation.

The resulting pair of image datasets reproducing realistic confocal three-dimensional images of fibers was submitted to our registration algorithm.

d. VALIDATION OF STITCHING ACCURACY

Using this simulated image stack, we assessed the quality of our registration (Fig. 4.19&20). We rotated the back substack at 1° around x-, 2° around y-, and 5° around z-axes, and submitted the front and rotated back substacks to the 2D-SIFT-in-3D-Space Volume Stitching plugin for registration. We can qualitatively see the performance of the plugin in Fig. 4.19. The front substack in green is superposed to the back substack in magenta. The superposed image should appear white where the two substacks are registered successfully. The two images do not match just after the first overlap detection step (Fig. 4.19.a, which corresponds to the step described in Fig. 4.5.a). Subsequent registration in the x-y plane (Fig. 4.5.b) and then x-z plane (Fig. 4.5.c) and y-z plane (Fig. 4.5.d) gradually improves matching (Fig. 4.19.b-d), and the overlapping images appear almost completely white with only a slight green or magenta blurred halo, attesting a good quality of registration. This halo, which is resulted from the different levels of signal noises of the front and back substacks calculated by the laser-scanning image simulator, affects neither the shape nor the diameter of the neurons drastically and can therefore be neglected.

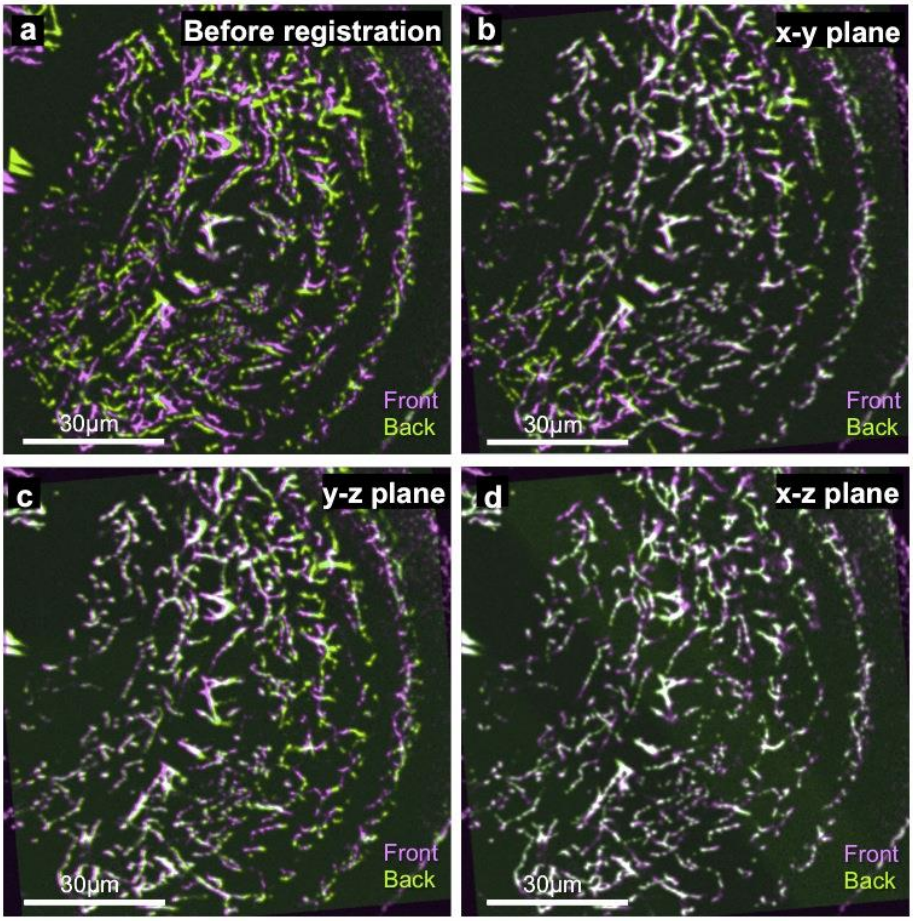

Figure 4.19. Superposition of the front and back stack at each step of the registration, (a) Before registration, (b) After registration around z, (c) After registration around x, (d) After registration around y.

Because the introduced rotation angles are known, we can do a quantitative analysis of the registration quality by comparing those values with the one given by the transformation matrix computed by our plugin. The final rotation matrix computed for this dataset is shown in Table 4.1.a. When we convert this matrix into Euler angles θx, θy and θz (rotation around x-, y- and z-axes), we obtain the rotation angles of Rx = -1.2757°, Ry = -2.0232°, Rz = -5.0010°, which are similar to, but not completely identical with, the opposite of the angles introduced artificially in our simulated data (1°, 2° and 5° around x-, y- and z-axes, respectively). Registration was very precise for z (registration error 0.019%) and y (1.160%) but worse for x (27.566%). This lower

precision around x can be explained by two factors. First of all, the tilting around x (1°) is small than the other angles (2° and 5°) which makes it harder to correct. The second factor is the order of the iterative registration: the procedure is done in such a way that it starts with the rotation correction around z, then x, y and finally z again. Because the rotation around x is calculated early in the procedure, it is likely to be disturbed by the following registration around y and z.

Registration can be improved by a second loop through the registration process. Indeed, after two iterations of registration, the rotation error around x is greatly improved (Annexes, Table 4.1.b). Higher number of iterations further decreases the rotation as well as translation errors, which are lower than 1% of the original rotation angles and less than 1.3 voxels (0.26 µm) of translation. In practice, 2 iterations seem to be a good compromise between accuracy and computation time, because further registrations do not greatly improve the errors. Note that the rotation error around each axis does not decrease steadily after more iteration. Trying to improve the registration around one angle may slightly shift the registration of the other ones.

Registration performance can also be examined using the overlap correspondence curve, which shows the number of matching features between the last section of the front substack and each section of the other substack (Annexes, Fig. 4.20.a). After the first overlap detection step before registration, the corresponding curve appears very broad with a small number of matching features (blue line in Fig. 4.20.a). Indeed, the front and back substacks are not registered yet and thus the similarity between them is still rather low. On the contrary, the correspondence curve after the first round of registration is much thinner and sharper, and the number of features is three times larger, traducing a higher similarity between the front and back substacks and thus the efficiency of the 2D-SIFT-in-3D-Space registration. The correspondence curves after the second iteration onwards essentially overlap, without showing further improvement. Visual examination of the overlap between front and back substacks also shows slight residual overlap error after the first iteration (Fig. 4.20.b) but no error after the second and further iteration (Fig. 4.20.c&d). These are consistent with the evolution of Euler angles shown in Table 4.1.b. In practice, we will refer to those curves to validate the proposed transformation model.

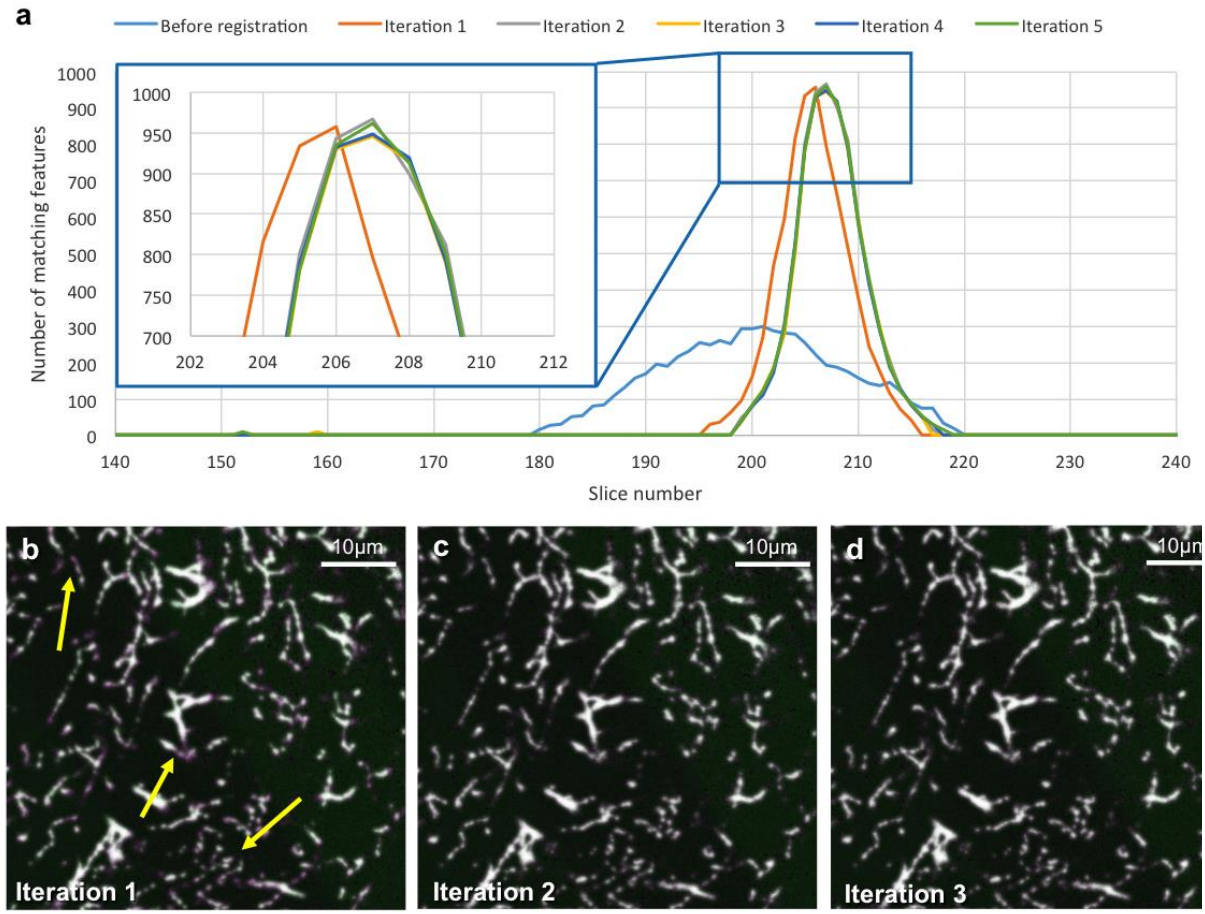

Figure 4.20. Registration of artificial data, (a) Visual result of the registration step by step of an algorithm iteration, (b) Overlap detection graph for five iterations, (c) Superposition of the front (green) and registered back (magenta) stacks of neural fibers data for three iterations.

In theory, iterative use of 2D SIFT might increase the chance that the whole registration fails. It is not the case in our code, because we initiate the iterative process in the direction of the most likely important transformation (rotation around z-axis), which greatly removes the registration error as shown in Figs. 4.19 and 4.20.

Table 4.1.b (Annexes) shows that rotation error after multiple iterations becomes very small around z-axis, but remain a bit larger around x- and y-axes. The better registration accuracy around z-axis compared to x and y can be explained by the size and the quality of the image slices

perpendicular to z. Indeed, the x-y slices are much larger (800 x 800 pixels) than the x-z and y-z slices (800 x 200 pixels) of the overlapping part, leading to a greater number of matching features. In addition, comparisons of x-y slices do not suffer from the lower resolution and deformation along the z-axis that can be seen in laser-scanning microscopy.

Thus, registration result is likely to be affected by the size of the overlap. When we reduced the overlap size by taking fewer sections from the front and back substacks, registration error increased (Annexes, Table 4.1.c). If the overlap size was too small (e.g., 50 voxels), the algorithm struggled to find rotation around x and y with the default parameters. However, modification of those parameters (here reducing the minimum image size from default value 64 to 1) fixed the problem (Annexes, Table. 4.1.c, bottom).

These results show that multiple iteration and adequate size of overlap are both important for precise registration. They result from a compromise between faster computation time and better registration quality. Other factors, such as SIFT parameters and the thickness of the partial-MIP slice, should also affect precision of registration. The simulated laser scanning fluorescent microscopy dataset with known rotation parameters is a valuable tool for exploring the best combination of registration parameters.

When the relative rotations are small between the front and back stack, it might be difficult to accurately compute a model. We repeated the same procedure with different introduced angles: Rx = 1°, Ry = 1° and Rz = 5° to check whether our algorithm is also able to fix very such shifts. The results for 5 iterations are reported in Table 4.2 (Annexes).

Similarly, we can see a significant improvement of the registration quality at the end of the second iteration but very few differences from the third one. Before registration (Fig. 4.21, blue curve), because the tilting angles are smaller than previously the curve is rather sharp but the number of matching features is very low. Moreover, the error on the corrected angles are inferior

to 1% for x and y but high for the x-axis rotation (23%). At the end of the second iteration all errors fall under 1% proving a good registration quality.

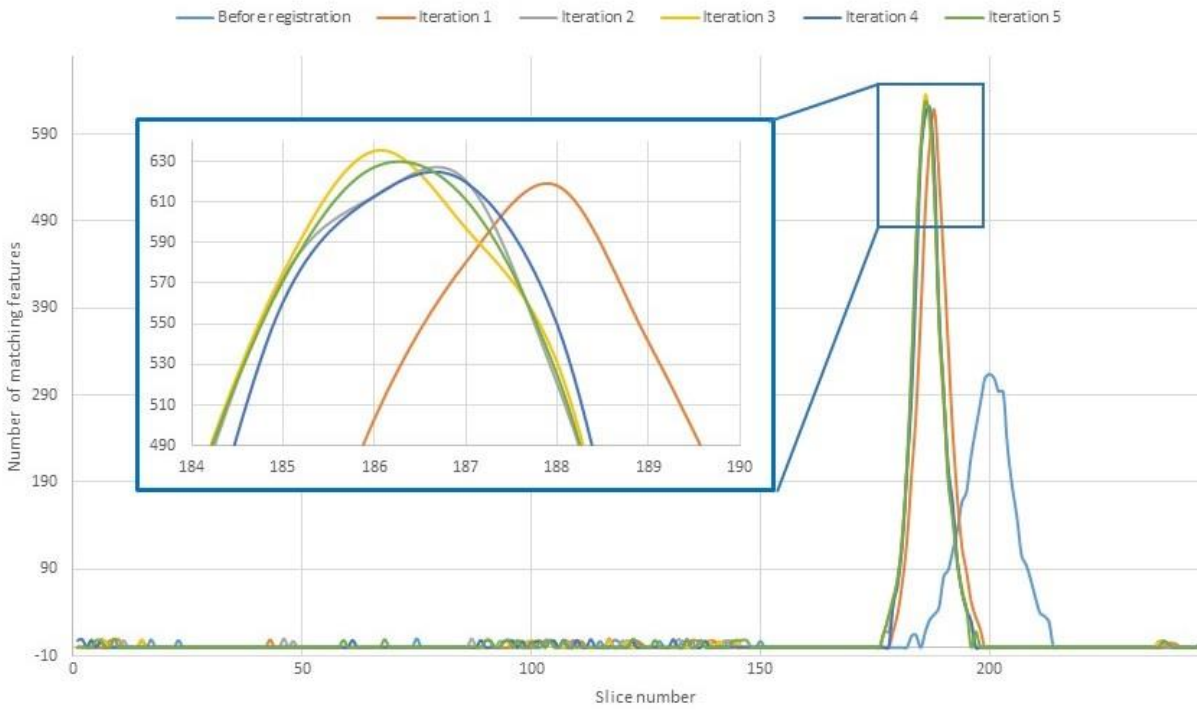

Figure 4.21. Overlap detection for 5 iterations of the simulated data for Rx = 1° Ry = 1° Rz = 5°

We then compared the accuracy and efficiency of the block-by-block comparison with the slice-by-slice comparison. This algorithm should be able to register substacks with large tilting angles. To determine the tilting limit of the method, we fixed the rotation and tilting angles of Rz = 5°, Ry = 2° and gradually increased the value of Rx by 5° steps and submitted the data to slice-by-slice (Annexes, Table 4.2.a) and block-by-block comparisons (Annexes, Table 4.2.b). The partial MIP size was set to 20 slices for both version and, for the latter case, the splitting parameter was set at 5.

Both algorithms performed similarly well for small tilting angles (≤15°). Stitching with block-by-block comparison was about two times faster than with slice-by-slice comparison. The difficulty of overlap detection increases with tiling because the similarity of sections perpendicular to z-

axis decreases. Overlap detection with slice-by-slice comparison becomes difficult as Rx becomes as large as 20°, where the correspondence curve does not present the typical bell-shape but is extremely noisy with very few matching features (Fig. 4.22.a). With our virtual test data the initial overlap was identified as 131-section thick (the peak of the correspondence curve), and thanks to the re-sliced partial MIP comparison around three axes, registration was improved drastically after a few iterations (orange curve in Fig. 4.22.b) than before registration (blue curve in Fig. 4.22.b). However, the computed rotation model was still not as accurate as expected, with higher rotation error rate around x- and y-axes (6.35% and 19.1% respectively, Annexes, Table 4.2.a, bottom).

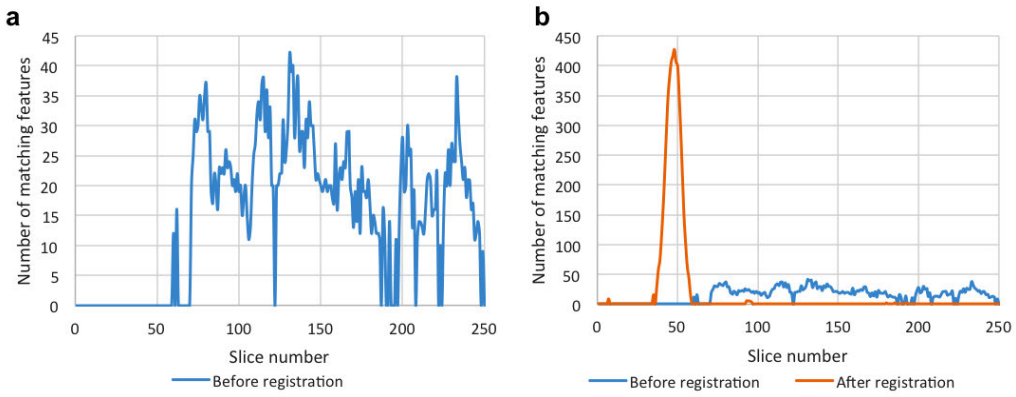

Figure 4.22. Registration of artificial data with big tilting (Rx = 20°, Ry = 2°, Rz = 5°) with the slice-by-slice overlap detection algorithm. (a) Overlap correspondence curve before registration. Highest peak was at the 131st section. (b) Comparison of the curves before and after registration. Actual matching peak after registration was at the 49th section.

The same data with 20% rotation were also tested with block-by-block comparison. In this case initial overlap was identified as 77-section thick. Due to the smaller size of the detected overlap, however, the matching features were concentrated only in a small portion of the data (Fig. 4.23.a, green circle). This caused erroneous computed rotation angle, with an error rate as high as 741% and 79. 9% around x- and y-axes (Annexes, Table 4.2.b, 4th row). We then decreased the split value to two, but the detected overlap was again as low as 76 sections (Fig. 4.23.b, green circle), causing similar problem as before to result in high error (Annexes, Table 4.2.b, 5th row).

In our algorithm we usually detect the overlapping volume of the substacks at the beginning and perform subsequent registration only using this portion of the data. With high tilting angle between substacks, only a small part of the overlapping volume might erroneously be detected, as experienced above. With block-by-block comparison we can effectively skip overlap detection when we set the split parameter to one (i.e., no splitting), so that the program uses the data of the entire substacks to compute registration (Fig. 4.23.c, green circle). This resulted in the much improved rotation error as low as 0.32% (Annexes, Table 4.2.b, bottom).

In conclusion, both slice-by-slice and block-by-block comparison were very efficient for small tilting (≤15°), and computation by block-by-block comparison was generally faster because of fewer number of comparisons performed. For larger tilting, block-by-block comparison without splitting was effective.

We then analyzed the effect of different splitting parameters for block-by-block comparison (Annexes, Table 4.3). For a moderate tilting angle of Rz = 5°, Ry = 2° and Rx = 5°, we performed registration from split value = 1 (no split) to the number of the sections in the substack, which is essentially the same as slice-by-slice comparison. After 5 iterations, registration accuracy was essentially the same for all splitting parameters. Computation time was long when the split value = 1, because the entire substack data are subjected to subsequent registration. Because the overlap does not cover all slices, many SIFT features will not match and their consideration does not bring any improvement to the registration result. Because of this, a splitting parameter of 1 (i.e., no split) must be used only in case of high tilting between the two stacks as discussed earlier.

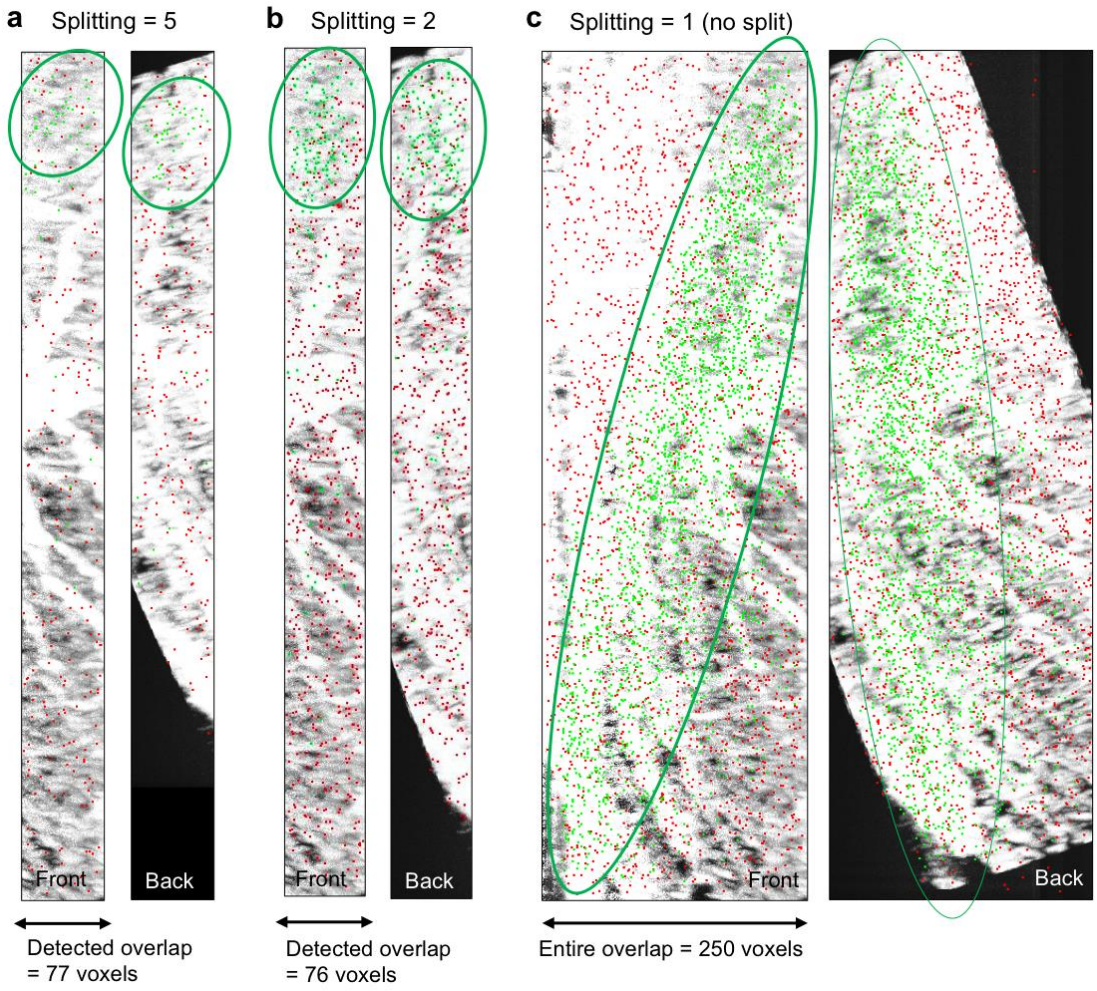

Figure 4.23. Repartition of matching features (green) of artificial data with big tilting (Rx = 20°, Ry = 2°, Rz = 5°) using the block-by-block overlap detection algorithm with the splitting parameter of 5 (a), 2 (b), and no splitting (c). Detected overlap was 77 and 76 pixels for (a) and (b).

When splitting was activated (split>1), computation time depended on the total number of SIFT comparison for overlap detection (#comparison in Table 4.3). Our test data has the thickness of 250 sections. For a splitting parameter of 5, the program first splits the entire substacks into 5 blocks of 50 sections and then does 5 SIFT comparisons to find the best match. The selected block is split again into 5 blocks of 10 sections and compared with a block of the same size from the front substack (5 comparisons). The best-matching block is further split into 5 blocks of 2 sections and once again compared five times. Because the selected block contains only 2 sections, it

cannot be further split into 5 parts, so a slice-by-slice comparison is used to determine the exact position of overlap (two comparisons). Thus, we need in total 17 comparisons to detect the overlap size. The number of the required comparisons is much smaller than that of the slice-by-slice comparison (250). However, the computation time was only about two times faster (40 min versus 71 min, Table 4.3). This is likely because SIFT comparison of thick partial MIP images takes longer time than the comparison of single section images with much fewer signals.

	Euler angles:			Rotation error:		
	Rx	Ry	Rz	ΔRx%	ΔRy%	ΔRz%
After single iteration	-0.7678°	-0.9922°	-4.9905°	23.22%	0.78%	0.19%
After 2 iterations	-0.9923°	-1.0009°	-4.9972°	0.77%	0.09%	0.056%
After 3 iterations	-1.0029°	-1.0009°	-4.9947°	0.29%	0.09%	0.106%
After 4 iterations	-1.0014°	-0.9992°	-4.9985°	0.14%	0.08%	0.003%
After 5 iterations	-1.0013°	-1.0023°	-5.9943°	0.13%	0.23%	0.114%

Table 4.4. Rotation parameters after registration of the simulated data for Rx = 1° Ry = 1° Rz = 5°

The number of comparison increases as we set higher split parameter, which results in longer computation time (Table 4.4). Thus, for practical purposes split parameter between 2 and 5 should be most useful. However, if the sections contain very dense signals, setting two few splits results in the blocks with too many signals that may cause saturation or too many unmatching features. The running time then increases a lot but not the quality of registration. Because the choice of the splitting parameter is let at the user appreciation and is not always obvious, the Table 4.5 can be used as a guide for an accurate selection.

Split parameter	Feature and suggested situation
1	No split. Slow computation, this value should be used only in case of big tilting.
2	Fastest splitting, but may cause misestimating of the overlap position in some cases.
5	Slower than splitting parameter 2 but better estimation of the overlap position. Recommended value for most purposes.
Number of sections in the substack	Effectively the same as slice-by-slice overlap detection. Slow. This must be used with a small number of iterations in case of small tilting for a very precise overlap detection

Table 4.5 Clues to select the splitting parameter of the block-by-block comparison overlap detection algorithm

Our comparison showed that block-by-block comparison is in most cases faster than and as accurate as slice-by-slice comparison. However, it is worth noting that overlap detection of the former algorithm might cause misidentification in a few certain cases. If the correct position of the overlap happens to fall just a few sections after a splitting position between blocks (Fig. 4.24), the algorithm might select the neighboring block as the best match because it may contain more sections that are similar to the best-matching section. Such mismatch in the overlap detection step is likely to be corrected during the subsequent registration steps, but if stitching does not work well, it is worth trying to use different split parameters in order to move the splitting position between blocks.

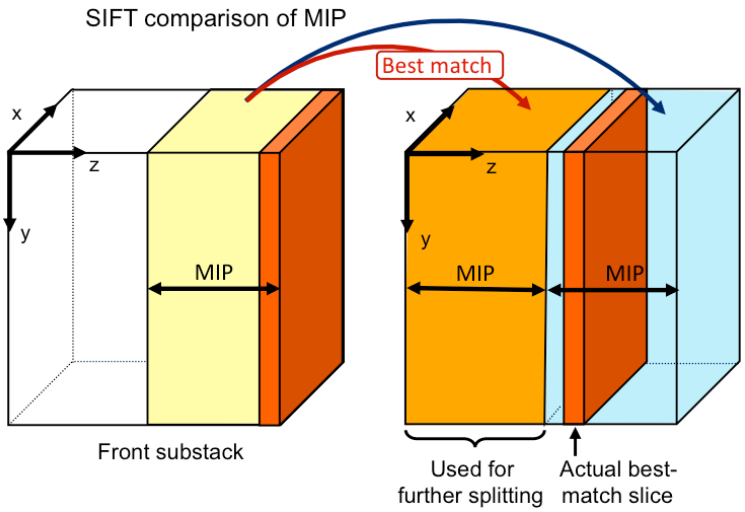

Figure 4.24. Possible miscomputation of overlap position with block-by-block overlap detection algorithm. Suppose that the true overlap position is located a few slices after the splitting position of the blocks. The orange block of the front substack has then more in common with the light purple block of the back stack. This block will then be used for further splitting instead of the blue substack, in which the true overlap position is actually located.

3. APPLICATION

a. EXPERIMENT DESCRIPTION

Using the previously described program, we took high resolution images of Drosophila melanogaster brain to study two specific types of neurons, the octopaminergic and dopaminergic neurons through two experiments.

In the first experiment, also referred as age-analysis, we investigated the evolution of the octopaminergic and dopaminergic neurons by qualitatively and quantitatively comparing their arborization and connectivity pattern within the brain between young flies (5 day-old) and adult flies (30 day-old). To this purpose we specifically label those particular neuron types as well as their pre-synaptic sites using fluorescent proteins.

In the second experiment, or activity-analysis we examined the effect of activity-dependent structural plasticity in the neural networks of monoamine cells. For this, we inactivated either octopaminergic or dopaminergic neurons by manipulation of their ion channels, determinant in neuron firing ability.

b. QUALITATIVE AND QUANTITATIVE ANALYSIS

i. Behavior

Flies whose octopaminergic or dopaminergic neurons were switched off (experiment 2) have an abnormal behavior: their walking, jumping and flying reactions appear to be very different than the wild type. Flies were stored in transparent tubes of which they climb the wall, taking the whole space available. If those tubes are stroke on a table, flies fall at the bottom of the tube under the impact but, wild type flies immediately move to the top by climbing the wall, jumping or flying.

5 day old (young) octopaminergic deficient flies show in majority this normal behavior: after falling because of the shock of the tube on the table (Fig. 4.25.b), similarly to the control (wild type), most of them quickly go back to the upper part of the tube (Fig. 4.25.c-f). A small number of them seems however to have difficulties to move and do not follow the global tendency of going back to the top of the tube. This abnormal behavior is even clearer for 30 day old Drosophila after inactivation of the octopaminergic neurons. Indeed, unlike the control they do not climb the wall immediately after Impact. Moreover, they tend to walk slower and do not jump as often (Fig. 4.26).

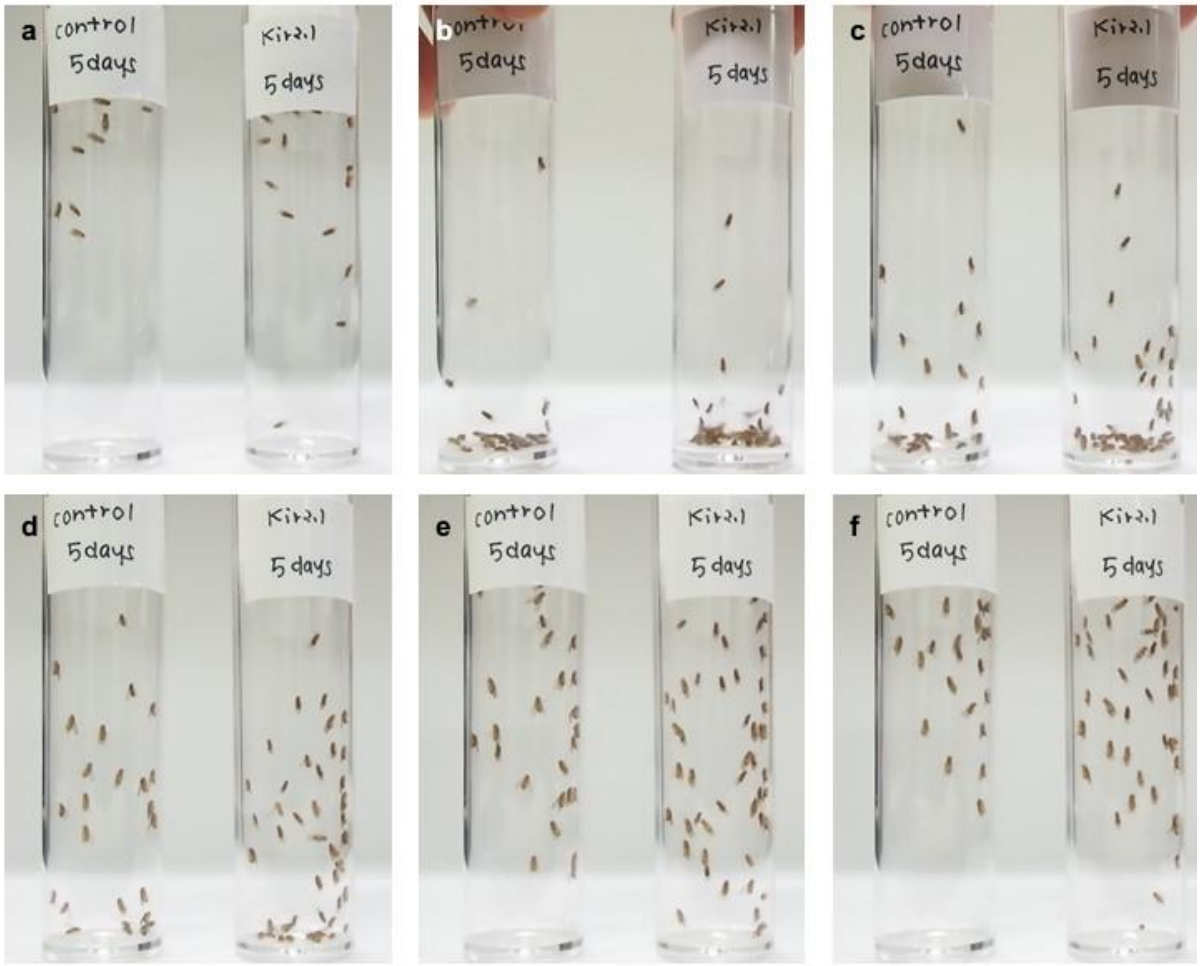

Figure 4.25. Behavior of 5 day old Drosophila melanogaster (octopaminergic neuron deficient flies versus control) after the impact of the tube on the table, (a) Before impact, (b) Impact, (c) Impact + 1s, (d) Impact + 2s, (e) Impact + 3s, (f) Impact + 4s.

Even when the mutant flies are resting, they present atypical leg movements. Indeed, whereas control flies stay static when resting, the mutant ones seem to have uncontrolled shaking movements.

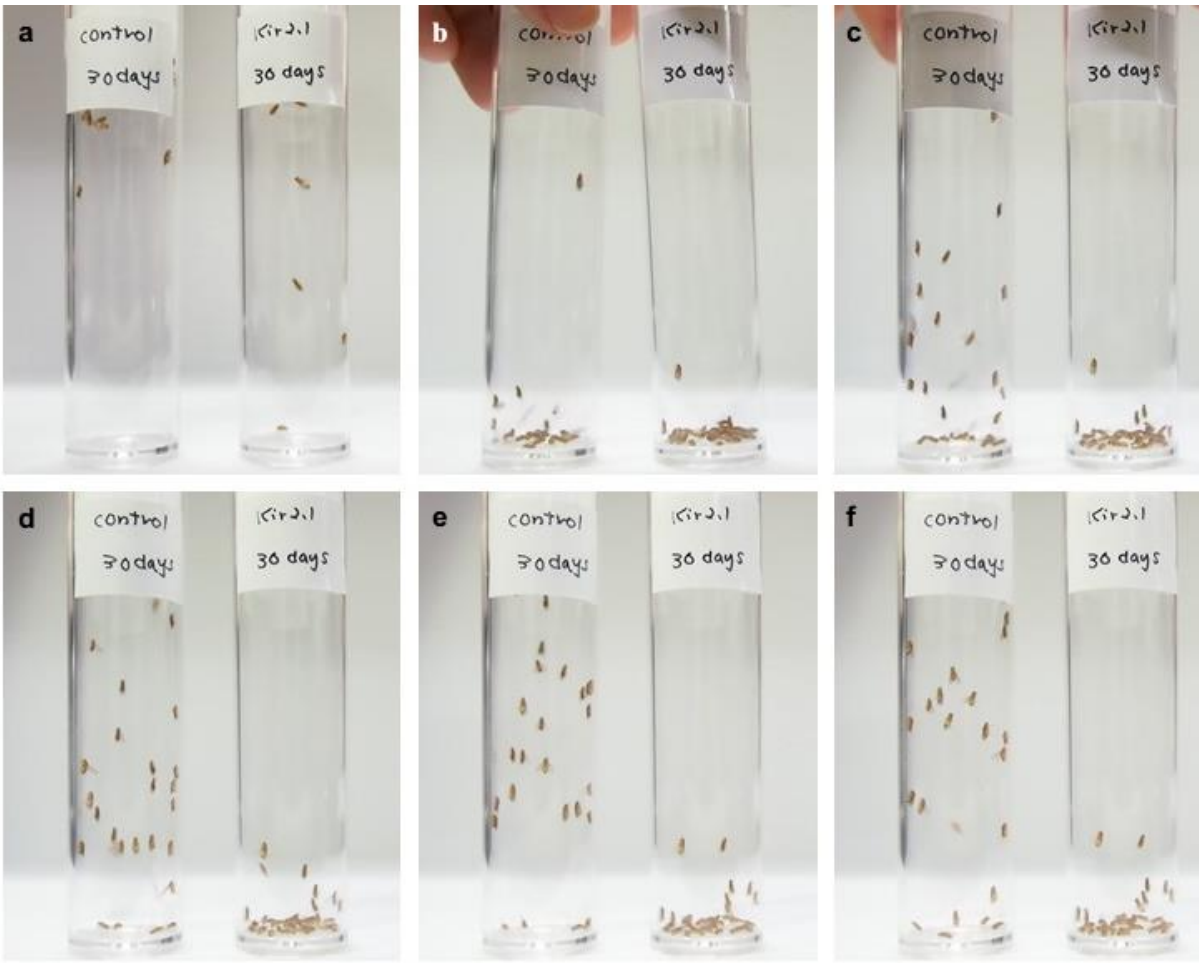

Figure 4.26. Behavior of 30 day old Drosophila melanogaster (octopaminergic neuron deficient flies versus control) after the impact of the tube on the table, (a) Before impact, (b) Impact, (c) Impact + 1s, (d) Impact + 2s, (e) Impact + 3s, (f) Impact + 4s.

ii. IMAGE COMPARISON

Experiment 1, genotype 1:

In this experiment, we want to study the evolution of both dopamine and dopaminergic neurons as well as the interactions over time. To this purpose we made samples for which dopaminergic neurons, octopaminergic neurons and octopaminergic neurons pre-synaptic sites are visible by a fluorescent confocal microcope. The pre-synaptic sites define the point of communication where

octopaminergic neurons are transmitting information with other neurons. We imaged this combination for 5 day old (also called young) and 30 day old (old) flies.

We first examined the evolution of dopaminergic fibers in young (Annexes, Fig. 4.27.a) and old (Annexes, Fig. 4.27.b) flies by image comparison. For both modalities, we can notice an important number of cell bodies located especially in the optical lobe. Despite the difficult comparison due to the partial occlusion of the cell bodies, we can notice that, 30 day old samples look relatively similar to young specimen. The fibers spread in the entire and do not present signs of aging. A superficial visual comparison does not allow us to find any obvious differences between young and old dopaminergic neurons and a precise mathematical characterization and comparison would be helpful to track an evolution within time.

Octopaminergic neurons also arborize in the entire brain for both young and old samples (Annexes, Fig. 4.28) at a relatively similar density. However, even if this is not obvious, we can point out a slight difference: young flies tend to have thicker and slightly more extensive branches. For confirmation, it would be useful to compute the length and diameters of those fibers.

Except the difference of intensity (not normalized data), the repartition and density of octopaminergic pre-synaptic sites seem to be stable over time for Drosophila melanogaster. 5 day old flies' pictures look very similar to 30 day old (Annexes, Fig. 4.29). To check this, we can compute the number of pre-synaptic site in the whole brain or in location of interest. This will also inform us of the uniformity of the synapse repartition (isotropy) within the brain.

By comparing 5 day old and 30 day old sample for dopaminergic, octopaminergic neurons and octopaminergic neuron pre-synaptic sites we notice an apparent stability over time of these neurons (few sign of aging). However, to precisely characterize the evolution of their morphology, repartition and track a potential reorganization a simple qualitative analysis is far from enough and a statistical must be performed to highlight any change.

Experiment 1, genotype 2:

This experience, very similar to the previous one, investigate the aging effect on the octopaminergic and dopaminergic neurons of the fruit fly, but the combination of genes of the Drosophila strain is switched such way that the third channel shows the pre-synaptic site of dopaminergic neurons instead of octopaminergic.

We can confirm the results of the previous experiment by comparing the images of 5 day old and 30 day old flies (Annexes, Fig. 4.30): octopaminergic neurons do not seem to be affected over time. Indeed, the picture of their fibers for 30 day old samples appears to be very similar to 5 day old ones.

This experience gives us also a better overview of dopaminergic neurons (Annexes, Fig. 4.31). Because the cell bodies are not labelled, we can see more accurately the repartition of fibers within the brain especially in the optical lobe. Despite the difference of brightness between samples, the branches density for young flies seems to be higher than the one of older fruit flies. Moreover, fibers appear more broken up in 30 day old specimen suggesting neuron degeneration. However, those conclusions must be taken with caution because the dopaminergic pre-synaptic sites, where the dopaminergic neurons transmit information to other neurons seem very similar between young and old flies suggesting a normal and stable activity over time (Annexes, Fig. 4.32).

Experiment 2, genotype 1:

In this experiment, we did not compare only the effect of the octopaminergic neurons inactivation but also the effect of time on those neurons and the brain plasticity. Pictures were taken for both Kir2.1 (inactivated) neurons and control neurons at 5 (Annexes, Fig. 4.33) and 30 days (Annexes, Fig. 4.35).

First of all, it is important to notice that the other neurons that all the other neurons of Drosophila central nervous system did not seem affected by Kir2.1 neurons. Indeed, the nc82 labelling appear to be normal and the brains do not look smaller compared to the control. However, because of the abnormal behavior observed and described in the previous section, we can affirm that the brain was affected by the octopaminergic neurons inactivation.

Kir2.1 inactivated octopaminergic neurons of 5 day-old flies seem normal compared to the control (Annexes, Fig. 4.33): they arborize in the entire brain in a pattern in appearance similar to normal flies and there are no gaps in the fibers. Similarly, big differences cannot be noted between the control and Kir2.1 flies in the number of repartition of the pre-synaptic sites (Annexes, Fig. 4.34).

Concerning 30 day-old specimen, we can notice a wide variability between individuals. Indeed, if fibers seem normal (Annexes, Fig. 4.35), the pre-synaptic site channel appear very different according to the sample. If for some flies, it hardly can be distinguished from control flies, in some other cases, no pre-synaptic sites can be detected even at high laser power (Annexes, Fig. 4.36).

Experiment 2, genotype 2:

Similarly, the effects of inactivation of dopaminergic neurons on the brain plasticity were studied over time. Flies lacking dopaminergic neurons do not survive for a very long time after birth. Because of this, we did not perform a comparison between young (5 days) and older (30 days) flies like in the previous experiment, but between newborns (0 day, just after heat shock) and young (5 days).

Despite this low survival rate, the brains of newborns seems normal at the first glance. Their sizes, given by the nc82 labelling (background), remain in a usual range of depth. However, even if the fibers also look relatively extensive, spreading in the entire brain, we can already notice a degradation of the fibers quickly after heat shock (0 day samples) compared to the control

(Annexes, Fig. 4.37). First, the fluorescent signal is extremely low. To be able to take those pictures, we had to use laser power more than 4 times higher than for the control. Moreover, many fibers, even the thick ones, already start to appear broken up and we can notice many gap in the signal. In the bottom part of the brain many thin fibers already disappeared, as well as in the OL. The number of pre-synaptic sites also dropped dramatically immediately after heat shock (Annexes, Fig. 4.38). Some of the newborns do not even show any pre-synaptic sites. Thus, the neuron degeneration seems to be initiated as soon as they are switched off. However, it seems that this is a big variation among samples. Indeed, some of the samples do not have any pre-synaptic site whereas others look almost normal.

After 5 days, only the thicker branches remain (Annexes, Fig. 4.39). The thinner ones, especially in the optical lobe completely degenerate and cannot be detected even at very high laser power. If some pre-synaptic sites remained visible in 0 day samples, at 5 days they almost all disappeared (Annexes, Fig. 4.40).

It is interesting to notice that switching off neurons does not have the same effect on their pattern according to the neuron type. Indeed, if dopaminergic neurons degenerate extremely rapidly, almost all fibers disappear, only big central branches remaining after 5 days, octopaminergic neurons do not seem to be disintegrate even after 30 days. Moreover, dopaminergic neurons deficient samples do not contain dopamine pre-synaptic sites either, whereas octopamine pre-synaptic sites channel appears normal.

Because of this quick degeneration and the depth of the insect, we can show the dopaminergic neurons are critical for Drosophila melanogaster and emit the hypothesis that their functions cannot be ensured by any other type of neurons.

iii. Statistical analysis

To quantitatively compare fiber architecture, we trace neural fibers and their branches using the algorithm developed by Henrik Skibbe (Kyoto Univ.) and identify the pre-synaptic sites using EVE (Extended Volume Embedding) algorithm. Using those data we can compute various morphological parameters such as position and number of branching, distance between two consecutive branches, and position and number of pre-synaptic sites.

In this document, we will detail the procedure of the pre-synaptic sites analysis and give preliminary answers to the question of connectivity evolution in the Drosophila melanogaster brain.

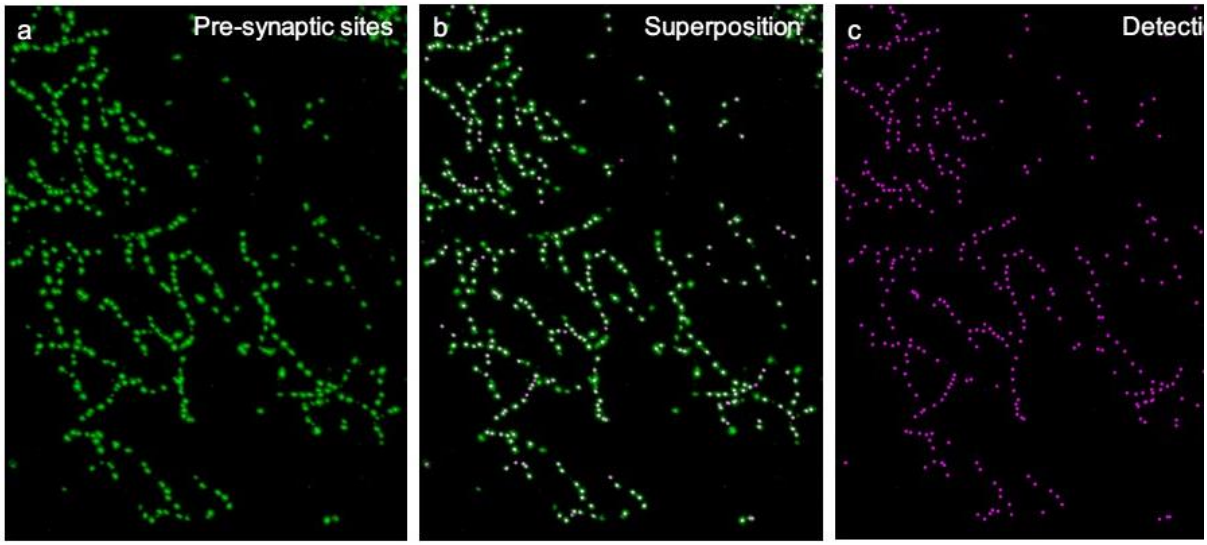

Figure 4.41. Pre-synaptic sites detection using EVE algorithm, (a) Raw data, (b) Superposition of the raw data (green) and the detected synapses (magenta), (c) Detected synapses using EVE.

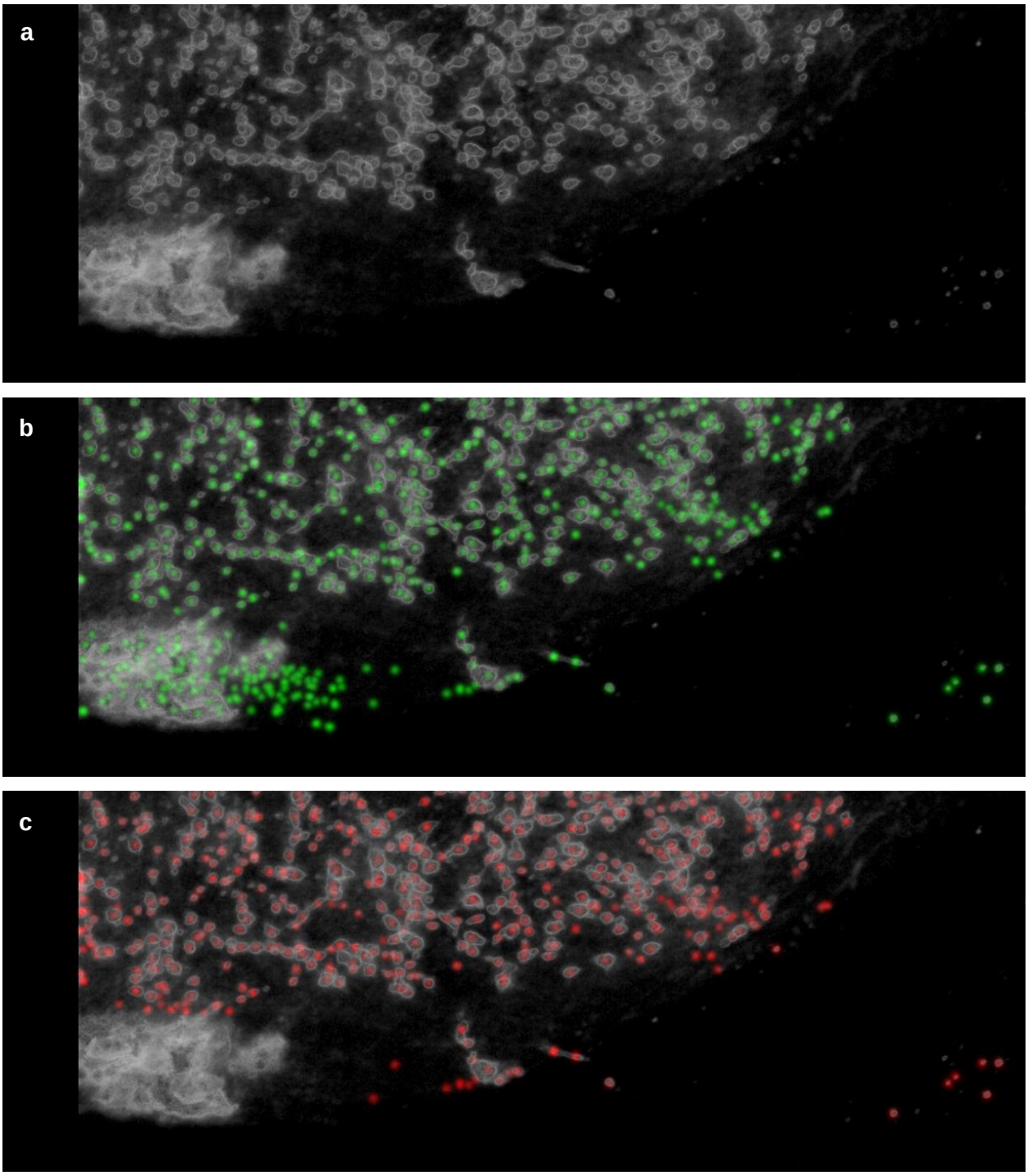

Figure 4.42. Effect of cell bodies presence on EVE pre-synaptic sites detection, (a) Raw data, (b) Superposition of raw data and EVE synaptic sites detection, (c) Superposition of raw data and EVE synapse detection on data whose cell bodies have been erased.

To count the number of pre-synaptic sites within the brain, we use EVE, which looks for blobs of a pre-given radius (r = 2) as shown in Fig. 4.41. To ensure the detection quality, before submitting the data to the software, they are first cleaned using the 3D rendering software Fluorender to erase labelled cell bodies which tend to give false positive synapses detection.

Indeed, as one can notice in Fig. 4.42.a, the data can present bundles of cell bodies in different parts of the brain. However, due to this strong non-uniform signal, EVE incorrectly detects pre-synaptic sites within this volume (Fig. 4.42.b). To limit this number of false positive, because no method exists to correct a posteriori, it is important to preprocess the data in order to erase the cell bodies and avoid the detection (Fig. 4.42.c). Since no automatic procedure has been established to accurately detect and suppress the cell bodies, we manually processed all the data using the brush tool of Fluorender despite the time required for such work.

Using EVE on the preprocessed data, the number and position of pre-synaptic sites is computed for all the genotypes described before.

Experiment 1, genotype 1:

We count the number of octopaminergic neurons pre-synaptic sites in five young (5 day-old) and five old (30 day-old) fruit flies. As it has been said in the qualitative analysis and as it can be shown in Fig. 4.43.a&b, no obvious difference in this number can be seen without a more careful analysis. We perform a t-test between the young and old cohort and found a Pvalue of 0.1757 (Fig. 4.43.c) showing no statistical differences in the evolution of number of connection with octopaminergic neurons within time for the fruit fly.

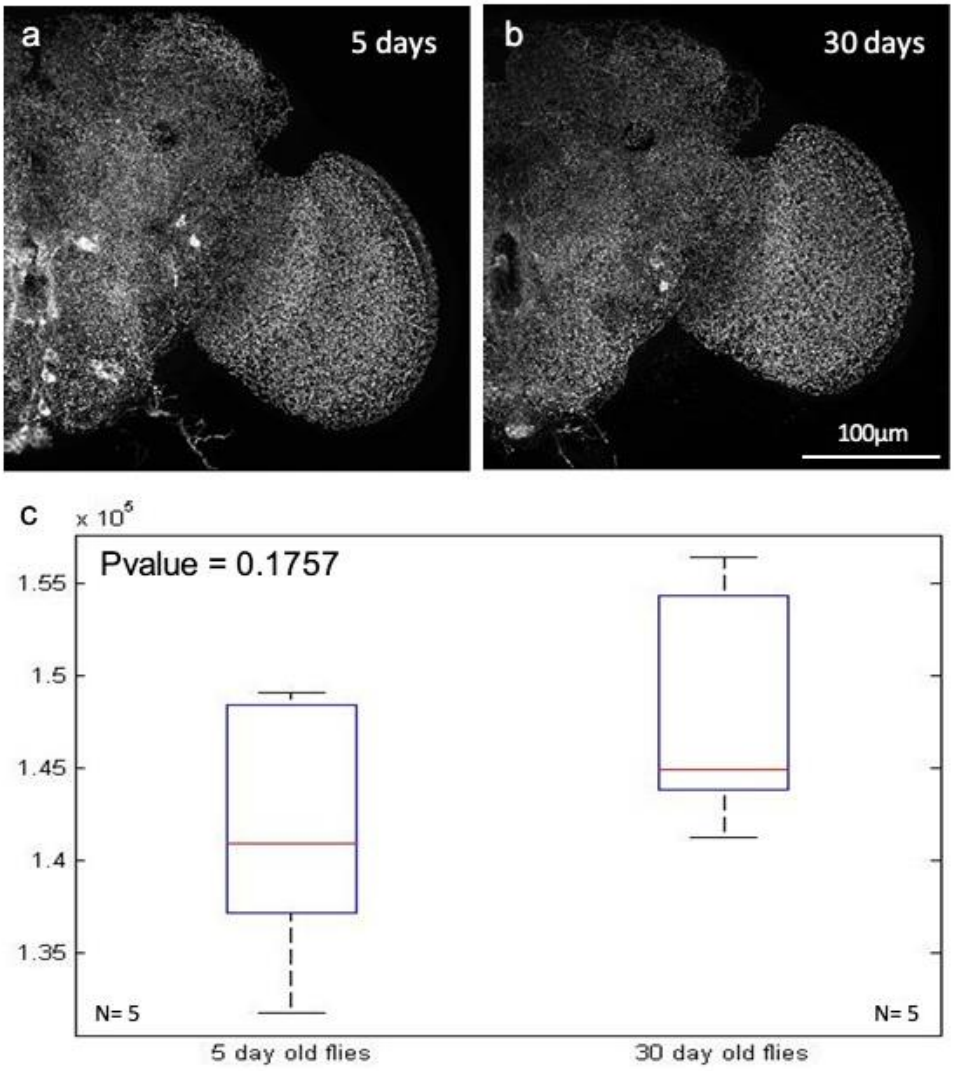

Figure 4.43. Quantitative analysis of octopaminergic neuron pre-synaptic sites between, (a) 5 day-old flies and, (b) 30 day-old flies, (c) Boxplot of the t-test and Pvalue = 0.1757, no evolution of the number of octopaminergic neurons pre-synaptic sites between young and old flies.

Experiment 1, genotype 2:

We perform a similar analysis for the dopaminergic neurons pre-synaptic sites. Similarly, no difference can be observed by a simple qualitative analysis as it can be seen in Fig. 4.44.a&b. After counting the number of synapses for 5 young and 5 old flies we compare this number with

a t-test and obtain a Pvalue = 0.9775 (Fig. 4.44.c). In conclusion, dopaminergic pre-synaptic sites number seems to be stable within time.

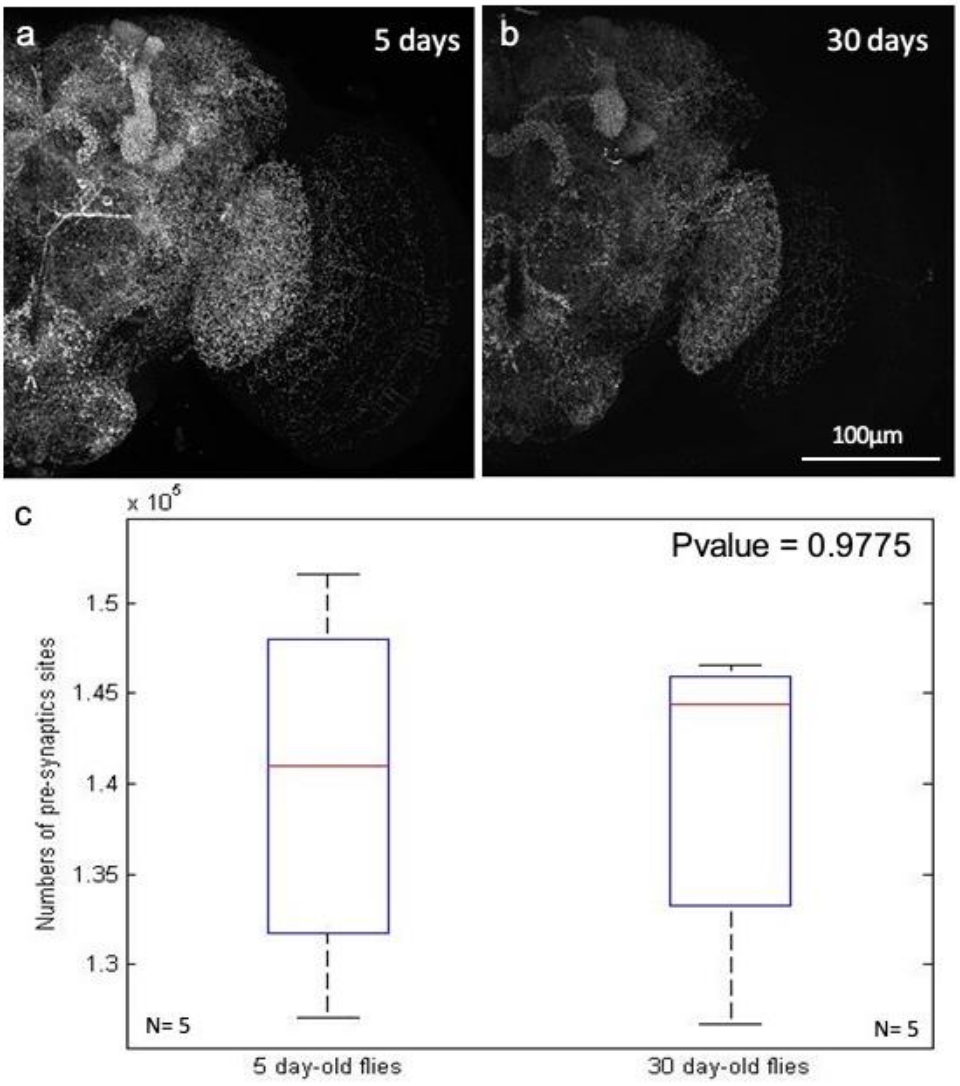

Figure 4.44. Quantitative analysis of dopaminergic neuron pre-synaptic sites between, (a) 5 day-old flies and, (b) 30 day-old flies, (c) Boxplot of the t-test and Pvalue = 0.9775, no evolution of the number of dopaminergic neurons pre-synaptic sites between young and old flies.

Experiment 2, genotype 1:

In this experiment we compare octopaminergic neurons deficient flies to control flies at different times (5 and 30 days).

For 5 day-old flies, the qualitative analysis did not highlight any difference between Kir flies and control (Fig. 4.45.a&b). After plotting the boxplot we can notice a slight decrease in the number of synapses (Fig. 4.45.c), however, the Pvalue equals to 0.2521 rejects this hypothesis, there is no significant difference between Kir and control for 5 days old flies.

For 30 day-old flies, we could notice big variations for Kir samples. Some of them seem to show a normal number of synapses whereas others present a much smaller number (Fig. 4.46.a&b). We statistically confirmed this by counting the pre-synaptic sites in both control and Kir flies and performing a t-test (Fig. 4.46.c). The Pvalues of 0.0052 attests of a significant difference between synapse numbers for 30 day-old flies. By comparing the mean of Kir and control flies we can notice a 20% decrease of synapses in Kir fly brains. This is consistent with the abnormal behavior highlighted in the previous section.

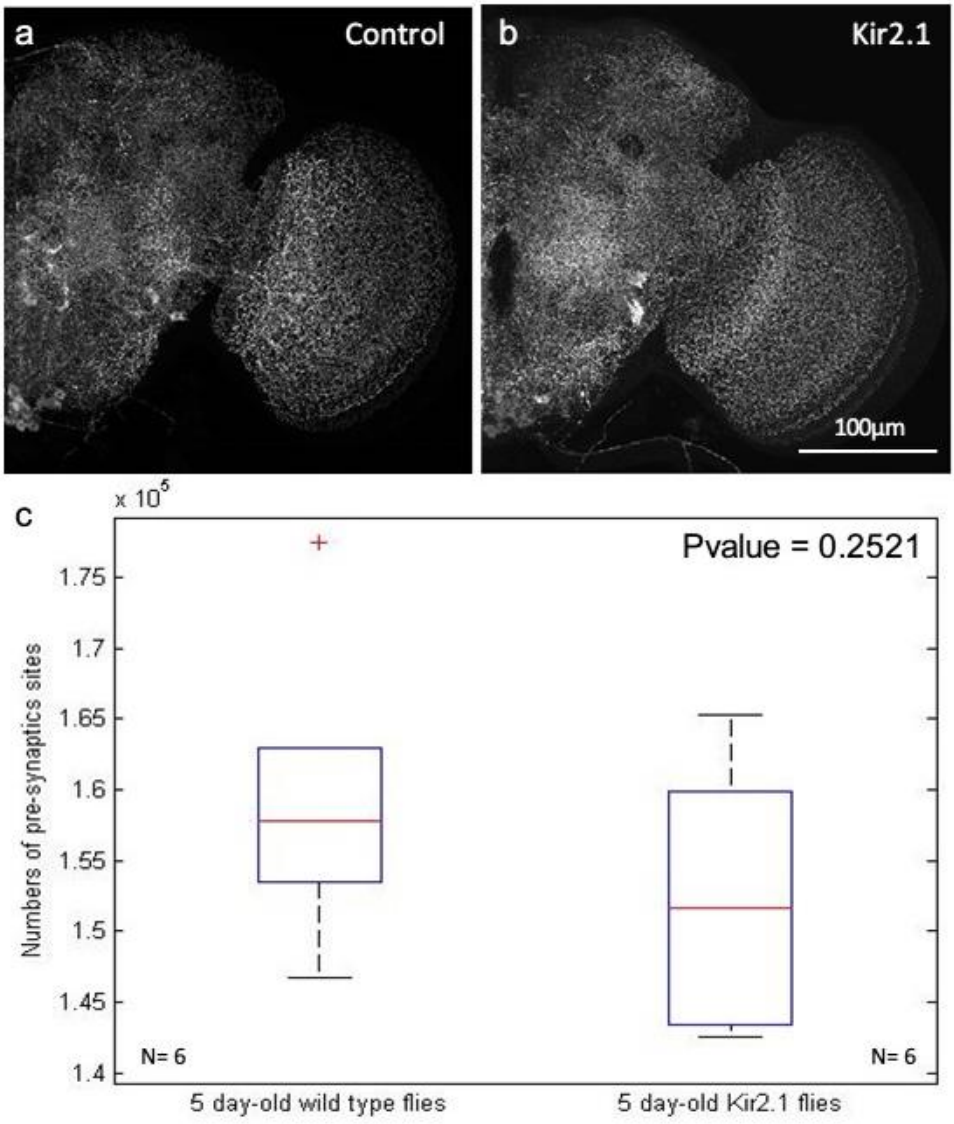

Figure 4.45. Quantitative analysis of octopaminergic neuron pre-synaptic sites between, (a) 5 day-old control flies and, (b) 5 day-old Kir2.1 flies, (c) Boxplot of the t-test and Pvalue = 0.2521, no difference of the number of octopaminergic neurons pre-synaptic sites between control and Kir2.1 5 for day-old flies.

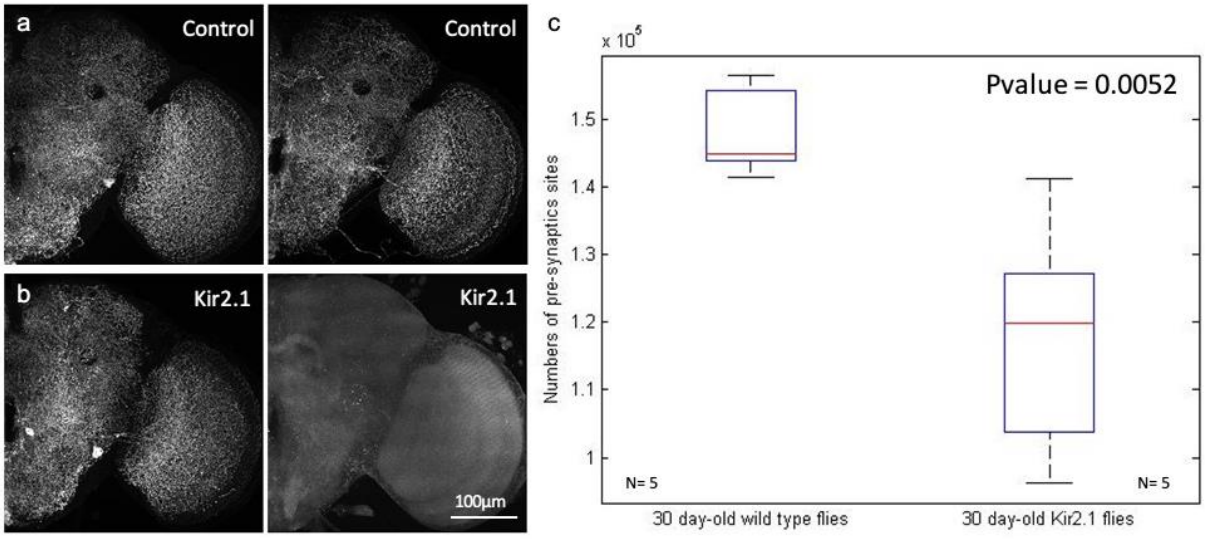

Figure 4.46. Quantitative analysis of octopaminergic neuron pre-synaptic sites between, (a) 30 day-old control flies and, (b) 30 day-old Kir2.1 flies, (c) Boxplot of the t-test and Pvalue = 0.0052, Significant difference of the number of octopaminergic neurons pre-synaptic sites between control and Kir2.1 for 30 day-old flies (20%).

c. CONCLUSION

A summary of these results is shown in Table 4.6 (Annexes).

Part 5
Discussion

Part 5 Discussion

1. CONFOCAL MICROSCOPY AND REGISTRATION

Due to its numerous advantages, confocal laser scanning fluorescent microscopy is commonly used in many biological laboratories: a large variety of cell types of relatively wide range of sizes can be visualize for most of organisms. Despite the efforts of microscopy manufacturers who try to provide objective lenses with longer working distances than previous models, diffraction and scattering of lights within the optically uneven specimen still causes practical limitations such as a short depth of imaging which makes the precise study of thick samples uneasy.

a. ALTERNATIVE SOLUTIONS

Many other types of microscopy can also be used for such study. Among them, another candidate could be two-photon microscopy, also widely used for biological research, because long-wavelength infrared light of the excitation laser is less prone to diffraction and scattering. However, emission light from the labeled signals suffers from the same optical problems as in single-photon confocal microscopy.

Another solution to get a high resolution image of a thick sample is the multiplication of imaging from different point of views either from both sides, like in this study, by flipping the sample or from the same side, by using microtomes that progressively cut off the sample surface. In both case, a set of overlapping images are taken and must be accurately stitched. Even though those kinds of techniques are not new and are commonly used, few algorithms exist to perform an accurate registration and stitching.

Using the same labelling techniques with fluorescent dyes, laser scanning confocal microscopy is not the only way to image our samples. An alternative solution is Light Sheet Fluorescent Microscopy (LSFM). In contrary with confocal microscopy, in LSFM, the sample is illuminated by a laser light beam focused in only one direction (laser light sheet) perpendicularly to the direction of observation. Similarly to the solution proposed in this study to overcome the problem of loss of quality with depth, in LSFM, the sample is imaged in several directions and the resulting views are then fused in a final high resolution picture. However, unlike confocal microscopy, this is done automatically by rotating the capillary (thin tube of agar containing the sample) inside the microscopy at a priori defined angles.

One of the advantages of such techniques is the acquisition speed. Because, the imaging is done using sheets of light instead of a point by point illumination, the acquisition of our three channels sample of the Drosophila brain took around twenty minutes (for four views) versus five to six hours in confocal microscopy for a similar sample. However, it must be noticed that the image resolution is lower for LSFM (1200x1200xX voxels at a 0.177x0.177x0.469µm resolution) than for confocal microscopy (1600x1600xX voxels for a 0.2x0.2x0.2µm resolution). For both microscopies, the resolution around z is smaller than in other directions. In LSFM, this can be corrected by multiplying the number of view (imaging in the perpendicular direction) but this also increase the complexity of the fusion of all views. The data size is also much bigger for LSFM due to these multiple views (50Go for four views of the Drosophila brain vs 16Go in confocal microscopy for similar samples).

However, because the sample is fixed in agar gel and does not float in a PBS like in confocal microscopy, the tilting is almost absent in LSFM making a three dimensional registration unnecessary, limiting the mistakes due to incorrect tilting correction.

The noise induced by LSFM is very different from confocal microscopy. Because the sample is illuminated perpendicularly to the direction of observation, the noise does not decrease with

depth but with the distance from the border of the sample (center very noisy but clear borders). Therefore the noise model developed in this study cannot be applied to LSFM images.

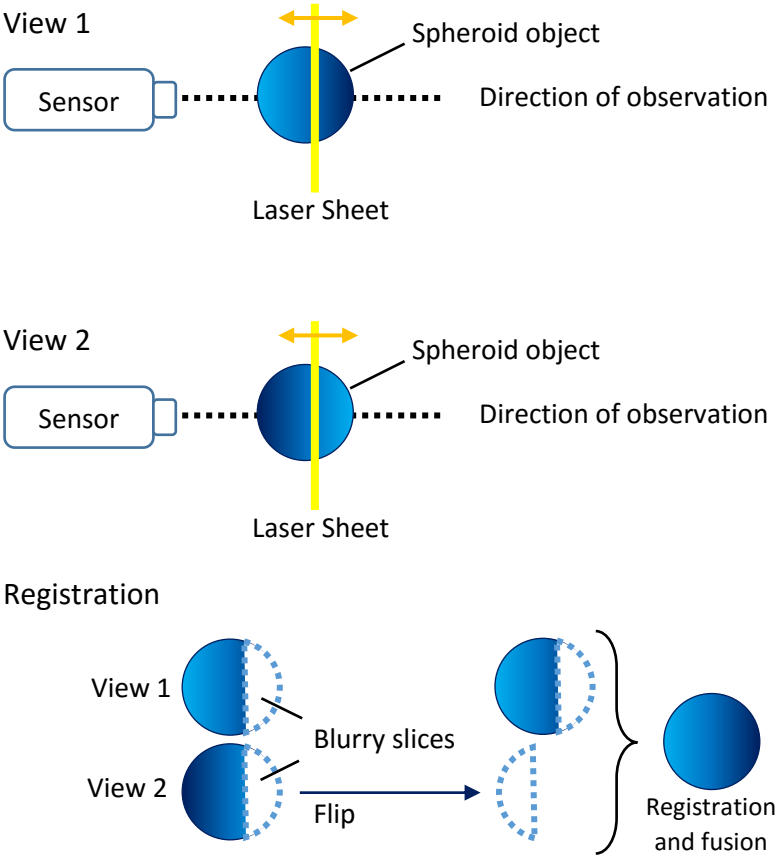

Figure 5.1. Imaging and registration of Light Sheet Fluorescent Microscopy stack of images.

The SIFT registration was tried for LSFM images for different types of samples. The first attempt was made for spheroid structures such as round cluster of cells. Because in LSFM, the samples are completely overlapping, we select, in two opposite views (180°), only the clearest part, discarding the blurry one (Fig. 5.1). Using the two overlapping parts, we try a SIFT registration. Because the tilting is very small due to the agar gel fixation a registration in translation along x and y and in rotation around x is sufficient. We register a cluster of cells with a shape of spheroid (Fig. 5.2). Using this procedure, we could achieve a good registration. Because a first loop in the algorithm already shows a peak in the overlap detection curve (Fig. 5.3), several iterations could refine the registration.

Encouraged by the good result of the registration on spheroids, we then perform the registration on more complex structures: halves brain of Drosophila melanogaster (octopaminergic neurons). To reduce the problems of diffraction and refraction of the light going through the whole sample we did the acquisition with the samples perpendicular to the z axis (Fig. 5.4).

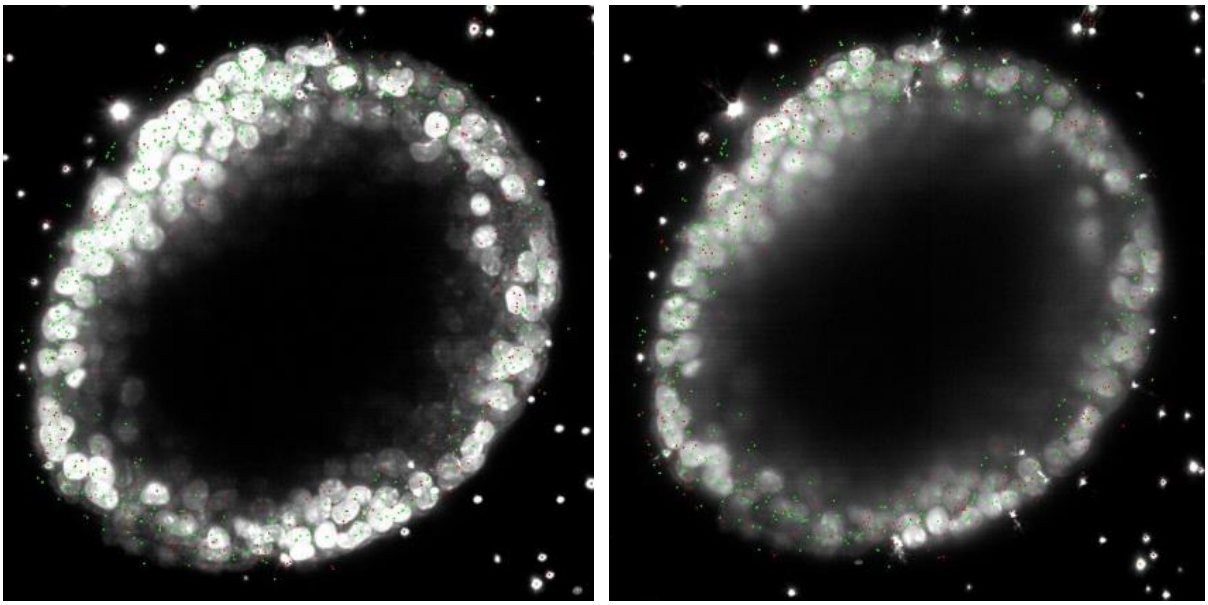

Figure 5.2. Registration of a cluster of cells (spheroid) acquired by LSFM. Identical slices and corresponding matching point (green) for (a) the front stack and (b) the back stack.

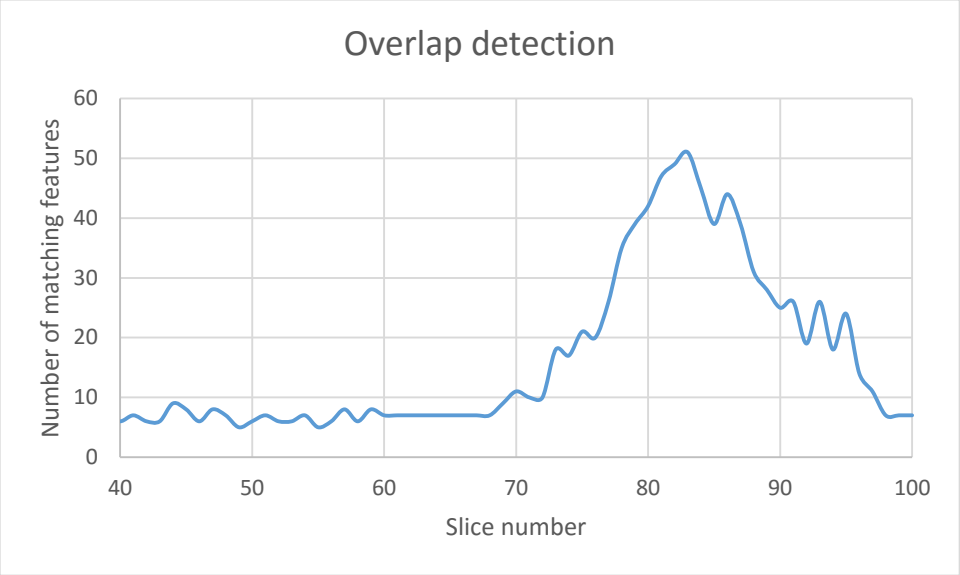

Figure 5.3. Overlap detection curve for LSFM image of a cluster of cell. The bell shape curve can be clearly seen.

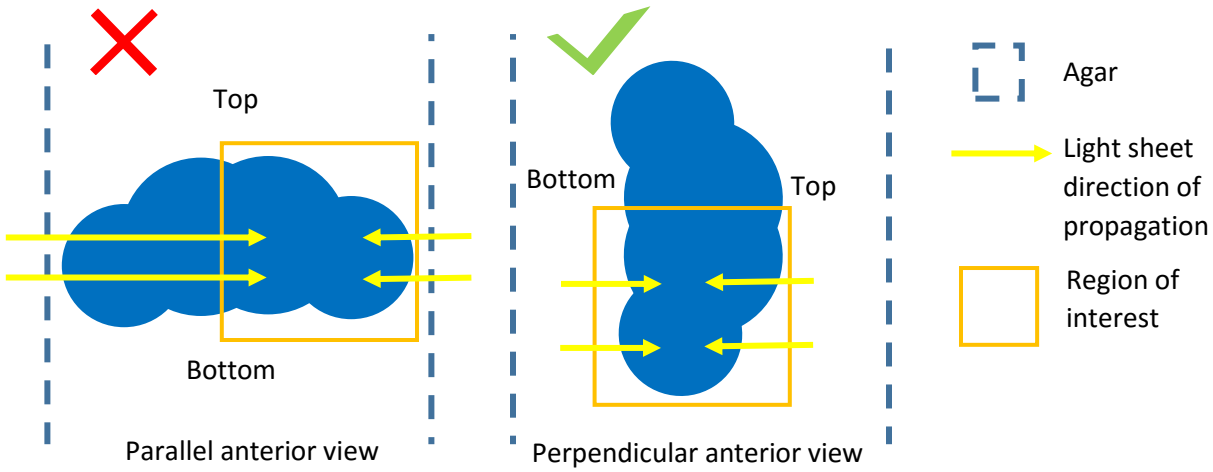

Figure 5.4. Light Sheet Fluorescent Microscopy Acquisition procedure for Drosophila melanogaster.

Similarly to the study done for confocal images, we tried to register and fused two opposite views. Both views were taken at a very high resolution (0.177x0.177x0.469µm) for an image size of 1920x1920 pixels with a variable size along z. Despite a similar resolution on x and y in confocal (0.2x0.2µm square pixel), we were unable to accurately register the two stacks (Fig. 5.5&6, orange curve in the overlap detection graph). However, the diminution of the resolution

(0.354x0.354x0.469µm), lead to a better estimation of the overlap (blue curve in the overlap detection graph) and therefore to a better registration (Fig. 5.6). In the front and back stack the level of blur appear very different and make the comparison uneasy.

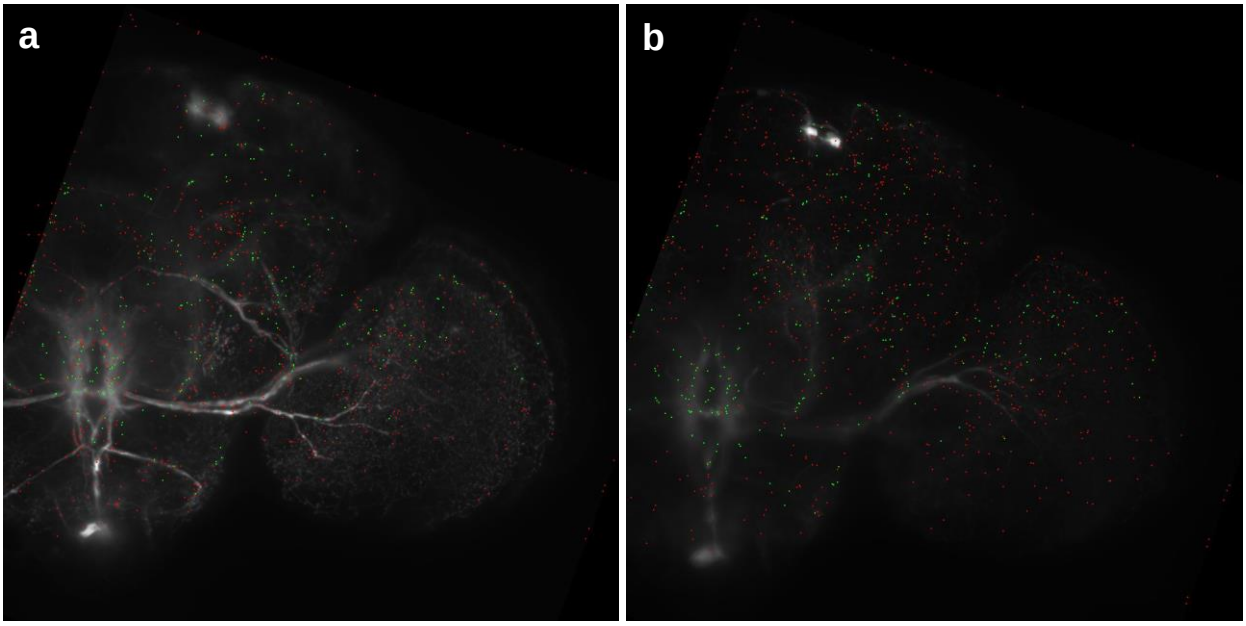

Figure 5.5. Registration of the brain of Drosophila melanogaster acquired by LSFM. Identical slices and corresponding matching point (green) for (a) the front stack and (b) the back stack.

Figure 5.6. Overlap detection curve for the same set of Light Sheet Fluorescent Microscopy Acquisition images of Drosophila melanogaster brain of different resolutions: 0.177x0.177x0.469µm (orange curve) and 0.354x0.354x0.469µm (blue curve).

One of the reasons of such issues encounters to register fly brains samples imaged with LSFM compared to confocal microscopy is the non-uniformity of the noise within a slice. Indeed, in confocal microscopy, the noise will be similar for each pixel of a section but different for each section of the stack whereas in LSFM the sample will be noisy in section far from the sensor due to the light refraction but also in the center part of the object. Because of this identic structures appear very different in the opposite views: structures that are blurred in a view can be clear in the other one and vice versa (Fig. 5.5&7). Because SIFT is looking for similar structure within the stack, the keypoints detected will be not be the same for both image and thus a precise registration is difficult if not impossible. Compare with the previous dataset, the fly brain is a heterogeneous sample of thin and thick objects, whereas the spheroid is an isotropic cluster of isotropic objects (sphere) of similar size. The light is then not refracted the same way by the structures within the Drosophila brain (Fig. 5.7).

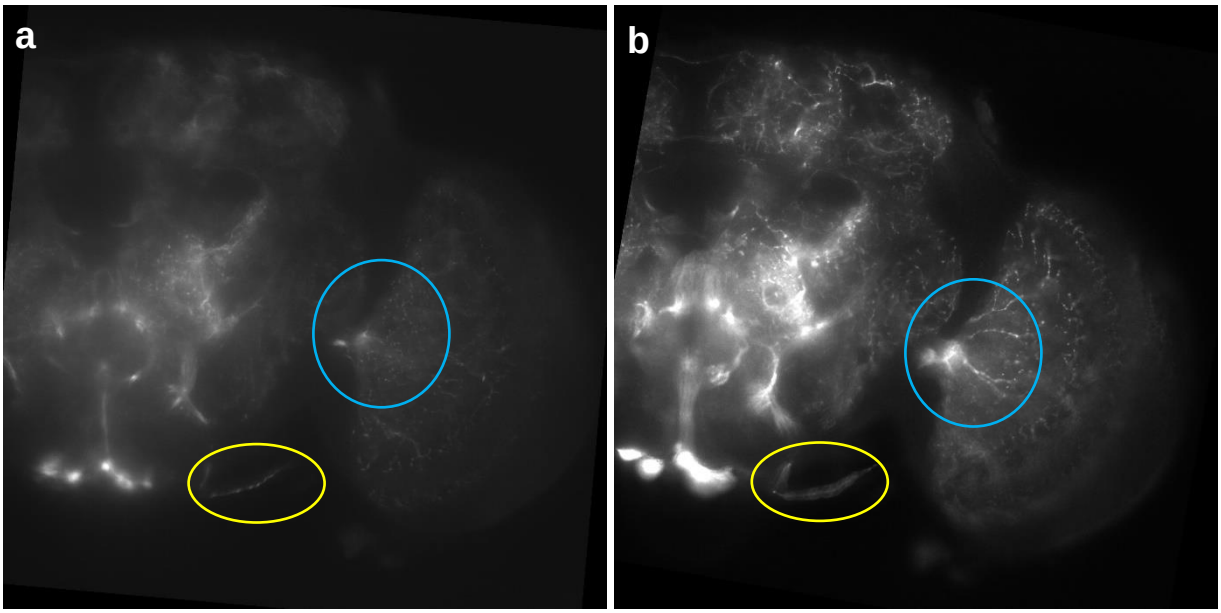

Figure 5.7. Similar slice in the front (a) and back (b) stack of the fruit fly brain taken by LSFM. Neurons that appear blurry in (a) are clear and sharp in (b) (blue circle) and vice versa (yellow circle).

To overcome this problem, we tried register and fused two other views: from the top and from the bottom of the brain, expecting a higher uniformity of the noise in each slice because of the thinner size of the brain along z (Fig. 5.8). However, because in LSFM the resolution in depth is

much smaller than the resolution in the plan of observation (twice smaller), the image quality of the anterior view is significantly smaller making the registration uneasy and further study practically difficult and inaccurate (Fig. 5.9).

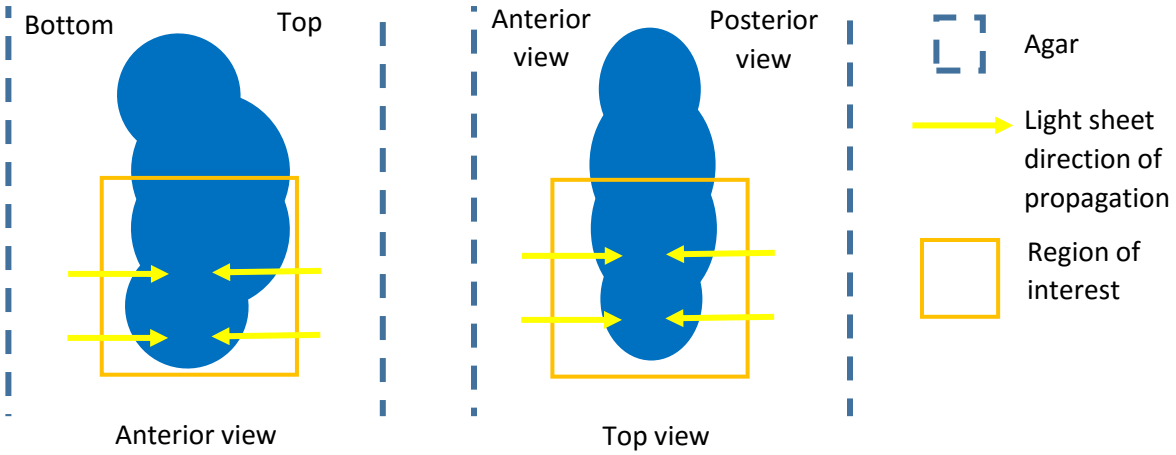

Figure 5.8. Modified procedure of LSFM image registration of Drosophila melanogaster brain.

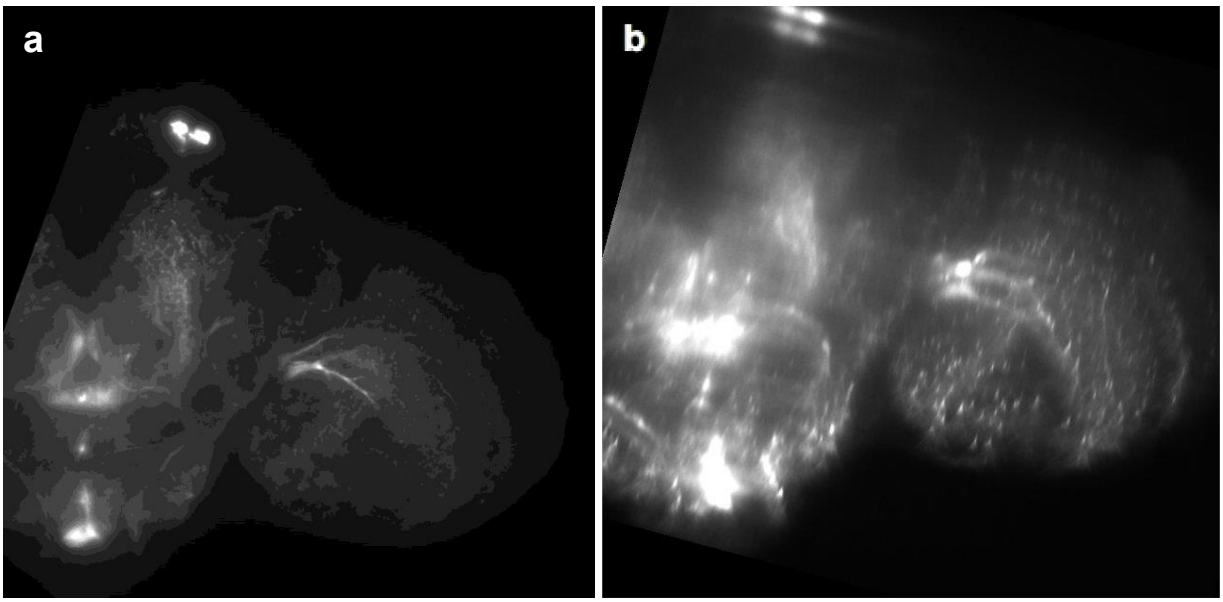

Figure 5.9. Qualitative comparison of (a) a Light sheet parallel to the anterior view and (b) a Light Sheet perpendicular the anterior view at the same resolution.

For a better registration a multiscale SIFT detection would give better results but this remains to be implemented. The fusion of the various views is also a challenge because only clear structures

must appear in the final reconstructed image. Ideally, the fusion must be done by linear blending to smooth the transition between the two stacks. However in this case, because structures can appear blurry in one of the stack and not in the other, the linear blending will not conserve the sharp objects. To preserve a little bit of this sharpness, a simple way to fuse the images is conserving maximum of the voxel intensity values for each position within the overlap. Fibers appear then bright with a blurry halo. Another way would be to filter separately the front and back stack with a 3D multiscale vesselness filter to preserve only sharp neurons (in focus) in both stack and fuse the filtered images.

It is worth noting that SIFT is not the only local descriptor that performs well in such different fields including image recognition or registration, although it is known to be one of the most efficient. Many other descriptors have been developed and introduced in the literature under the form of filter-based descriptors such as steerable filters and Gabor filters, distribution-based descriptors such as SIFT, RIFT (rotation-invariant feature transform) and GLOH (gradient location-orientation histogram), or derivative-based descriptors such as local derivatives, Florack descriptor and local gray value invariants. A detailed description and a comparison of those descriptors accuracy have been performed by Li et al. (2008).

b. REGISTRATION ALGORITHMS

To stitch substacks, the position and orientation of the two substacks must be registered. Most of the current algorithms assume that the planes of the sections of the two substacks should be completely in parallel. For example, a Fiji stitching plugin developed by Preibisch et al. (2009) provides various benefits such as fast execution time and simple use. The purpose of this software meets ours well, but the plugin does not perform any 3D registration and do not correct rotation mismatches around x- or y-axes, which makes it unusable if tilting – even a slight one – exists between the two substacks.

To compare the effect of tilting correction, we tried to register the same front and back substacks of the fly brain neurons using both the previously described Fiji plugin and our 3D-SIFT Volume Stitching plugin (Fig. 5.10). As expected, because the Fiji stitching plugin does not fix tilting, the resulting registration matches in some parts of the image but not in other parts. On the contrary, 3D-SIFT plugin corrects mismatch of the tilted planes to achieve complete registration throughout the image field.

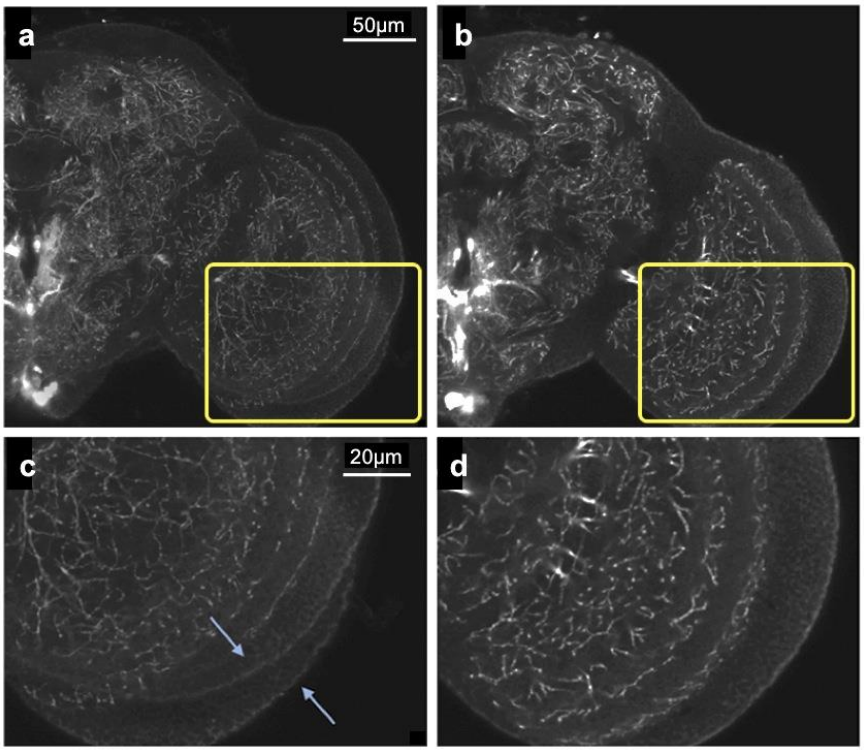

Figure 5.10. Registration comparison for the same pair of substacks (down-sampled substacks with 800 x 800 x 300 voxels, resolution 0.4 x 0.4 x 0.4 µm). A single-section view after the images of the front and back substacks are superposed. (a) Fiji stitching registration. (b) 3D-SIFT registration. (c) Zoom up view of the Fiji registration. Note that, although the images of the two sections are registered nicely in the central part of the sample (a), the two images appear misaligned in the peripheral part (two arrows in c). (d) Zoom up view of the 3D-SIFT registration. The two images are registered completely throughout the view.

The 3D registration proposed in this manuscript is obtained by the repeated use of 2D SIFT on three orthogonal planes. This demonstrates the extended applicability of the well-established,

multithreaded fast 2D SIFT algorithm by Saalfeld (developed in 2008 for the FIJI plugin Linear Stack Alignment with 2D SIFT) to our particular demands. Whereas the original 2D SIFT plugin was developed for aligning a series of single sections of light or electron microscopy, in which registration is needed only in the 2D plane of sections, our algorithm is finding the best way of aligning and stitching 3D images by maximizing the number of SIFT matches between two overlapping 3D substacks. We also employed partial MIP of multiple slices to maximize the number of matches in the SIFT comparison. This improves not only accuracy of matching but also computation speed compared to the comparison of single slices. In addition, we separated the steps of transformation formula calculation and application of the obtained registration parameters. This enabled two features that have not been available in the original 2D SIFT plugin. First, registration computed for one channel can be applied to the data of different channels. This is essential for handling fluorescence microscopy data many of which contain multichannel images. And second, preprocessed images that are optimized for future extraction can be used for alignment, while the final concatenation is performed on the raw data. This is indispensable when the stitched data will be used for subsequent analyses and image manipulation.

Whereas we achieved 3D registration with the repeated use of 2D SIFT, SIFT in true 3D space has also been proposed for motion recognition of video images (Scovanner et al. 2007) and object recognition for X-ray computer tomography images (Flitton et al. 2010). Although the same approach can in principle be applied to develop an image registration software, the choice of 2D SIFT in 3D space is well adapted in our case, because the specific image acquisition sequence considered in this article – stitching of microscope image substacks obtained from the same sample – induces more important rotations around z-axis than the tilting around other axes; the first iteration of registration in x-y plane is thus very likely to bring a strong improvement. This prior would not be used with 3D SIFT registration, which would blindly look for solutions in any direction of the 3D space. Therefore, the number of iterations requested with a 3D SIFT algorithm to reach a fixed convergence criteria could be higher in principle than with the 2D SIFT in 3D space.

Point-based registration, developed originally for light sheet microscopy (Preibisch et al. 2010), can also register overlapping image stacks in 3D. As the key for registration it requires the use of fluorescence beads that are embedded firmly in agar gel with the sample. Registration error would occur if beads and samples are put in popular fluid mounting medium such as glycerol used in this study. Preibisch et al.'s algorithm was also applied for stitching a large set of tiles of the two-photon tomography image data of the mouse brain (Economo et al. 2015). Here, instead of fluorescence beads embedded along with the sample tissue, fluorescence from the endogenous aging-related pigment granules called lipofuscin, which are distributed across the mouse neural tissue, was used as the keys for registration. This approach was not applicable to our samples, because such granules do not seem to be distributed ubiquitously in young fly brains.

Although the primary purpose of our 2D-SIFT-in-3D-Space Volume Stitching plugin is to stitch two image substacks, its registration feature is achieved by comparing the signals of two overlapping volume stacks. In this respect it shares certain features with the registration algorithms such as BrainAligner (Peng et al. 2011) and CMTK (Computational Morphometry Toolkit) (Rohlfing 2011), which are developed solely for registering volume data obtained from different samples into a common template and have been used extensively for registering 3D images of tens of thousands of samples of Drosophila melanogaster and other brains. BrainAligner and CMTK offer extensive affine and non-rigid (warping) transformation, because they assume that the volume data to be compared should be obtained from different samples. On the contrary, 2D-SIFT-in-3D-Space Volume Stitching performs only simple affine transformation because it assumes that the two data should derive from the same sample and only rotation and translation are expected to occur during the acquisition procedure. Moreover, because only a small portions of the two substacks overlap, for the rest of the volume there is no reference for non-rigid transformation. Unlike 2D-SIFT-in-3D-Space, BrainAligner and CMTK do not offer stitching function because they assume that the two volume data should cover similar parts of the specimen.

In spite of such differences, approaches to the registration of two overlapping volumes are worthy of comparison. BrainAligner uses a similar approach to that of 3D-SIFT that it first extracts

landmarks based on feature detection. Thus, even though the software has been optimized for the registration of continuous-looking background labeling such as those with nc82 pre-synaptic neuropil marker, it can be used for a variety of other images including those with fine fibers. Whereas 3D-SIFT actually compares features in 2D cross sections of partial-MIP slices, BrainAligner extracts features in 3D space. The latter appears to be very appropriate for 3D image registration, because its landmarks are actual three-dimensional points that should in principle give accurate 3D registration. BrainAligner, however, uses a semi-manual method to detect features to be compared. The features (or landmarks) are defined manually in the target brain as point of high curvature, also called corners or edges, which indicate high changes in the contrast of the image. The algorithm then automatically looks for matching landmarks in the second image that satisfy criteria such as maximizing mutual information and correlation. Defining landmarks manually is a time consuming task. It suits well for the purpose of image registration against a template, because the target landmarks need to be defined only once in such a case. The approach does not seems adapted to our purpose, because the pair of volume data to be registered are always unique in our case; the landmarks painstakingly defined manually will be used only once for the registration of that particular sample.

CMTK, like 3D-SIFT, compares two volumes automatically without manual intervention. Unlike 3D-SIFT, CMTK register volumes based on intensity values. This is effective when comparing volume data with continuous labeling. Indeed, CMTK often provides better results than BrainAligner when registering samples with nc82 labeling. On the other hand, CMTK cannot satisfactorily register the images of neuronal fibers such as those used in our study, even if the two image stacks completely overlap.

Thus, although various approaches have been proposed for registering 3D volume data, none of them seems to meet our particular demands without extensive modification (Table 5.1). Our plugin would therefore provide novel features that have not previously been available to the community.

	CMTK (Fiji)	Brain Aligner (Peng, 2011)	Fiji volume stitching	Linear Stack Alignment with SIFT (2008)
Sample properties	Volumes from different samples Complete stacks	Volumes from different samples Complete stacks	Volumes from same sample Half stacks	One sample misaligned
Transformation	Warping	Warping	2D linear	2D linear
Sample type	Background labelling	Requires manual landmarks	Anything	Anything
Main issue	Not optimized for fibers	Landmarks selection	No tilting correction	Registration within the stack

Table 5.1. Comparison of Registration algoithms

Although 2D-SIFT-in-3D-Space Volume Stitching should in principle be more efficient than voxel-to-voxel comparisons, slice by slice SIFT comparison required for precise detection of overlapping parts is computationally hungry. Stitching of two 1600 x 1600 x 500 substacks takes about hours with our workstation equipped with a 6-core 3.4GHz Core i7-4930k CPU. This is in part because the current program written in Java may not be optimized for multi-thread parallel processing. Performance may be improved by designing the software code for massive parallel processing.

As explained earlier, current version of 3D-SIFT Volume Stitching performs only affine transformation. This is because the section images of the same sample obtained from different sides should have same size and morphology. However, we found that this assumption may not always hold true. In a few cases we noticed that one side of the image could not be registered completely even when complete match was achieved on the other side of the image. There is apparently a slight non-linear distortion between the section images of the same part of the sample obtained from different substacks (Fig. 5.11). This is most likely because of the optical aberrations caused by the microscope objectives.

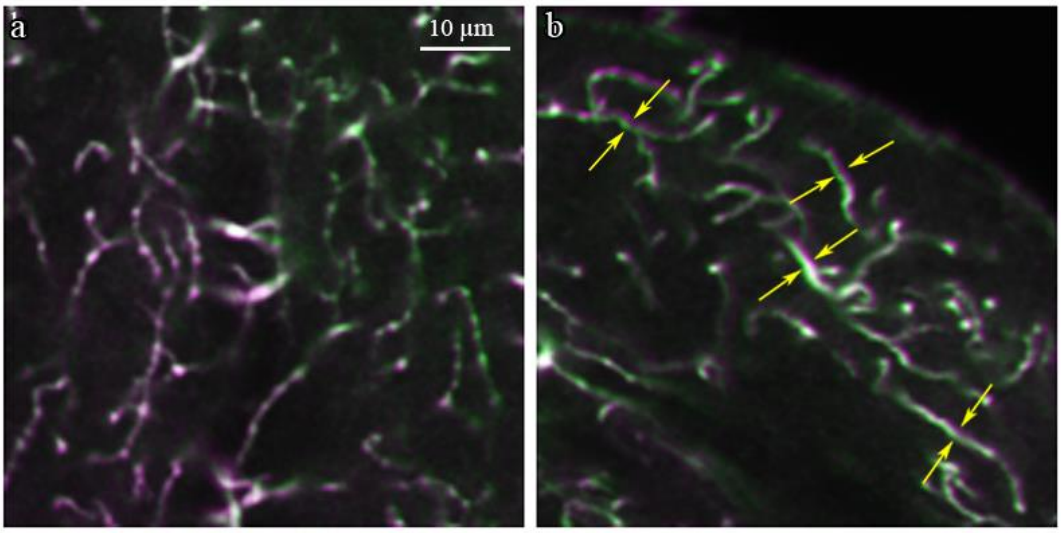

Figure 5.11. Illustration of the registration errors caused by optical aberration. Superposition of the front substack (green) and back substack (magenta). (a) The two substacks are registered nicely in the central part of the image. (b) In the peripheral areas of the image, however, small mismatch tends to remain regardless of the registration around any axes (arrows).

c. REMAINING PROBLEMS

Among the Seidel's five aberrations, spherical aberration, coma and astigmatism mainly affect the sharpness of the image without affecting the location of the signal. Those aberrations may cause uneven sharpness in the image field. Then sharper parts of the image with the highest feature vectors concentration will have a stronger influence on the model computation, leading to perfect registration in those parts but a shift between the front and back stacks in the opposite side of the image. Moreover, field curvature and distortion cause distorted projection of the signal distribution in the sample to the obtained 3D image space, making straight lines in the sample appear curved along the z-axis (field curvature) or x- and y- axis (distortion). An objective lens tuned for the best performance in certain focal depth may not perform optimally at shallower or deeper levels. Thus, the optical sections of the same part of the specimen but obtained from different sides (i.e., at different depth) may not be identical. To avoid such complication, addition of non-linear registration feature might be helpful even for concatenating

substacks obtained from the same sample. Also, reduction of optical aberrations by implementing adaptive optics should reduce such problems (Lowe 2004, Meijering2010).

2. REGISTRATION RESULTS AMELIORATION

A two-steps acquisition procedure can achieve high resolution images linearly “clear” throughout the entire sample if the registration is correctly performed. However, the registration result greatly depends on the quality of both substacks of images (front and back substacks). We already noticed that a difference in the signal intensity between the two stacks can lead to registration errors, but this can be corrected by an – even rough - intensity adjustment.

Another critical point during the image acquisition is providing a “calm” environment. Indeed, to be able to take pictures from both sides, the sample is mounted between two thin cover slips, a long and a short one. At the contrary of the thick glassed, the thin ones offer less protection to the sample which becomes very sensitive to air movement (air conditioner), vibration (doors) and pressure (objective pressing the slip).

a. DATA PREPROCESSING: INTENSITY AND CONTRAST CORRECTION

i. Problem and proposed solution

As previously discussed, laser scanning microscopy is a powerful tool and is then widely used to obtain three dimensional stacks of serial thin optical sections from organic and inorganic samples. However the possible depth of imaging is limited by two factors: the working distances of microscope objectives and the image degradation resulting from the light scattering within the sample in the deeper layers of the specimen. The light is then partially lost causing a diminution of the sensibility and limited depth penetration. In a few words, the signal intensity in fluorescent confocal microscopy techniques tends to decrease with the depth (along z axis) and therefore

images of the sections that are deep in the specimen tend to appear darker (i.e., having lower intensity) than those that are close to sample surface and must then be adequately compensated.

We develop our registration/stitching technique in order to overcome this problem, particularly visible for great depth (more than 100µm). However this issue subsists, at a lower scale within the two substacks.

Moreover, in the deepest sections, where the two stacks are overlapping imaging is done twice: for both the front and back stack. The second image tends to be even darker than the first one due to the excitation of a smaller number of Fluorophore. This phenomenon is called photobleaching (Ito et al 2003) and can cause many processing problems.

Because of this two problem, slices deeply located in the specimen tend to appear darker (having lower intensity) and flatter (having lower contrast) than those that are close to sample surface. Even if SIFT is relatively robust against brightness differences between two images to be registered do to the mathematical matching of features vectors instead of raw pixels, a too big shift between the two images will make a smooth stitching uneasy if not adequately compensated. It then appears helpful, if not necessary, to perform a pre-processing of the two image substacks to match their brightness and contrast at sections of similar depth.

In order to address this problem we developed a Fiji/ImageJ plugin called Progressive Intensity and Gamma Correction (Fig. 5.12). This plugin progressively increases or decreases the intensity and/or gamma contrast of each slice of a 3 dimensional of images at a rate defined by the user. In confocal microscopy images, the deepest slices often appear so dark that the signal is barely visible and should then be increased. However, the surface sections appear much brighter and an intensity enhancement will saturate the signal causing a loss of contrast and thus of information. A constant increase of the signal intensity must be avoided. In order to overcome such saturation issues, the enhancement must be progressive throughout the stack from shallow to deep sections, from for example, no enhancement in the first slices (100%), to signal intensity

doubling (200%). However, in real samples, the intensity degradation is rarely uniform, and to solve this problem, we provided several interpolation laws: constant, linear and exponential with variable steepness. The Progressive Intensity and Gamma Correction plugin corrects progressively the intensity of each slices of an image stack by multiplying each voxel values by a given percentage that varies according to the depth and the selected law (Annexes, Fig. 5.13). Three interpolation laws are available:

1) Constant: IE = c with IE intensity enhancement and c a constant, all the pixels are enhanced by the same value (Fig. 5.12.b, blue curve)

2) Linear: IE = za + b with a = (IE(Zm) – IE(1))/(Zm – 1) and b = IE(1) – a; Zm the number of slices, IE(1) the intensity enhancement values chosen for the first slice and IE(Zm) the intensity enhancement value for the last slice, the intensity enhancement value varies linearly between two values IE(1) and IE(Zm) set by the user (Fig. 5.12.b, green curve)

3) Exponential (IE = azg + b where a = IE(Zm) – IE(1))/(Zmg – 1) and b = IE(1) – a with g, a parameter accommodating the curvature of the exponential (Fig. 5.12.b, red and light blue curves)

Remark: we here use enhancement as the percentage each pixel will be multiplied by: a 200% enhancement means that signal values will be multiplied by 2 (100% increase) and a 50% enhancement will divide those values by 2 (50% decrease).

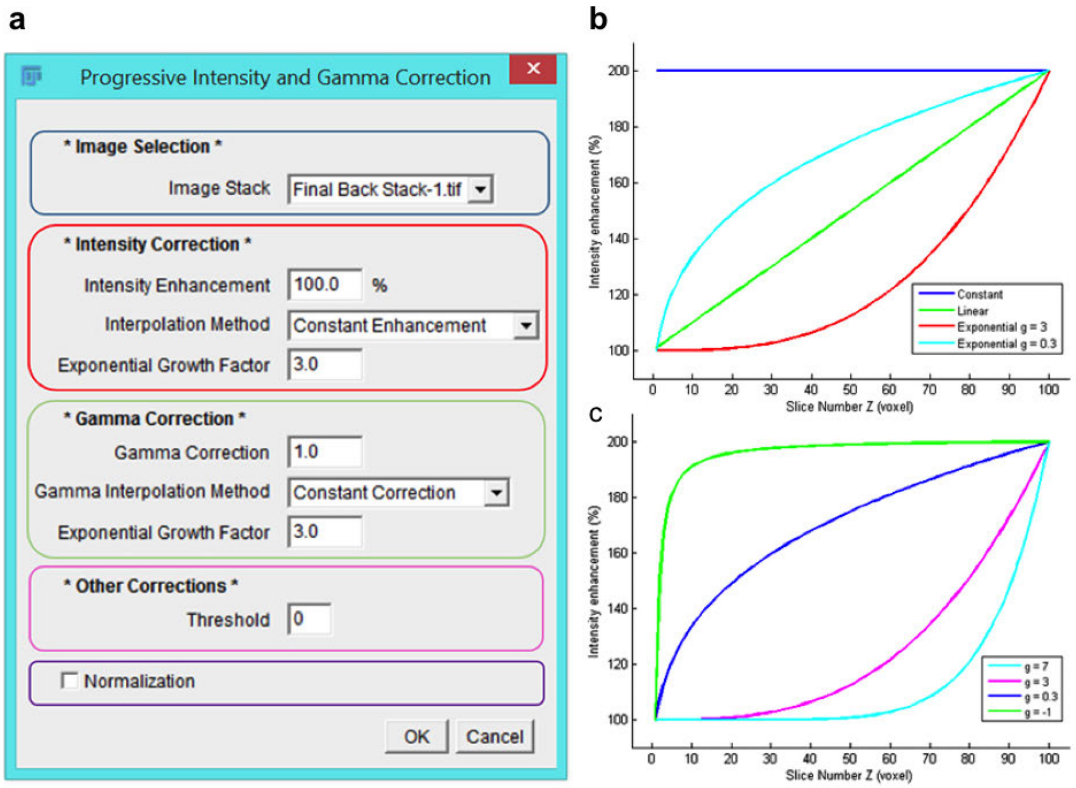

Figure 5.12. Intensity and contrast adjustment plugin, (a) Control panel of the *Progressive Intensity and Gamma Correction* plugin. First select the image stack to be corrected (blue panel), choose the intensity enhancement value (100% = no enhancement) and method for progressive interpolation (red panel): constant (blue line in b), linear (green line in b) and exponential (cyan and red lines in b), and the gamma correction value (1.0 = no modification) and interpolation method (green panel). Enter a threshold value if needed (magenta panel), and check normalization if necessary (purple panel), (b) The curvature of the exponential law can be set in the "Exponential growth factor" numeric field. Exponential growth factor g, here refers to the exponent of the power law $ax^g + b$, used to estimate the variation of correction, (c) If g < 1, correction will be done early within the stack (c, green and blue lines), whereas if g > 1, correction will be done late in the stack (c, magenta and cyan lines).

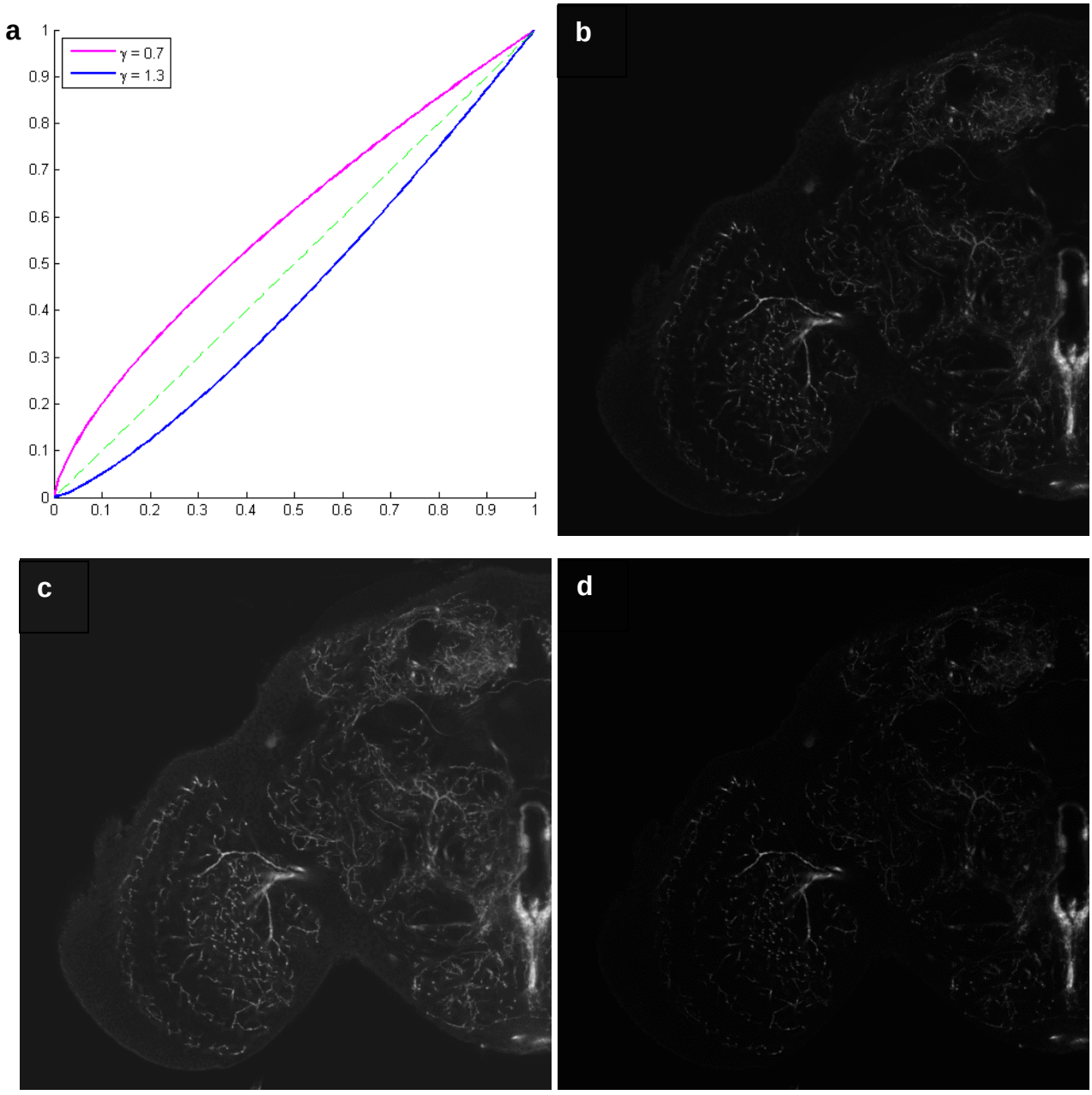

Figure 5.14. Example of gamma correction on a Drosophila Melanogaster brain image, (a) CTR gamma correction, the dotted green line indicate a linear transfer function (γ = 1), the solid lines are the CTR behavior for γ = 0.7 (magenta) and γ = 1.3 (blue), (b) Original image, (c) γ = 0.7 example, (d) γ = 1.3 example.

The main problem of this enhancement technique is that all the pixels of a slice are equally enhanced: the signal, but also the background noise because intensity enhancement increases the values of all the pixels at the same level. To overcome this issue, the gamma, roughly

representing the image contrast can be modified. Unlike intensity correction, gamma correction keeps the intensity of the darkest (black) and brightest (white) pixels while brighten or darken mid tones (gray pixels). This gives nonlinear but natural-looking correction of image contrast without causing signal saturation in bright pixels. Similarly to the pixel intensity, the contrast quality can be unequal through the stack and it often occurs that shallow section have a good contrast whereas the deeper slices show a poor one (contrast tends to become flatter in deep images) and then should often be applied in a progressive manner. The same interpolation system as the intensity one has been implemented such way that the user can choose the gamma value of the first and last slices, the value of the intermediated ones to be automatically computed by the program according to the same three laws: constant, linear or exponential (Fig. 5.14).

ii. The Fiji Intensity correction Plugin

We developed a plugin in java available on the Fiji platform. In this part, we give an example of the use of our plugin on a real stack of image: a three-dimensional image of neural fibers of the brain of Drosophila melanogaster (Annexes, Fig. 5.13.a).

Fig. 5.13.a2 (Annexes) is the first slice of this stack (we set the depth at 0µm), Fig. 5.13.a3 (Annexes) is the 50th (20µm) and Fig. 5.13.a. (Annexes) is the last one (100th, or 40µm). As we can see, the brightness is not constant within the stack as the last slice appear much darker than the first and intermediate one. For the sake of this example, we set the enhancement of the last slice at 200% (double the intensity). The interpolation law between the first and the 100th slice must then be selected.

A constant enhancement is in this case not satisfying as shown in Fig. 13.4.b2-b4 (Annexes) because the signal of the shallow slices is saturated (Annexes, Fig. 5.13.b2) and the background noise equally enhanced. Another solution is using a linear increase (Annexes, Fig. 5.13.d2-d4). In this case the first slice is not modified (Annexes, Fig. 5.13.d2) whereas the pixel values of the last

slice was doubled and the intermediate slice one has been enhanced at 150% (multiplied by 1.5). However, it often happens in scanning microscopy that the sample shows a satisfying brightness through the stack except in the deepest slices, and a linear enhancement will then increase too much the signal in intermediate slices (Annexes, Fig. 5.13.d3).

This problem can easily be addressed by an exponential intensity correction with a "growth factor" g strictly superior to 1 (Fig. 5.12.c, light blue and purple curves). The highest is the growth factor the deepest the intensity correction starts. The Fig. 5.13.c2-c4 (Annexes) show the result of an exponential intensity correction with g = 3: the intermediate slice (50th) is enhanced by 12.5% (each pixel multiplied by 1.125) whereas the last one is enhanced at 200% (each pixel multiplied by 2). In the contrary, if only the upper slices do not present a reliable signal intensity, a growth factor inferior to 1 (fig.12.c blue and green curves) can be used to enhance more slices as in Fig. 5.13.e2-e4 (Annexes) and the 50th slice will be enhanced at 175%. However, this case does not occur so often in our samples.

iii. Other features

Among the features proposed in this plugin, we also implemented a gamma correction and a simple thresholding function that sets every voxel under a certain value to zero. The former allows the user to fix the contrast as illustrated in Fig. 5.14 and the latter is an easy way to delete the background (Fig. 5.15).

If the fiber signal also need to be adjusted, normalization, an image processing method that modify the range of pixel intensity values, can be considered. Normalization independently modifies the range of the resulting pixel intensity values of each section of the entire data volume from 0 to 255, 65,535 or 4,294,967,295 (for 8-, 16- and 32-bit data, respectively) by converting the current intensity minimum and maximum of the section (respectively Imin and Imax) to 0 and 2bit depth – 1 according to the (linear) formula:

$$lnew = \frac{(lorignal - lmin) * 2\ (bit\ depth - 1)}{lmax - lmin}$$

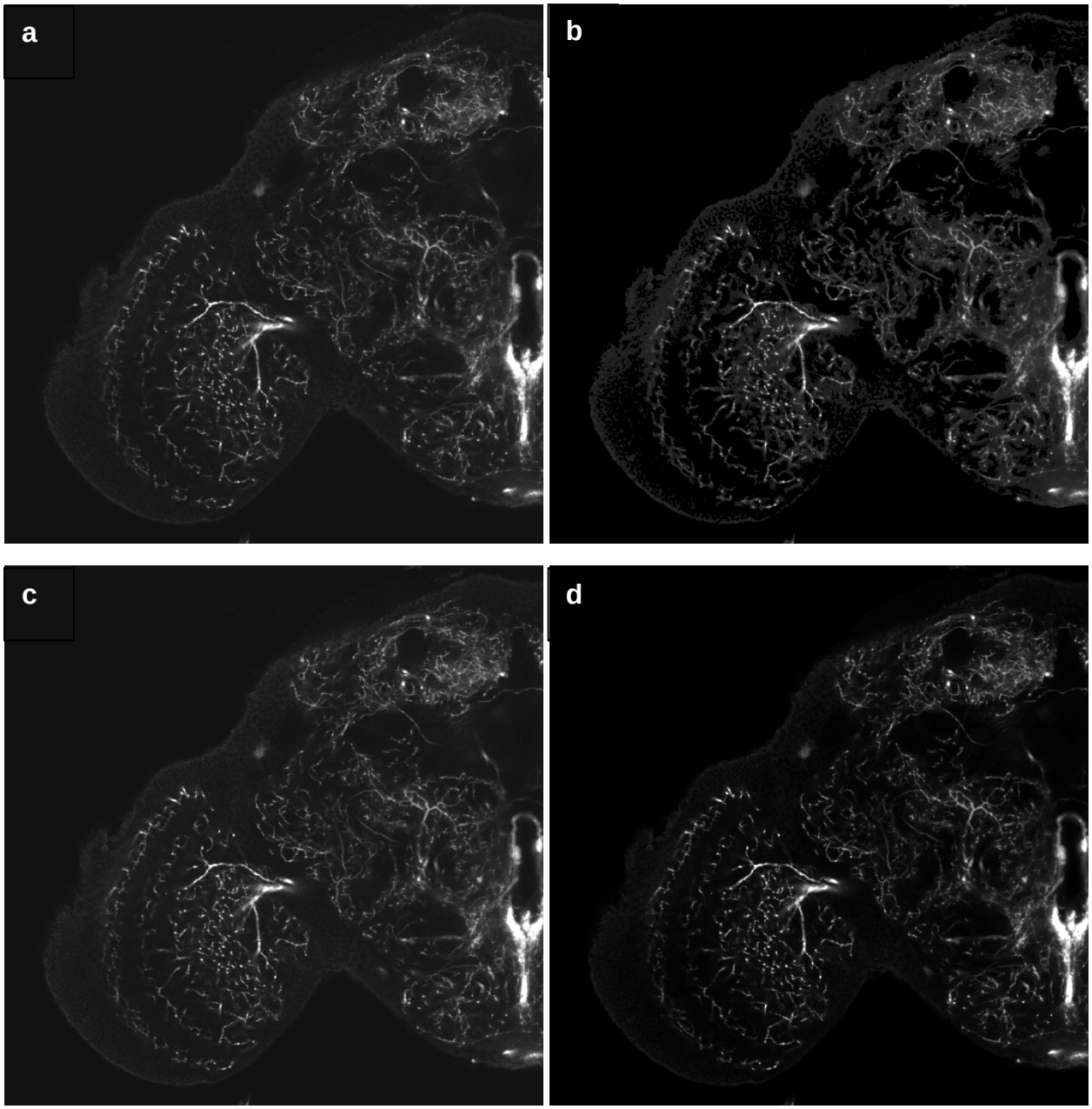

Figure 5.15. Top: Thresholding of an image of the Drosophila Melanogaster brain (the signal intensity was enhanced by 200% before thresholding for better visualization), (a) 200% Enhanced image, (b) Threshold image (pixels inferior to 28 set to 0); Bottom: Normalization of an image of the Drosophila Melanogaster brain (the signal intensity was enhanced by 200% before normalization for better visualization), (c) 200% Enhanced image, (d) Normalized image.

In practice, the normalization can be done for 8, 16 and 32-bit data (bit depth recognized by Fiji). For other bit depths, higher bit depth will be used (16 bits for 12 bit-data, for example). This function can also be used to set the background to zero while enhancing the bright signal to modify the contrast. In the contrary of the thresholding the resulting images appear smoother because all pixel values are modified. However, one should notice that Fiji does not handle 12bits images and the use of the normalization must be applied with caution.

b. RESULTS ON A REAL IMAGE REGISTRATION

We then tested whether proper intensity/gamma correction would indeed improve the precision of registration. Fig. 5.16 compares the results of overlap extraction for the same pair of substacks with or without intensity/gamma correction. Compared to the original substack (Fig. 5.16.a), intensity was corrected between 100% and 300% linearly and gamma between 1.0 and 1.4 linearly from the first (shallowest) to the last (deepest) sections of substacks (Fig. 5.16.b). At the first step of 3D SIFT Volume Stitching, the last slice of the front substack is compared with all the slices of the back substack to compute the number of matching features. The more two slices are similar the greater is the number of matching features. Fig. 5.16.c shows that, in case of the registration after intensity/gamma correction (magenta line), the number of matching features is not only much higher but also the transition is much sharper compared to the registration using original data (green line). Indeed, feature-matching curve of the original data presents a plateau, making the overlap size determination confusing, whereas that of the corrected data shows a sharp peak from which we can precisely deduce the overlap size. This difference can be noticed as a slight shift along the z-axis when the front and back substacks are merged. In the cross section view of the stack (Fig. 5.16.d&e), we can see that the superposition works better (white color without green or magenta fringe) for the intensity-corrected data (Fig. 5.16.e) than for the original data (arrows in Fig. 5.16.d). In many other cases, we have successfully obtained higher number of matching features and smoother and sharper transition curves by adjusting intensity and gamma, leading to more accurate registration.

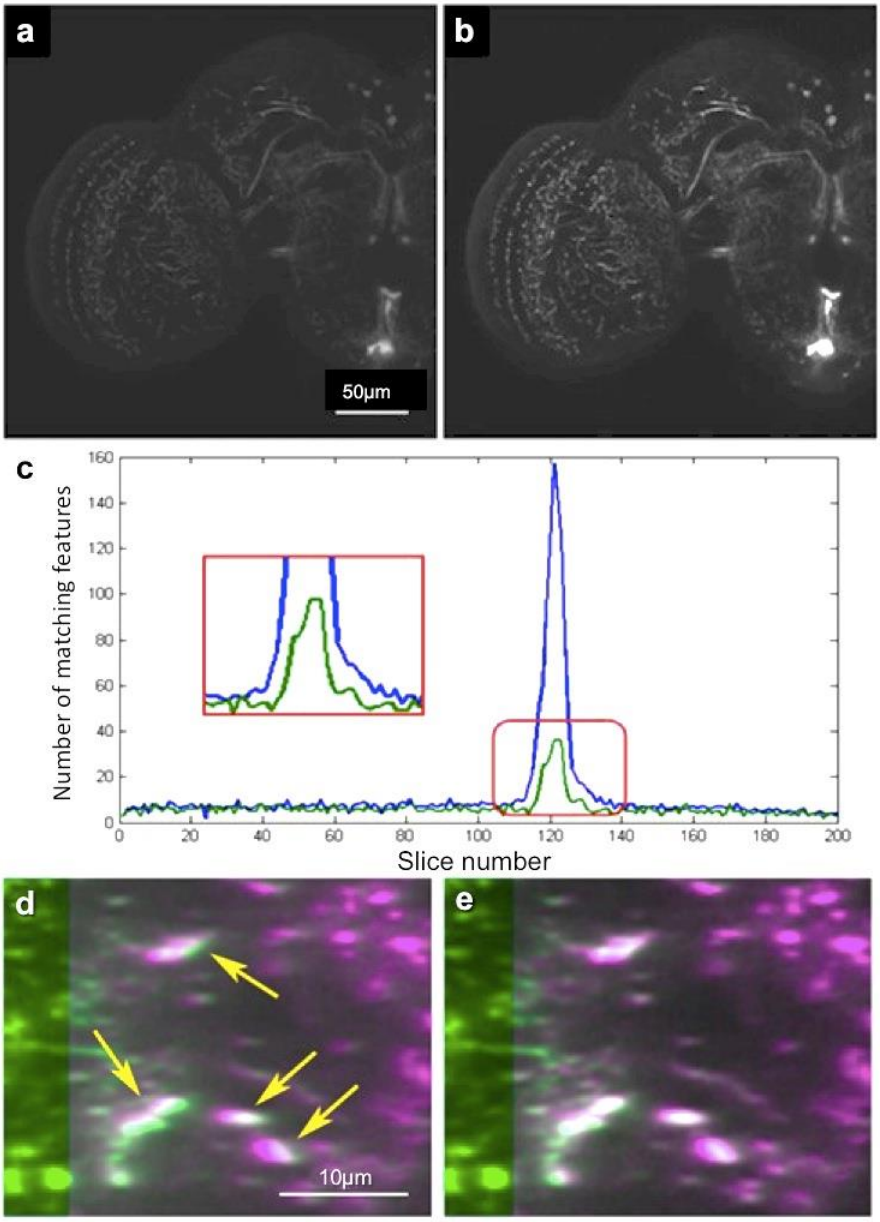

Figure 5.16. Improved registration after intensity and gamma correction, (a) Original data, (b) Corrected data (Intensity 100% to 300% linear, gamma 1 to 1.4 linear), (c) Number of SIFT features in overlap detection for original data (green) and intensity/gamma corrected data (blue). Rectangle shows the plateau of the matching peak without intensity and gamma correction, (d, e) The x-z cross sections of the stack, showing superposition of the front (green, left side of the panels) and back substack images (magenta, right side of the panels). Registration on original data (d) and corrected data (e). Brightness is enhanced for better visualization. Arrows in (d) indicate purple and magenta fringe caused by the mismatch between the front and back substacks, which are hardly seen in (e).

It is important to note that Progressive Intensity and Gamma Correction is not only useful for improving registration accuracy but also useful for matching the appearance of the sections of the two substacks to enable smooth blending of the two. It is useful even for the image stacks that are not meant for stitching, because it can flexibly compensate for the decreasing brightness and contrast in the deep sections of thick volume data.

c. APPLICATION TO OTHER TYPES OF DATASETS

Application of 3D-SIFT technique is not limited to the neuron images of front and back substacks; it can be used on a variety of different datasets that require precise registration. Here we show another example to stitch two stacks of volume data that are aligned side by side instead of top to bottom (Fig. 5.17). Such application is called tiling and often used for obtaining high-resolution image data of the sample that is larger than the imaging field of the objective lens. Stitching should be straightforward if the samples are moved completely in parallel. However, tiny rotation may occur because of mechanical error of the microscope stage, making perfect stitching difficult. 3D-SIFT can cope with such errors and can easily stitch volume image tiles precisely. Note that SIFT-based feature matching is robust against the appearance of images: it works completely well with non-neuronal images that have more continuous appearance and few fiber-like structures compared to the images of neuronal fibers shown in previous figures.

3. APPLICATION

Using this registration technique, we were able to image more than 50 brains of Drosophila melanogaster to visualize octopaminergic and dopaminergic neurons as well as their pre-synaptic site at very high resolution. Therefore, this tools can be used to extensively study object of very complex structures such as neural fibers overcoming the problem of decrease of quality within depth of confocal microscopy.

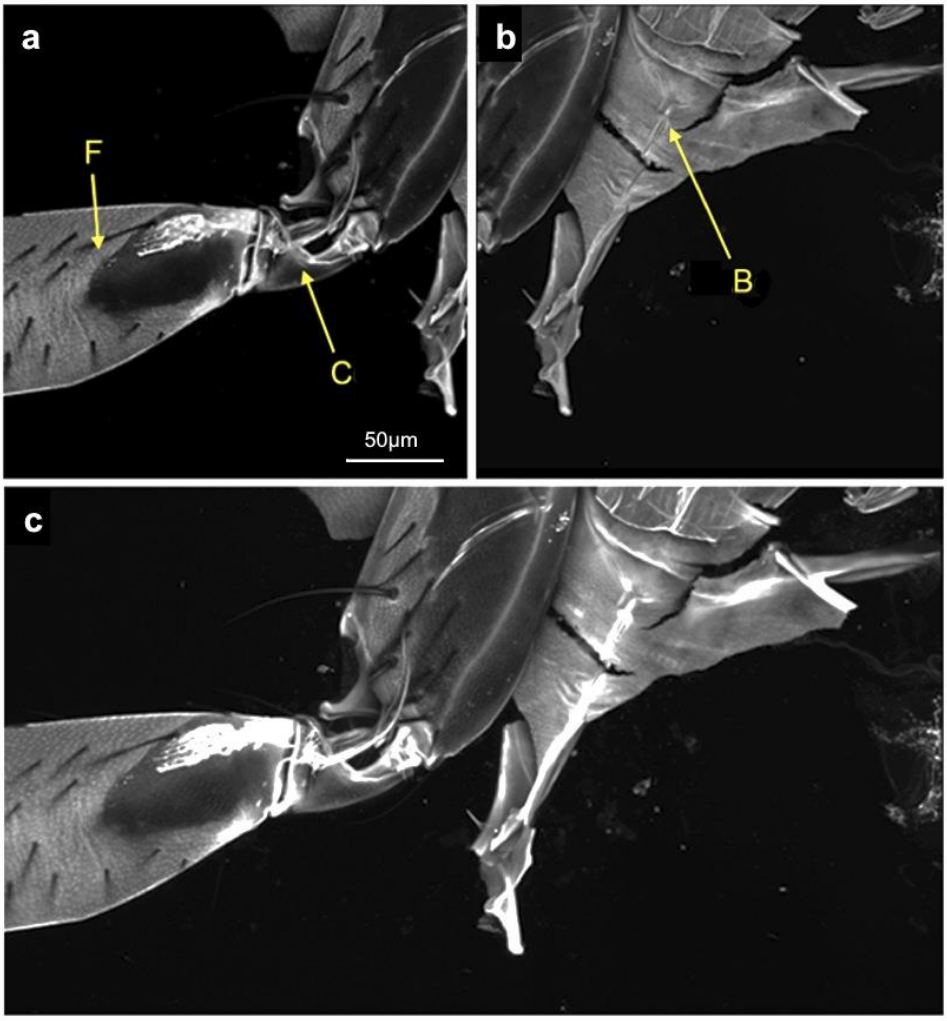

Figure 5.17. Tiling registration of two substacks recorded side-by side. 3D reconstructed images of the base of a *Drosophila* leg. (a) An image stack showing the middle (femur, F) and base (coxa, C) part of the leg. (b) Base of the leg and a part of the body (B). (c) Registered image. Scale bar = 50 µm.

We were then able to globally study those complicated neuron branches as a complete network, exchanging information with other types of neurons, and not to focus on single neurons. However, computationally handling such heavy data remains challenging. We were still able to show a certain plasticity of the brain not only over time but also upon activation. This reorganization does not equally affect octopaminergic and dopaminergic neurons and a variety of responses has to be expected from other types of neurons.

4. CONCLUSION

With the advances of research in biological fields, understanding the global organization of a system has become a key point for further discovery. Getting a more global view of the system leads to the necessity of data acquisition of thicker volumes, whose must be processed by appropriate tools. The 3D-SIFT is an efficient method for registration and stitching of a variety of big 3D image stacks. It allows tight adjustment of stacks of thin structures such as neurons to avoid seams between stitched substacks, or tiles, reducing errors in further 3D image analyses. Moreover, since the comparison is done between specific stable locations of the image stacks, registration between big volume data can be performed more quickly than in the case of voxel-to-voxel comparison methods. 3D-SIFT is therefore an efficient tool not only for stitching tilted substacks but also for stitching horizontally-aligned tiles of volume stacks and registration of large substacks that has no tilting. Our study also gives clues on the way of evaluating the quality of new data processing method by the creation of a set of in silico test data that simulate the noise in laser scanning microscopy. In parallel we also developed tools that aim to improve intensity and contrast of serial section image stacks to compensate the loss induced by laser scanning image acquisition. Those tools, available on Fiji and ImageJ, should help advanced analyses of big volume data.

Using those tools, we were able to image a large number of very high quality samples of dopaminergic and octopaminergic neurons of the fruit fly brain. We could show differences between those neurons evolution under various condition. Octopaminergic neurons seem to be more stable, less subject to the effect of time or inactivation than dopaminergic neurons that seem to be fragile and degenerate quickly after inactivation but also, at a slower pace, within time. However, unlike octopaminergic neurons, dopaminergic neurons are crucial for Drosophila melanogaster, who cannot survive more than a few days to their inactivation. This suggest that the function of these neurons cannot be ensure by any other type of neurons. Octopaminergic neurons appear to be less essential to the fruit fly (the fly survives) but flies lacking those neurons

present an abnormal behavior proving that the octopaminergic neurons inactivation affects the brain.

PART 6 ACKNOWLEDGMENTS

I am particularly grateful to my laboratories members, especially my professor, Dr. Kei Ito for his supervision, as well as my labmates for their support.

Thank you to David Rousseau and Carole Frindel for their help and precious advices in image processing and analysis through this whole study.

I am deeply grateful Hanchuan Peng from Allen Institute for Brain Sciences, Henrik Skibbe and Shin Ishii from the University of Kyoto, Hideo Otsuna from Janelia farm for their comments and suggestions through fruitful discussions.

I thank Haruka Hirose, Youko Ishida, Ryoko Tatsumi, Jun Tanimura, Asako Tsubouchi, Satomi Shuto and Tomoko Yano for their technical and scientific assistance.

I also thank Bloomington Drosophila Stock Centre for fly strains and Hybridoma Bank for antibodies. This study is supported by the Strategic Research Program for Brain Sciences and CREST Program by the Japan Science and Technology Agency / Japan Agency for Medical Research and Development to KI.

I finally thank my family for their unconditional support through my whole academic life.

PART 7 REFERENCES

Booth, M. J., Neil, M. A. A., Juškaitis, R., & Wilson, T., (2002) Adaptive aberration correction in a confocal microscope. Applied Physical Sciences, 99(9): 5788–5792, doi:10.1073/pnas.082544799

Brand, A.H., & Perrimon, N. (1993). Targeted gene expression as a means of altering cell fates and generating dominant phenotypes. *Development*, 118(2), 401-15.

Brown, K. M., Barrionuevo, G., Canty, A. J., De Paola, V., Hirsch, J. A., Jefferis, G. S., Lu, J., Snippe, M., Sugihara, I., & Ascoli, G. A., (2011) The DIADEM Data Sets: Representative Light Microscopy Images of Neuronal Morphology to Advance Automation of Digital Reconstructions. *Neuroinformatics*, 9(2-3):143-57, doi: 10.1007/s12021-010-9095-5.

Burke, C.J., Huetteroth, W., Owald, D., Perisse, E., Krashes, M.J., Das, G., Gohl, D., Silies, M., Certel, S., Waddell, S., (2012) Layered reward signalling through octopamine and dopamine in Drosophila *Nature* 492 (7429): 433–7. doi:10.1038/nature11614. PMID 23103875.

Busch, S., Selscho, M., Ito, K., & Tanimoto, H. (2009). A Map of Octopaminergic Neurons in the Drosophila Brain. *J Comp Neurol*, 513(6), 643-67.

Cardona, A., (2013) Towards Semi-Automatic Reconstruction of Neural Circuits. *Neuroinformatics*, 11(1):31-3, doi: 10.1007/s12021-012-9166-x.

Chung, K., Wallace, J., Kim, S. Y., Kalyanasundaram, S., Andalman, A. S., Davidson, T. J., Mirzabekov, J. J., Zalocusky, K. A., Mattis, J., Denisin, A. K., Pak, S.; Bernstein, H., Ramakrishnan, C., Grosenick, L., Gradinaru, V., & Deisseroth, K. (2013). Structural and molecular interrogation of intact biological systems. *Nature* 497 (7449): 332–337. doi:10.1038/nature12107. PMID 23575631

Davidovits, P., & Egger, M. D., (1969). Scanning laser microscope. *Nature* 223 (5208): 831, doi:10.1038/223831a0. PMID 5799022.

Fritzky, L., & Lagunoff, D., (2013) Advanced methods in fluorescence Microscopy. *Anal Cell Pathol*, 36(1-2):5-17, doi: 10.3233/ACP-120071.

Graf, B. W., & Boppart, S. A, (2010) Imaging and Analysis of Three-Dimensional Cell Culture Models. *Methods Mol Biol*, 591: 211–227.

Hama, H., Kurokawa, H., Kawano, H., Ando, R., Shimogori, T., Noda, H., Fukami, K., Sakaue-Sawano, A., & Miyawaki, A.. (2011) Scale: a chemical approach for fluorescence imaging and reconstruction of transparent mouse brain. *Nat Neurosci.* 14(11): 1481-8. doi: 10.1038/nn.2928.

Herberich, G., Windoffer, R., Leube, R.E., & Aach, T. (2012). Signal and Noise Modeling in Confocal Laser Scanning Fluorescence Microscopy. *Med Image Comput Comput Assist Interv*, 15(1), 381-8.

Ito, K., Okada, R., Tanaka, N. K., & Awasaki, T., (2003) Cautionary observations on preparing and inter-preting brain images using molecular biology-based staining techniques. Microsc Res Tech, 62, 170-86

Ito, K., Shinomiya, K., Ito, M., Armstrong, D., Boyan, G., Hartenstein, V., Harzsch, S., Heisenberg, M., Homberg, U., Jenett, A., Keshishian, H., Restifo, L., Rössler, W., Simpson, J., Strausfeld, N. J., Strauss, R., & Vosshall, L.B., (2014) The Insect Brain Name Working Group. A systematic nomenclature for the insect brain. *Neuron*, 81, 755-765

James, J.L., Hodge, (2009) Ion Channels to Inactivate Neurons in Drosophila, Front Mol Neurosci. 2: 13. doi: 10.3389/neuro.02.013.2009, PMCID: PMC2741205

Jefferis, G. S., & Livet J., (2012) Sparse and combinatorial neuron labelling. *Curr Opin Neurobiol*, 101-10, doi: 10.1016/j.conb.2011.09.010

Li, C. H., & Lee C. K., (1993) Minimum cross entropy thresholding. *Pattern Recognition*. Volume 26, Issue 4, Pages 617–625, doi:10.1016/0031-3203(93)90115-D

Li, J., & Allinson, N. M. (2008). A comprehensive review of current local features for computer vision. *Neurocomputing*, 71(10), 1771-1787

Liu, C., Plaçais, P.Y., Yamagata, N., Pfeiffer, B., Aso, Y., Friedrich, A.B., Siwanowicz, I., Rubin, G.M., Preat, T., Tanimoto, H. (2012) A subset of dopamine neurons signals reward for odour memory in Drosophila. *Nature* 488 (7412): 512–6. doi:10.1038/nature11304. PMID 22810589

Lindeberg, T., (1998) Feature detection with automatic scale selection. *International Journal of Computer Vision*, 30(2):79–116.

Lowe, D.G. (1999). Object recognition from local scale-invariant features. *Proc. of the International Conference on Computer Vision*.

Lowe, D.G. (2004). Distinctive Image Features from Scale-Invariant Keypoints. *International Journal of Computer Vision*, 60(2), 91-110.

McGuire, S.E., Mao, Z., Davis, R.L., (2004) Spatiotemporal gene expression targeting with the TARGET and gene-switch systems in Drosophila. Feb 12;2004(220):pl6.

Meijering, E., (2010) Neuron tracing in perspective. *Cytometry A*, 77(7):693-704, doi: 10.1002/cyto.a.20895.

Mikolajczyk, K., (2002) Interest point detection invariant to affine transformations. PhD thesis, Institut National Polytechnique de Grenoble.

Peng, H., Chung, P., Long, F., Qu, L., Jenett, A., Seeds, A. M., Myers, E. W., & Simpson, J. H., (2011) BrainAligner: 3D registration atlases of Drosophila brains. *Nature Methods* 8, 493–498, doi:10.1038/nmeth.1602

Preibisch, S., Saalfeldand, S., & Tomancak, P. (2009). Globally optimal stitching of tiled 3D microscopic image acquisitions. *Bioinformatics*, 25(11), 1463–1465.

Ragan, T., Kadiri, L. R., Venkataraju, K. U., Bahlmann, K., Sutin, J., Taranda, J., Arganda-Carreras, I., Kim, Y., Seung., H. S., & Osten P., (2012) Serial two-photon tomography for automated ex vivo mouse brain imaging. Nat Methods, 15;9(3):255-8, doi: 10.1038/nmeth.1854

Rameshy, N., Otsuna, H., & Tasdizen, T. (2013). Three-Dimensional alignment and merging of confocal microscopy stacks. *20th IEEE International Conference on Image Processing*, 1447 - 1450.

Rohlfing, T., (2011) User Guide to The Computational Morphometry Toolkit. Neuroscience Program, SRI International, Menlo Park, CA

Scovanner, P., Ali, S., & Shah, M., (2007) A 3-dimensional sift descriptor and its application to action recognition. *Proceedings of the 15th international conference on Multimedia*, doi: 10.1145/1291233.1291311

Sheppard, C., (1991) Aberration compensation in confocal microscopy. *Applied Optics*, 30(25):3563-8. doi: 10.1364/AO.30.003563

Shih, C. T., Sporns, O, Yuan, SL, Su, TS, Lin, YJ, Chuang, CC, Wang, TY, Lo, C. C., Greenspan, R. J., Chiang, A. S., (2015) Connectomics-based analysis of information flow in the Drosophila brain. Curr Biol, 18;25(10):1249-58, doi: 10.1016/j.cub.2015.03.021.

Takemura, S. Y., Bharioke, A., Lu, Z., Nern, A., Vitaladevuni, S., Rivlin, P. K., Katz, W. T., Olbris, D. J., Plaza, S. M., Winston, P., Zhao, T., Horne, J. A., Fetter, R. D., Takemura, S., Blazek, K., Chang, L. A., Ogundeyi, O., Saunders, M. A., Shapiro, V., Sigmund, C., Rubin, G. M., Scheffer, L. K., Meinertzhagen, I. A., Chklovskii, D. B., (2013) A visual motion detection circuit suggested by Drosophila connectomics. Nature. 8;500(7461):175-81. doi: 10.1038/nature12450.

White, K.E., Humphrey, D.M., & Hirth, F. (2010). The dopaminergic system in the aging brain of Drosophila. *Front Neurosci*. doi:10.3389/fnins.2010.00205

Zheng, T., Yang, Z., Li, A., Lv, X., Zhou, Z., Wang, X., Qi, X., Li, S., Luo, Q., Gong, H., & Zeng, S., (2013) Visualization of brain circuits using two-photon fluorescence micro-optical sectioning tomography. *Opt Express*, 21(8):9839-50, doi: 10.1364/OE.21.009839

PART 8 PUBLICATIONS

International journal article

Image processing for precise three-dimensional registration and stitching of thick high-resolution laser-scanning microscopy image stacks Chloé MURTIN, David ROUSSEAU, Carole FRINDEL, Kei ITO, Neuroinformatics (under revision).

International conferences

Image Registration for Confocal Fluorescence Microscopy 3-Dimensional Stack of Images of Drosophila Melanogaster Central Nervous System. Chloé MURTIN, Carole FRINDEL, David ROUSSEAU, and Kei ITO. In 11th International Congress of Neuroethology (ICN), Sapporo, Japon. August, 2014.

National conference

Multipleview image registration based on landmarks without fluorescence beads in 3D light sheet microscopy; Gilda COSTANTINO, Chloé MURTIN, Carole FRINDEL, Charlotte RIVIERE, Tess HOMAN, Ito KEI, David ROUSSEAU. First French Light Sheet Microscopy conference 5-6 April 2016.

Three-dimensional image analysis of high resolution confocal microscopy data of the drosophila melanogaster brain. Chloé MURTIN, Carole FRINDEL, David ROUSSEAU, Ito KEI. Journée Traitement du signal et des images pour la biologie, GdR CNRS ISIS, 8 juin 2016.

ANNEXES

Table 2.1. Example of crossing

a. ♂♂ yw UAS-Syt::HA UAS-DsRed; +/+; LexAop-rCD2::GFP/TM6 Sb Tb

♂♂		Gonosome	Second chromosome	Third chromosome
	X	yw UAS-Syt::HA UAS-DsRed	+	LexAop-rCD2::GFP
	Y	Y	+	TM6 Sb Tb

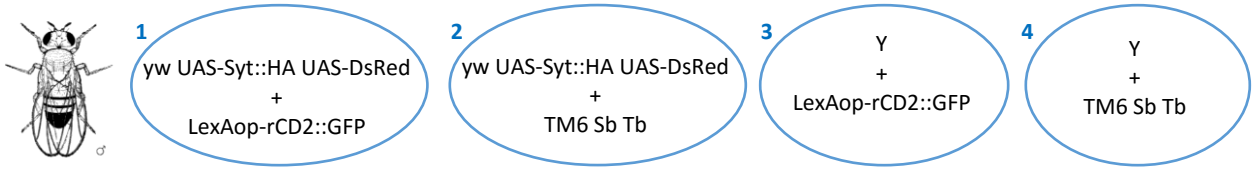

b. ♀♀ w; Tdc2-GAL4/CyO; TH-LexA/TM3 Ser

♀♀		Gonosome	Second chromosome	Third chromosome
	X	w	Tdc2-GAL4	TH-LexA
	X	w	CyO	TM3 Ser

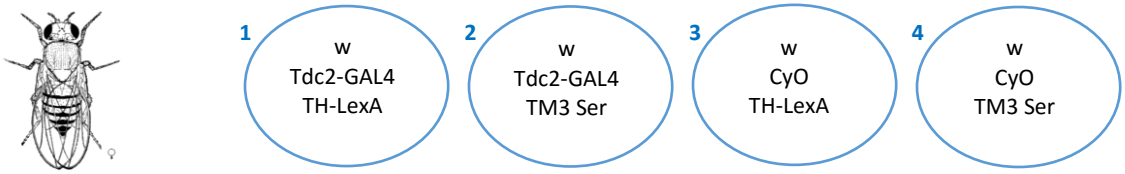

c. Crossing

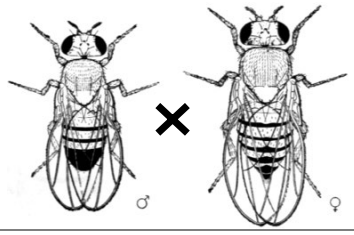

Crossing	Genotype	Phenotype	Gene of interest
♂ 1x ♀1	yw UAS-Syt::HA UAS-DsRed/w +/ Tdc2-GAL4 LexAop-rCD2::GFP/TH-LexA	Female Red eyes Straight wings Merged wings Long bristles Normal body size	UAS-Syt::HA UAS-DsRed Tdc2-GAL4 LexAop-rCD2::GFP TH-LexA
♂ 1x ♀2	yw UAS-Syt::HA UAS-DsRed/w +/ Tdc2-GAL4 LexAop-rCD2::GFP/TM3 Ser	Female White eyes Straight wings Notched wings Long bristles Normal body size	UAS-Syt::HA UAS-DsRed Tdc2-GAL4 LexAop-rCD2::GFP TH-LexA
♂ 1x ♀3	yw UAS-Syt::HA UAS-DsRed/w +/ CyO	Female Red eyes	UAS-Syt::HA UAS-DsRed Tdc2-GAL4

	LexAop-rCD2::GFP/TH-LexA	Curved wings Merged wings Long bristles Normal body size	LexAop-rCD2::GFP TH-LexA
♂ 1x ♀4	yw UAS-Syt::HA UAS-DsRed/w +/ CyO LexAop-rCD2::GFP/TM3 Ser	Female Red eyes Curved wings Notched wings Long bristles Normal body size	UAS-Syt::HA UAS-DsRed Tdc2-GAL4 LexAop-rCD2::GFP TH-LexA
♂ 2x ♀1	yw UAS-Syt::HA UAS-DsRed/w +/ Tdc2-GAL4 TM6 Sb Tb/ TH-LexA	Female Red eyes Straight wings Merged wings Short and stubby bristles Short body	UAS-Syt::HA UAS-DsRed Tdc2-GAL4 LexAop-rCD2::GFP TH-LexA
♂ 2x ♀2	yw UAS-Syt::HA UAS-DsRed/w +/ Tdc2-GAL4 TM6 Sb Tb/ TM3 Ser	Female Red eyes Straight wings Notched wings Short and stubby bristles Short body	UAS-Syt::HA UAS-DsRed Tdc2-GAL4 LexAop-rCD2::GFP TH-LexA
♂ 2x ♀3	yw UAS-Syt::HA UAS-DsRed/w +/CyO TM6 Sb Tb/ TH-LexA	Female Red eyes Curved wings Merged wings Short and stubby bristles Short body	UAS-Syt::HA UAS-DsRed Tdc2-GAL4 LexAop-rCD2::GFP TH-LexA
♂ 2x ♀4	yw UAS-Syt::HA UAS-DsRed/w +/CyO TM6 Sb Tb/ TM3 Ser	Female Red eyes Curved wings Notched wings Short and stubby bristles Short body	UAS-Syt::HA UAS-DsRed Tdc2-GAL4 LexAop-rCD2::GFP TH-LexA
♂ 3x ♀1	Y/w +/ Tdc2-GAL4 LexAop-rCD2::GFP/TH-LexA	Male Red eyes Straight wings Merged wings Long bristles Normal body size	UAS-Syt::HA UAS-DsRed Tdc2-GAL4 LexAop-rCD2::GFP TH-LexA
♂ 3x ♀2	Y/w +/ Tdc2-GAL4 LexAop-rCD2::GFP/TM3 Ser	Male Red eyes Straight wings Notched wings Long bristles Normal body size	UAS-Syt::HA UAS-DsRed Tdc2-GAL4 LexAop-rCD2::GFP TH-LexA
♂ 3x ♀3	Y/w +/ CyO LexAop-rCD2::GFP/TH-LexA	Male white eyes Curved wings Merged wings Long bristles Normal body size	UAS-Syt::HA UAS-DsRed Tdc2-GAL4 LexAop-rCD2::GFP TH-LexA

♂ 3x ♀4	Y/w +/ CyO LexAop-rCD2::GFP/TM3 Ser	Male White eyes Curved wings Notched wings Long bristles Normal body size	UAS-Syt::HA UAS-DsRed Tdc2-GAL4 LexAop-rCD2::GFP TH-LexA
♂ 4x ♀1	Y/w +/ Tdc2-GAL4 TM6 Sb Tb /TH-LexA	Male Red eyes Straight wings Merged wings Short and stubby bristles Short body	UAS-Syt::HA UAS-DsRed Tdc2-GAL4 LexAop-rCD2::GFP TH-LexA
♂ 4x ♀2	Y/w +/ Tdc2-GAL4 TM6 Sb Tb /TM3 Ser	Male Red eyes Straight wings Notched wings Short and stubby bristles Short body	UAS-Syt::HA UAS-DsRed Tdc2-GAL4 LexAop-rCD2::GFP TH-LexA
♂ 4x ♀3	Y/w +/ CyO TM6 Sb Tb /TH-LexA	Male White eyes Curved wings Merged wings Short and stubby bristles Short body	UAS-Syt::HA UAS-DsRed Tdc2-GAL4 LexAop-rCD2::GFP TH-LexA
♂ 4x ♀4	Y/w +/ CyO TM6 Sb Tb /TM3 Ser	Male White eyes Curved wings Notched wings Short and stubby bristles Short body	UAS-Syt::HA UAS-DsRed Tdc2-GAL4 LexAop-rCD2::GFP TH-LexA

d. Gene nomenclature:

Gene	Complete name	Chromosome	Phenotype
+	Wild type	-	-
Cyo		2nd	Curved wings
Ser	Serrate	3rd	Notched wings
Sb	Stubble	3rd	Short and stubby bristles
Tb	Tubby	3rd	Short body (size)
TM3			Balancer
TM6			Balancer
w	white	X	White eye color
y	yellow	X	Light brown body color

a. 5 day old flies

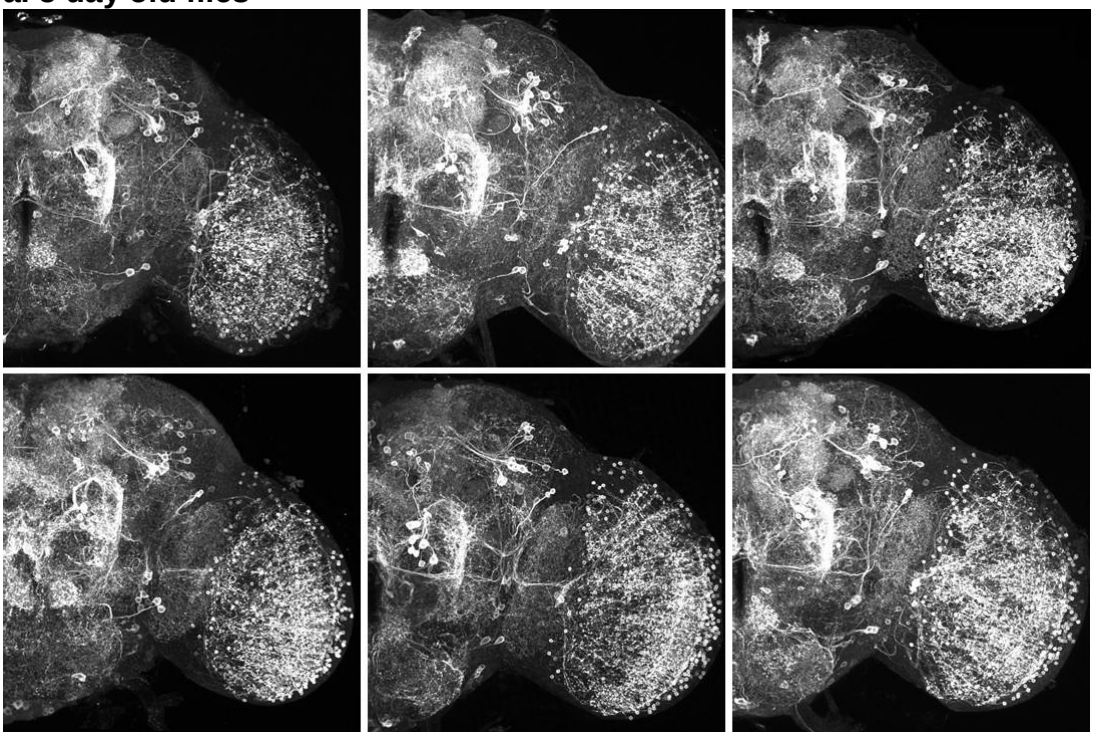

b. 30 day old flies

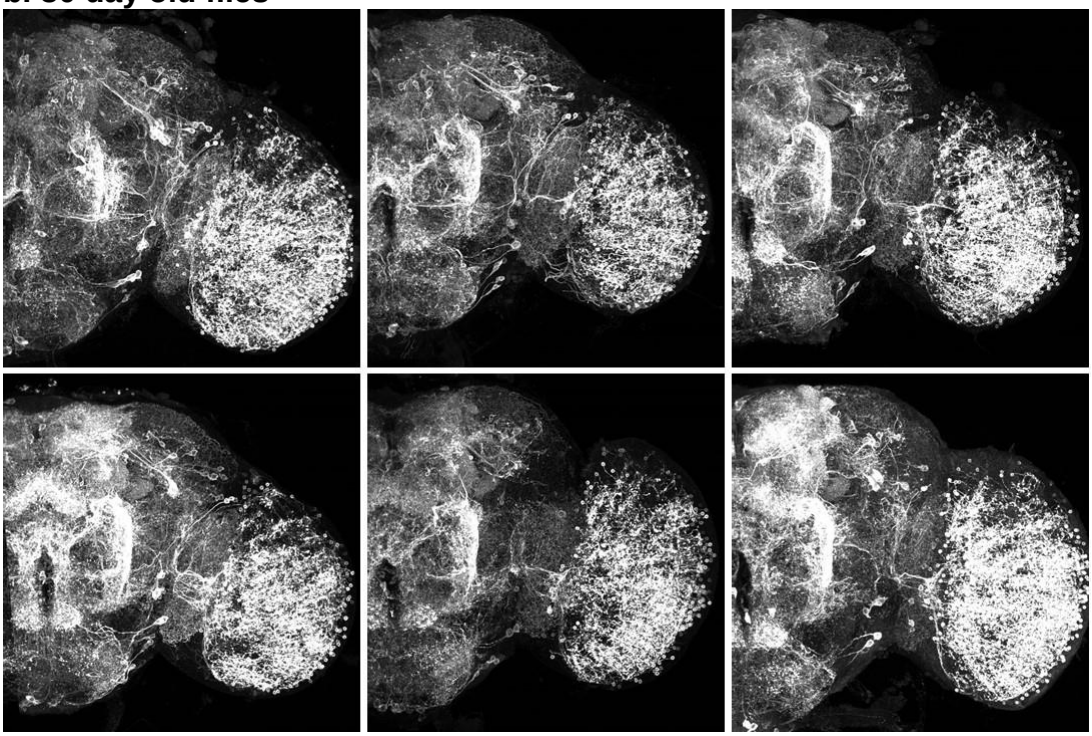

Figure 4.27. Comparison of dopaminergic neurons of Drosophila melanogaster (experiment 1, genotype 1) for, (a) 5 day old flies (young) and, (b) 30 day old flies (old).

a. 5 day old flies

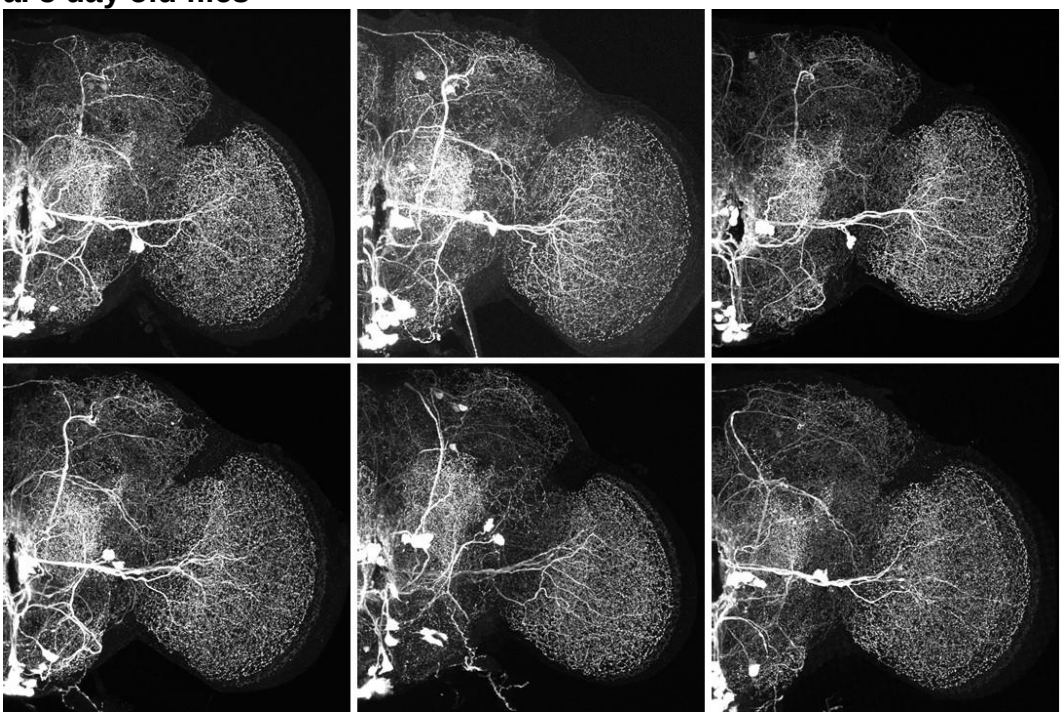

b. 30 day old flies

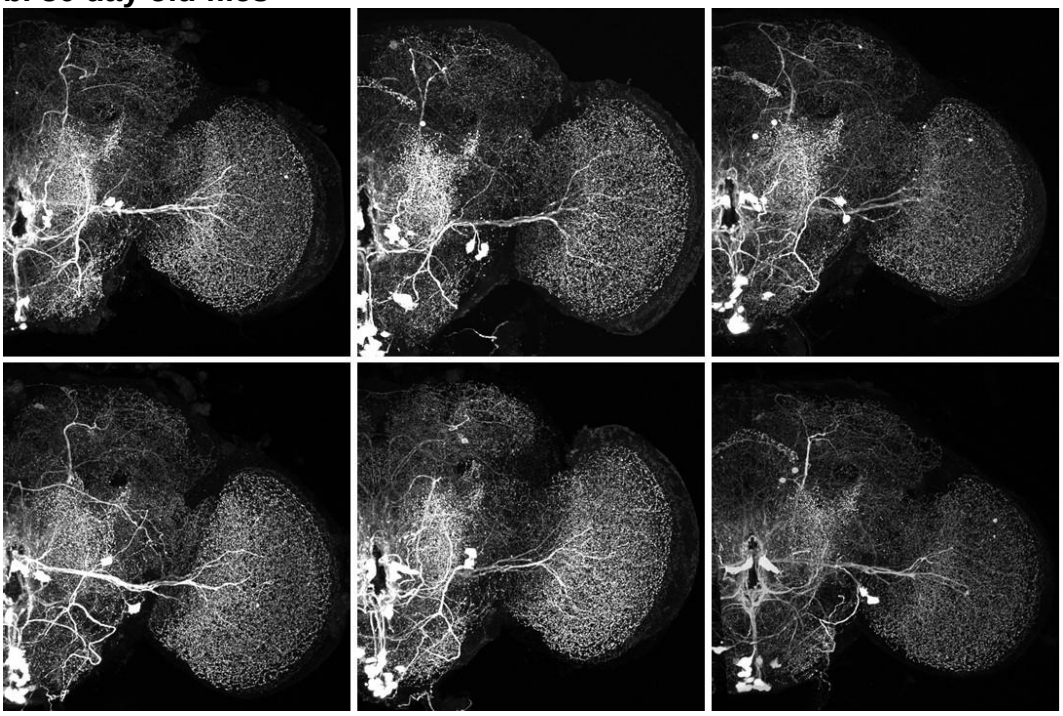

Figure 4.28. Comparison of octopaminergic neurons of Drosophila melanogaster (experiment 1, genotype 1) for, (a) 5 day old flies (young) and, (b) 30 day old flies (old).

a. 5 day old flies

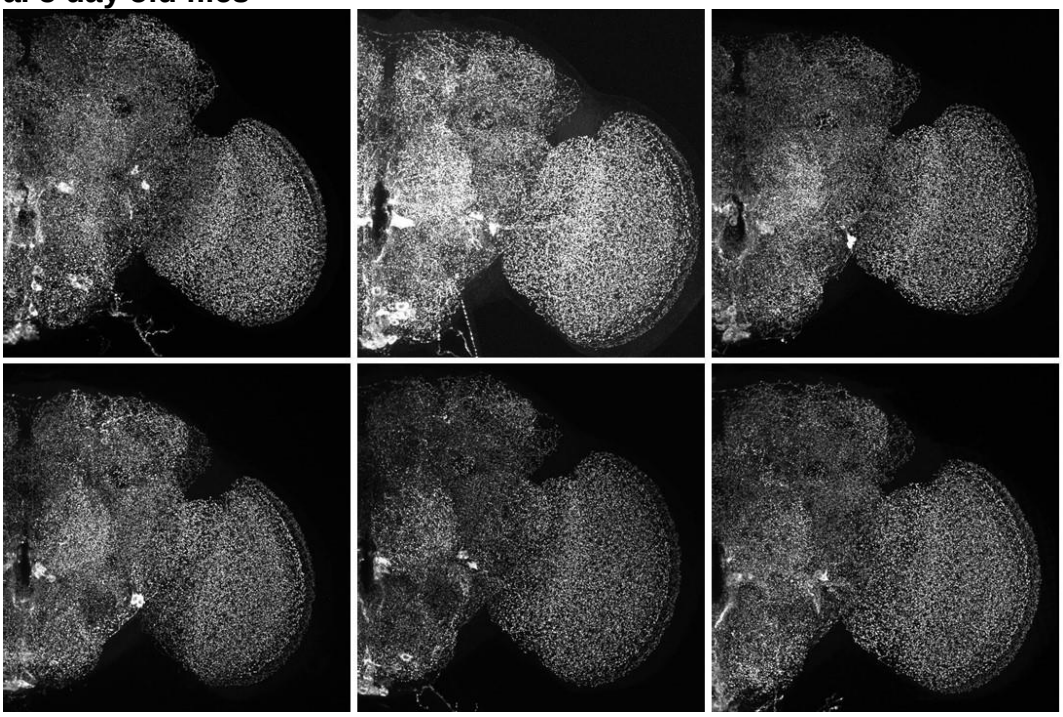

b. 30 day old flies

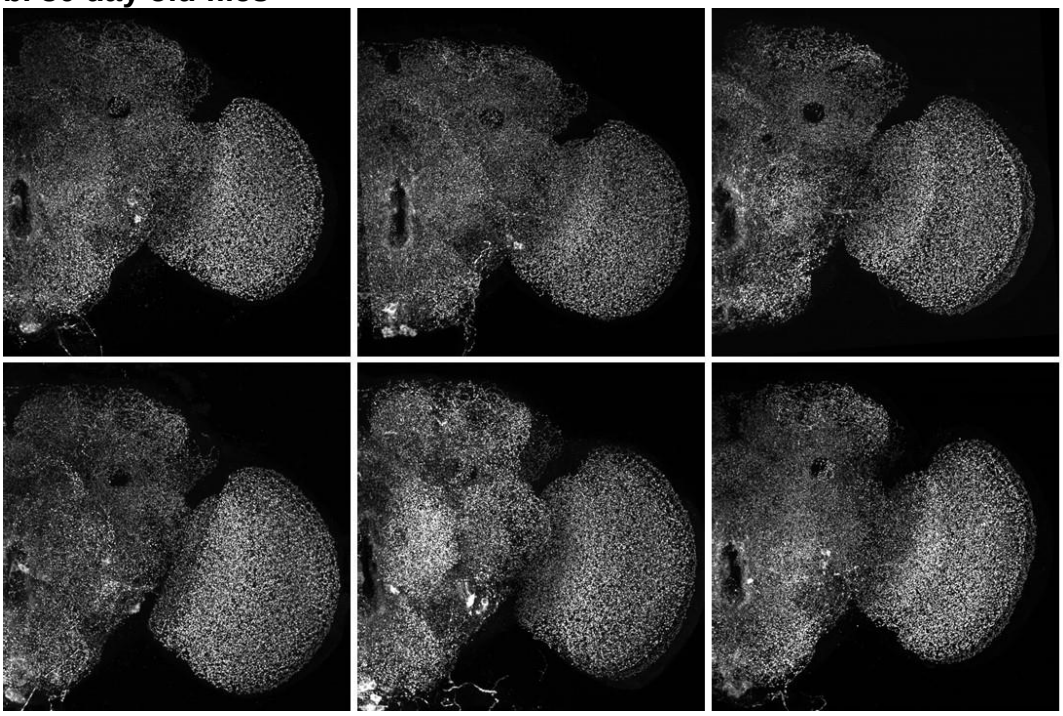

Figure 4.29. Comparison of pre-synaptique sites of octopaminergic neurons of Drosophila melanogaster (experiment 1, genotype 1) for, (a) 5 day old flies (young) and, (b) 30 day old flies (old).

a. 5 day old flies

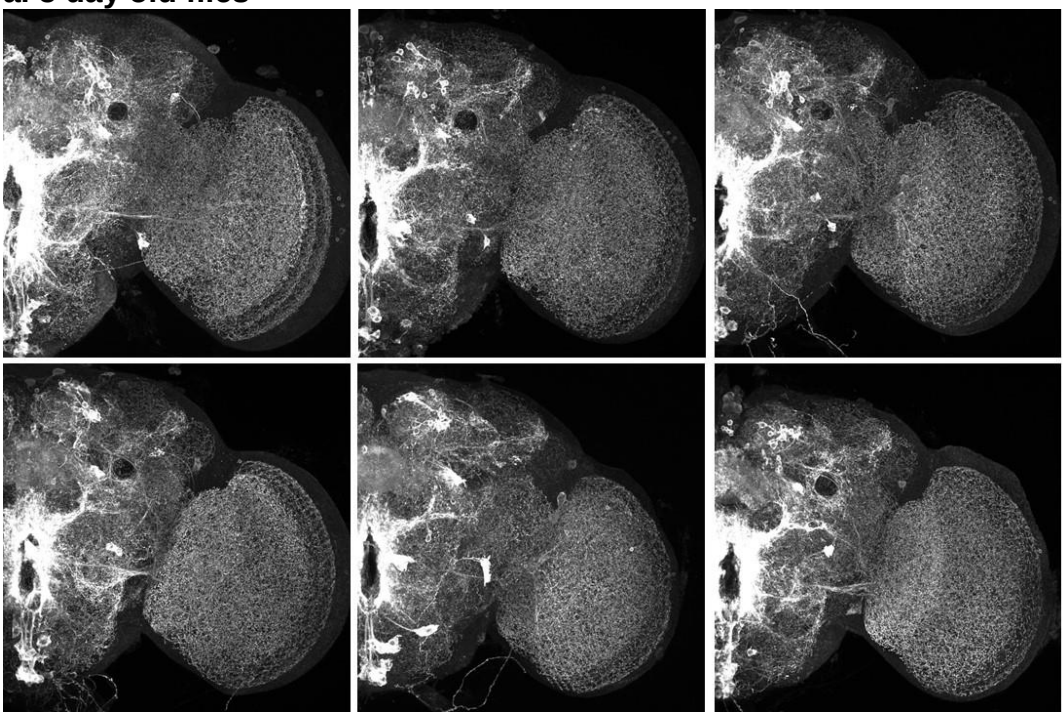

b. 30 day old flies

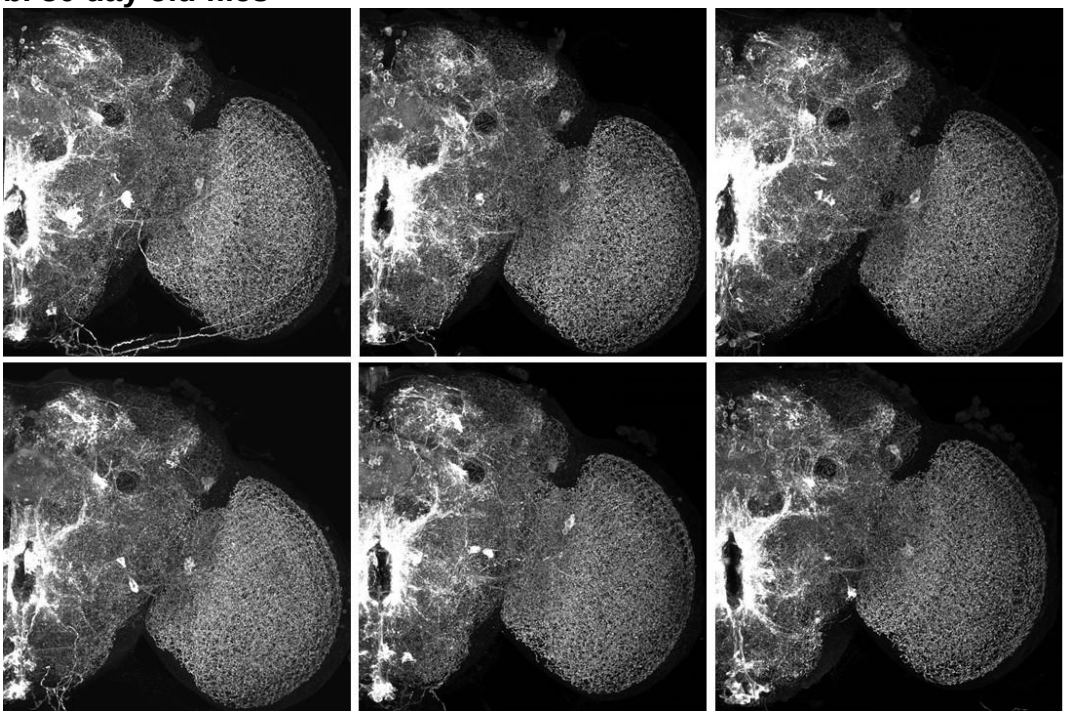

Figure 4.30. Comparison of octopaminergic neurons of Drosophila melanogaster (experiment 1, genotype 2) for, (a) 5 day old flies (young) and, (b) 30 day old flies (old).

a. 5 day old flies

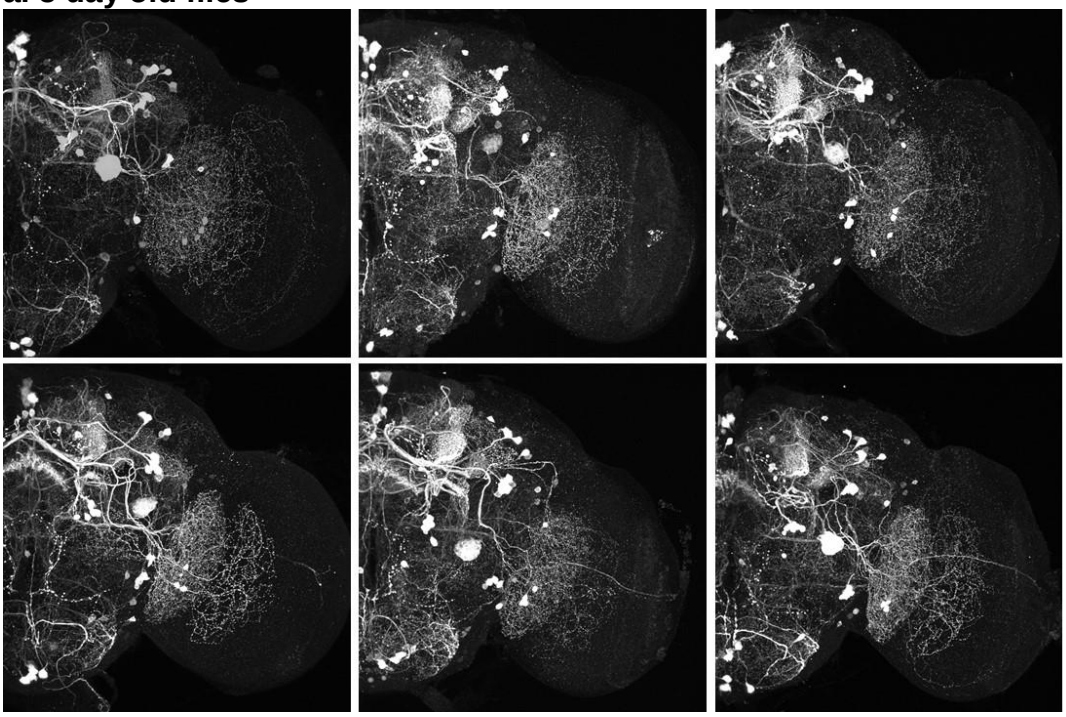

b. 30 day old flies

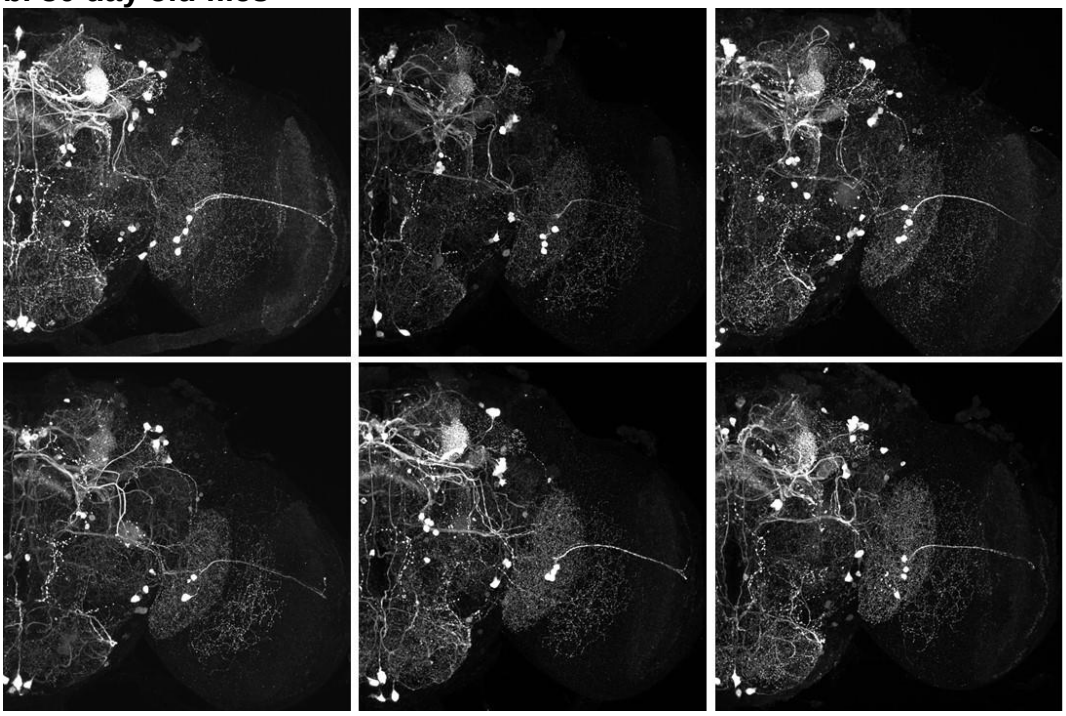

Figure 4.31. Comparison of dopaminergic neurons of Drosophila melanogaster (experiment 1, genotype 2) for, (a) 5 day old flies (young) and, (b) 30 day old flies (old).

a. 5 day old flies

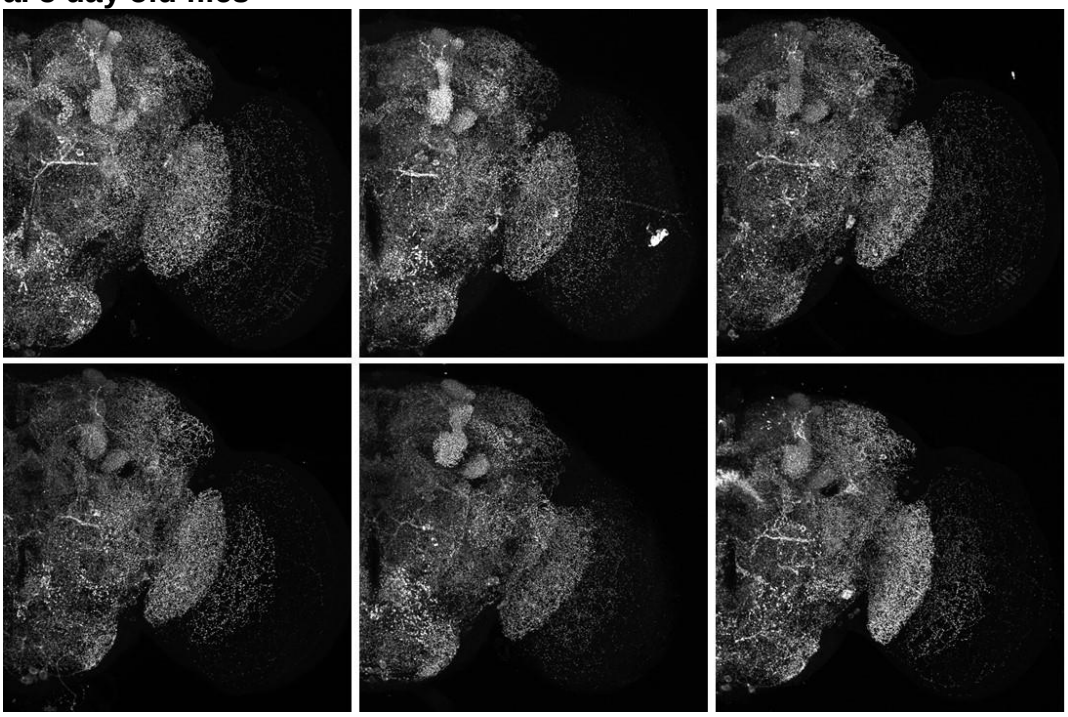

b. 30 day old flies

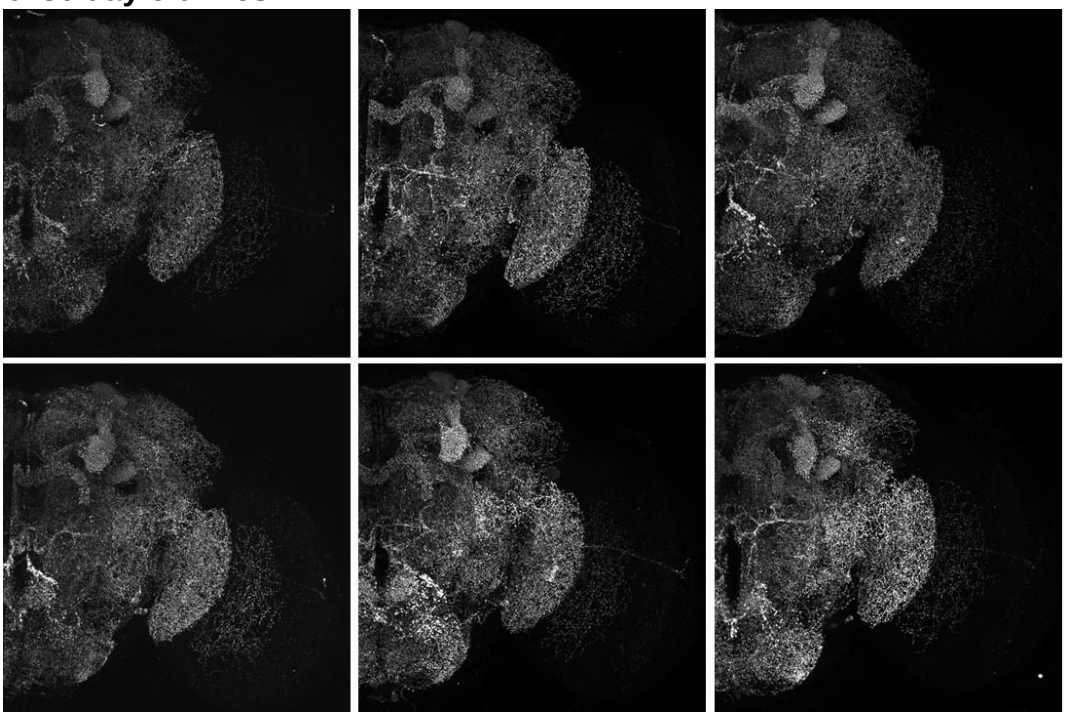

Figure 4.32. Comparison of pre-synaptique sites of octopaminergic neurons of Drosophila melanogaster (experiment 1, genotype 1) for, (a) 5 day old flies (young) and, (b) 30 day old flies (old).

a. Control

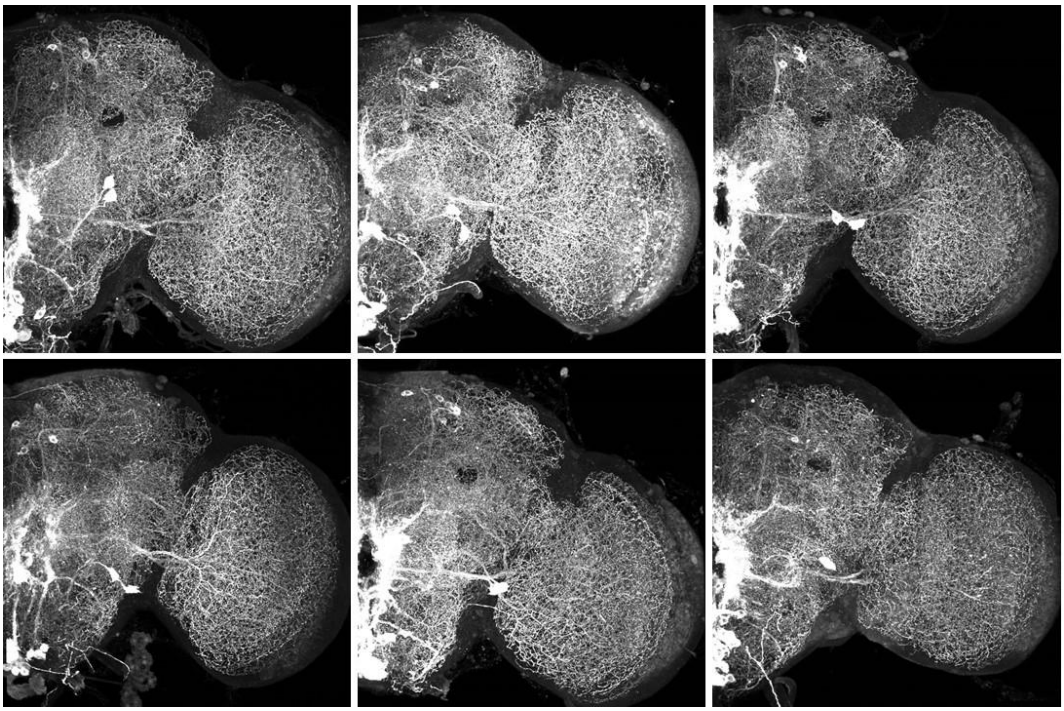

b. Kir2.1

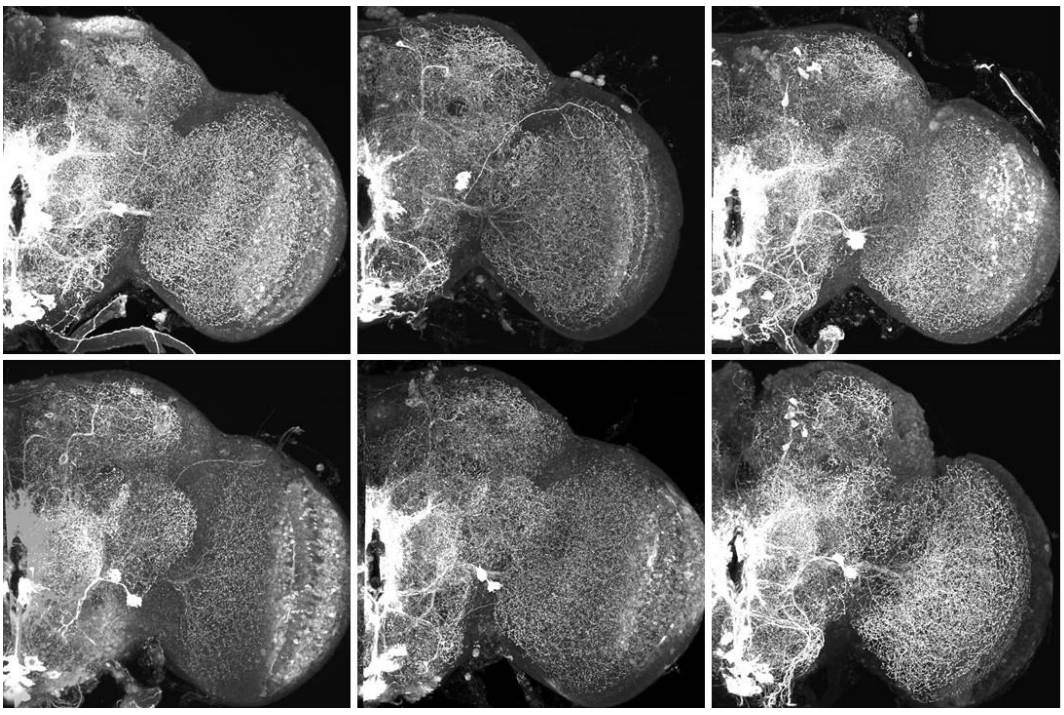

Figure 4.33. Comparison of octopaminergic neurons of 5 day old Drosophila melanogaster (experiment 2) for, (a) control (wild type, genotype 1.2 and, (b) kir2.1 (overexpressing of potassium channel, genotype 1.1).

a. Control

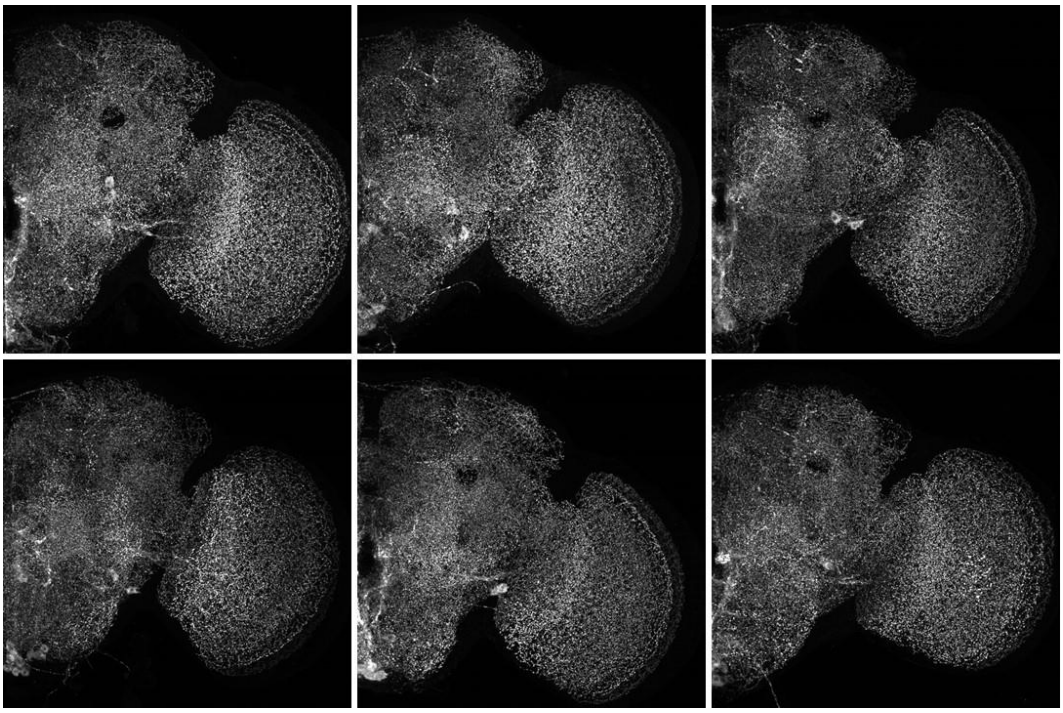

b. Kir2.1

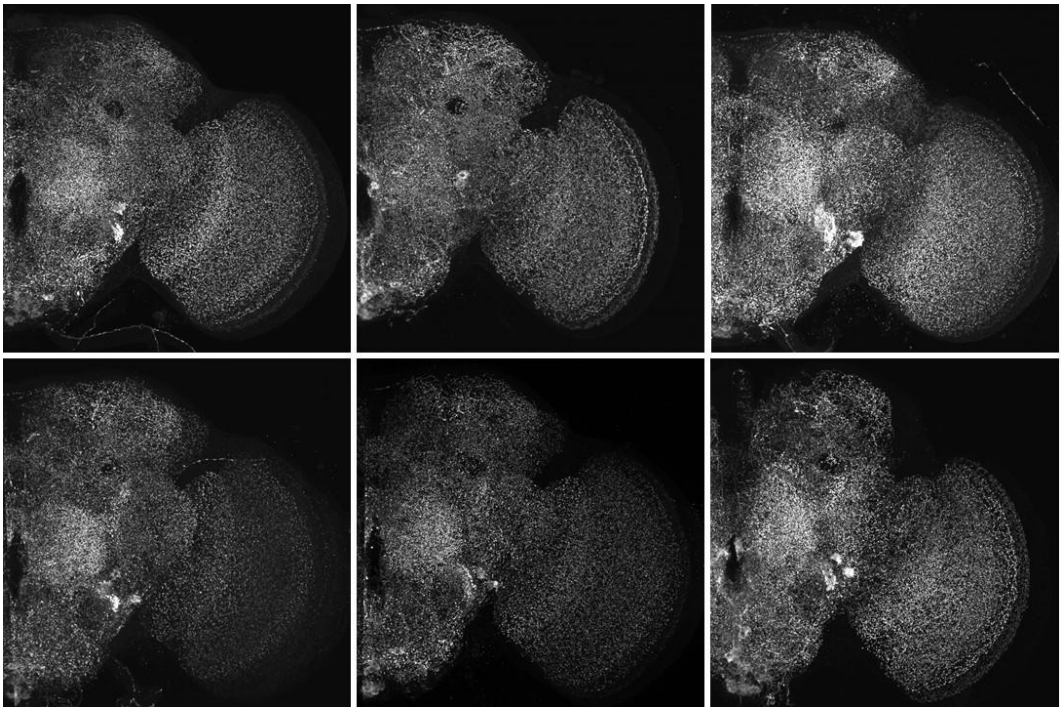

Figure 4.34. Comparison of pre-synaptic sites of octopaminergic neurons of 5 day old Drosophila melanogaster (experiment 2) for, (a) control (wild type, genotype 1.2) and, (b) kir2.1 (overexpressing of potassium channel, genotype 1.1).

a. Control

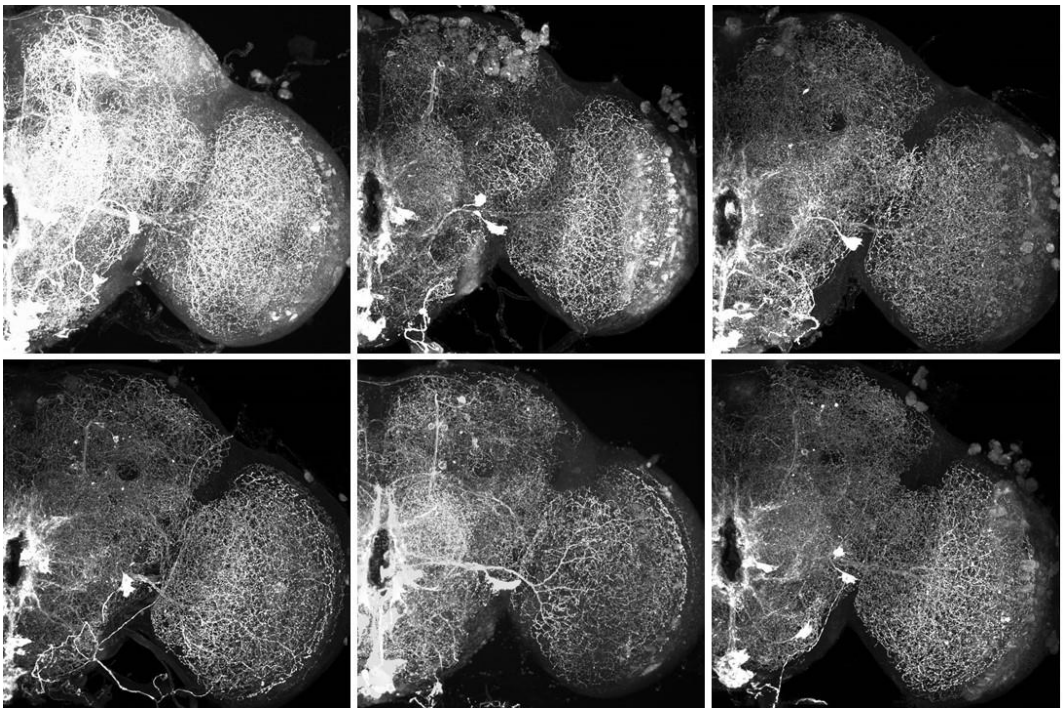

b. Kir2.1

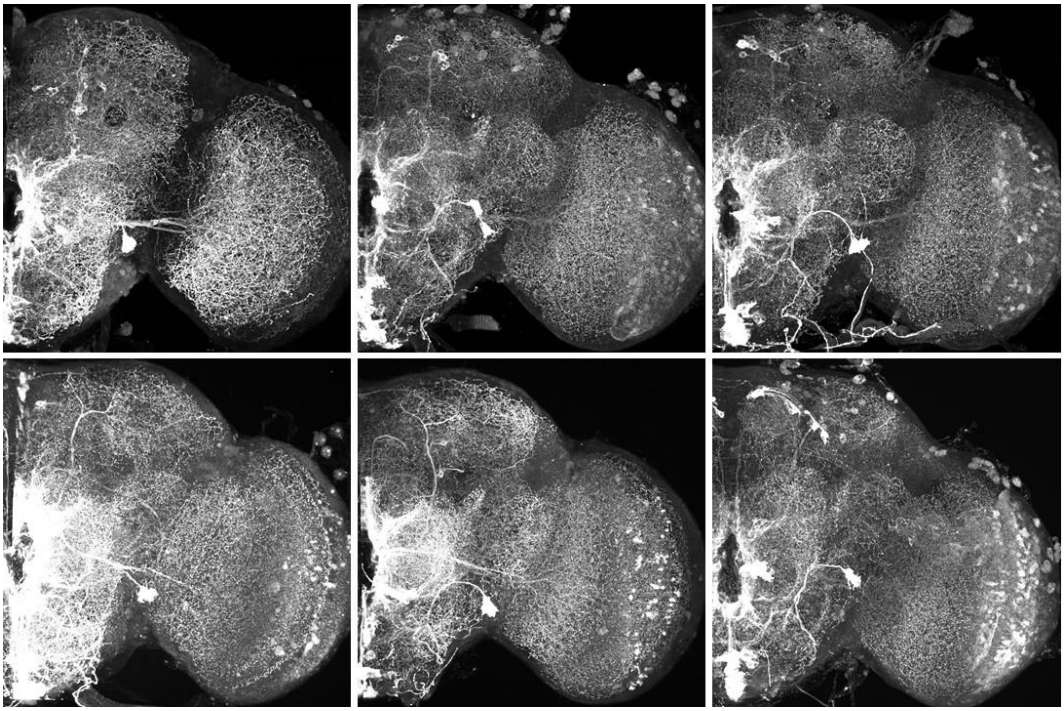

Figure 4.35. Comparison of octopaminergic neurons of 30 day old Drosophila melanogaster (experiment 2) for, (a) control (wild type, genotype 1.2 and, (b) kir2.1 (overexpressing of potassium channel, genotype 1.1).

a. Control

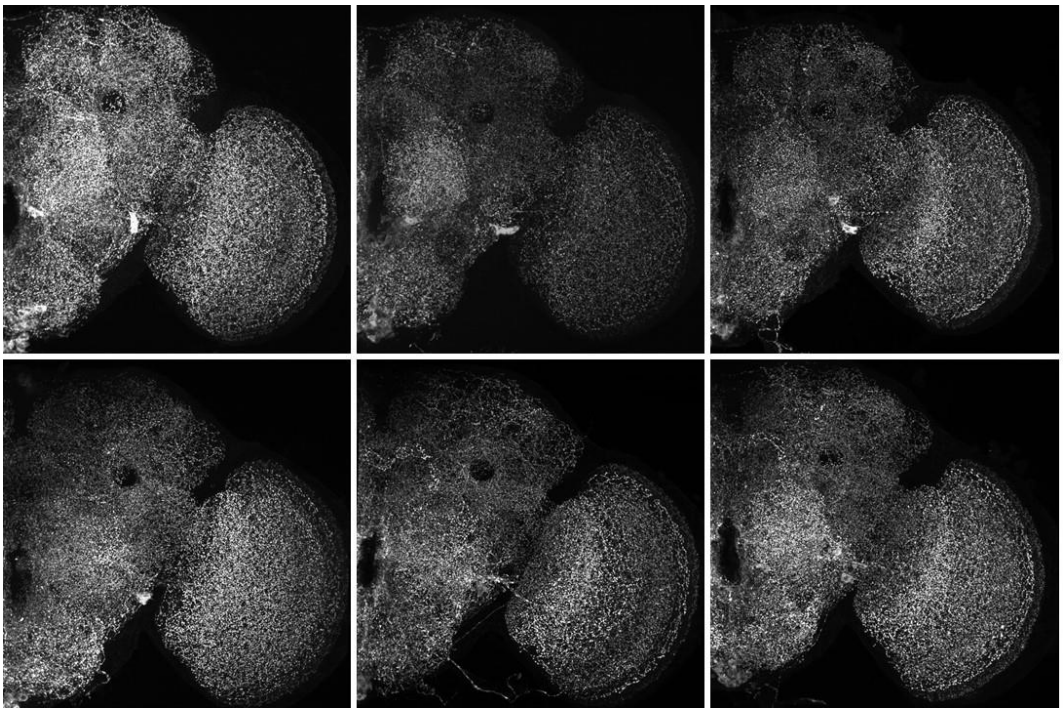

b. Kir2.1

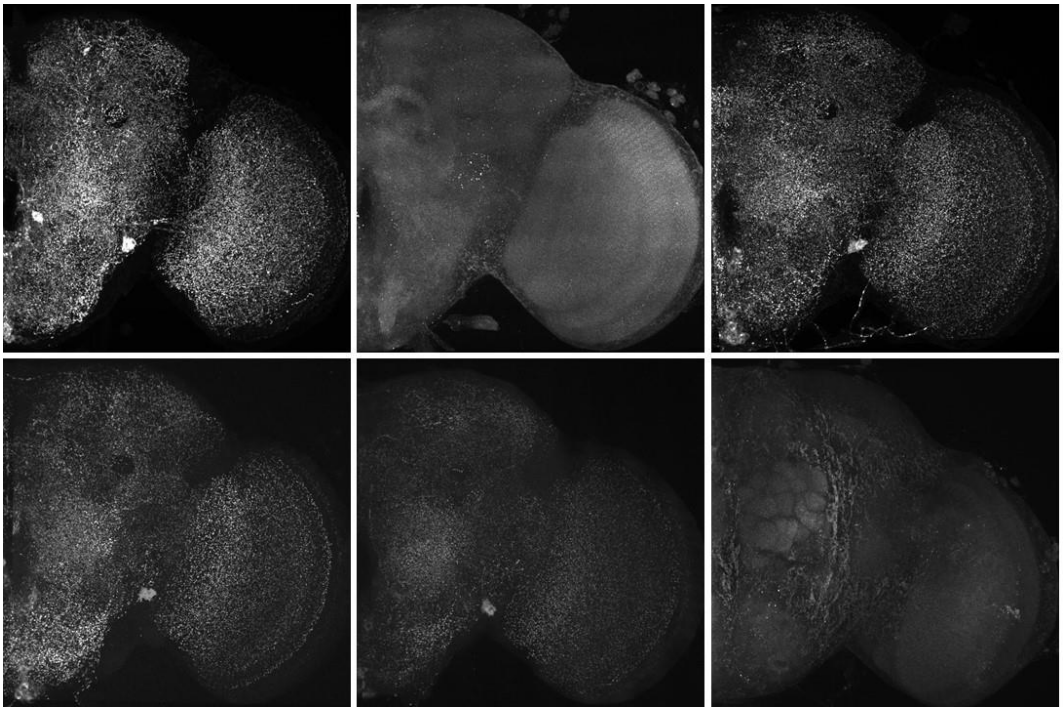

Figure 4.36. Comparison of pre-synaptic sites of octopaminergic neurons of 30 day old Drosophila melanogaster (experiment 2) for, (a) control (wild type, genotype 1.2) and, (b) kir2.1 (overexpressing of potassium channel, genotype 1.1).

a. Control

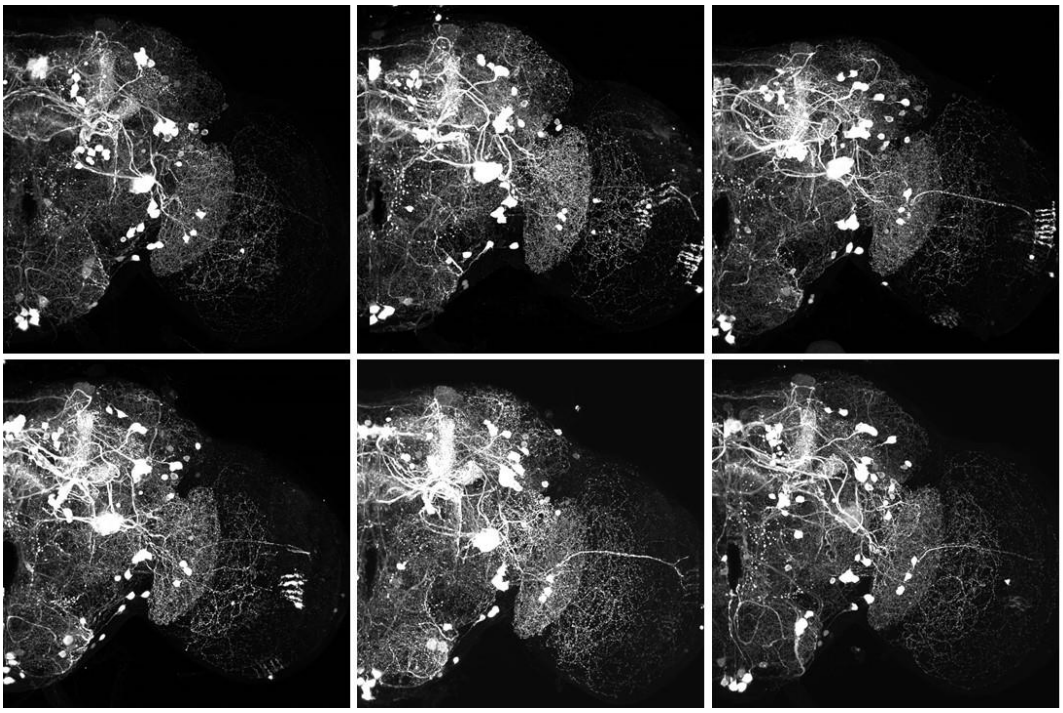

b. Kir2.1

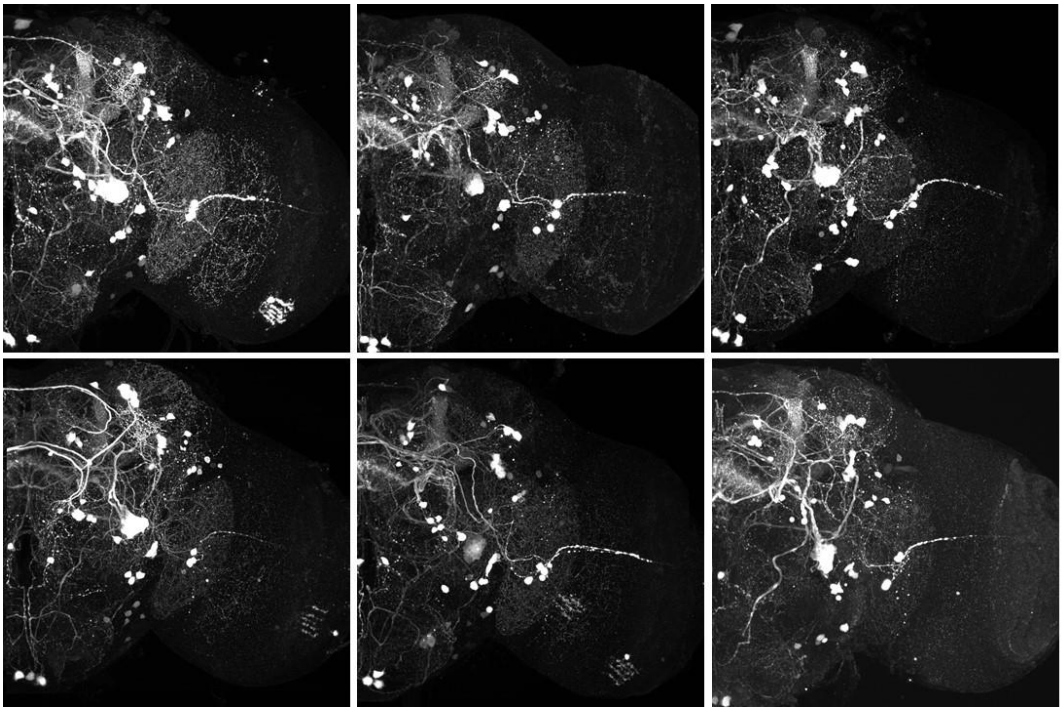

Figure 4.37. Comparison of dopaminergic neurons of 0 day old Drosophila melanogaster (experiment 2) for, (a) control (wild type, genotype 2.2 and, (b) kir2.1 (overexpressing of potassium channel, genotype 2.1).

a. Control

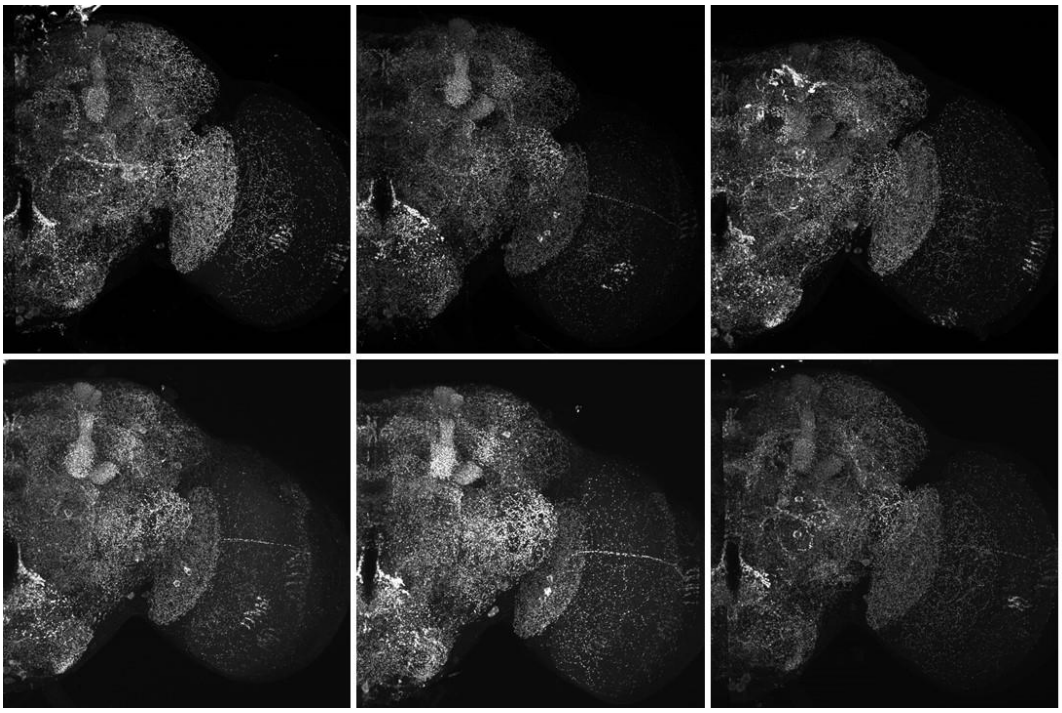

b. Kir2.1

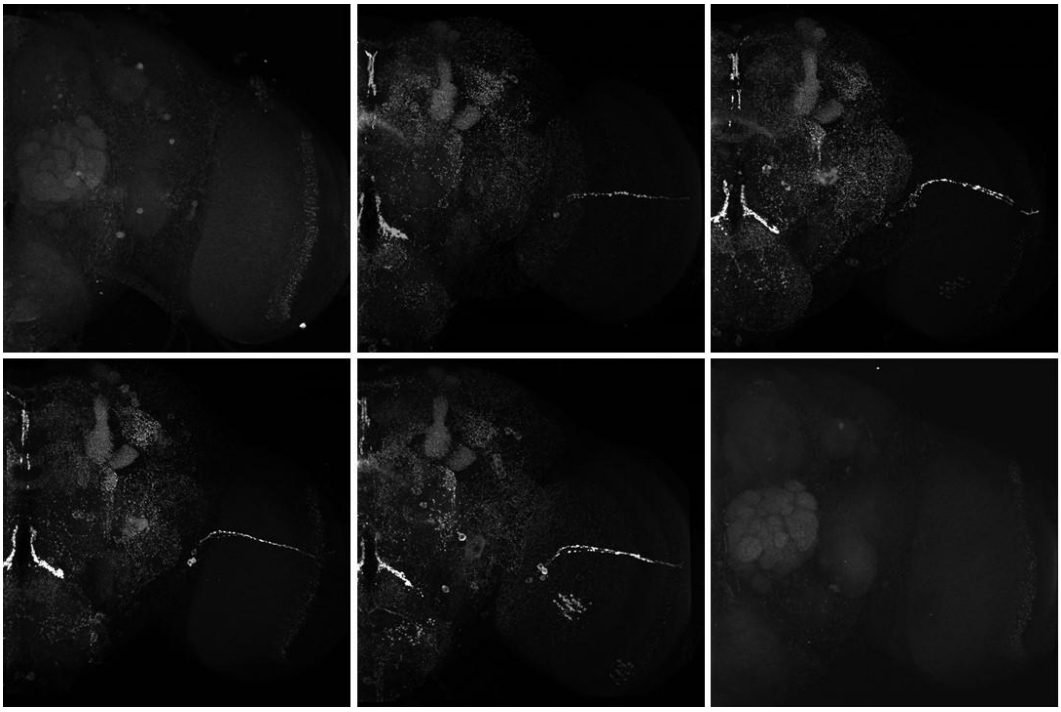

Figure 4.38. Comparison of pre-synaptic sites of dopaminergic neurons of 0 day old Drosophila melanogaster (experiment 2) for, (a) control (wild type, genotype 2.2) and, (b) kir2.1 (overexpressing of potassium channel, genotype 2.1).

a. Control

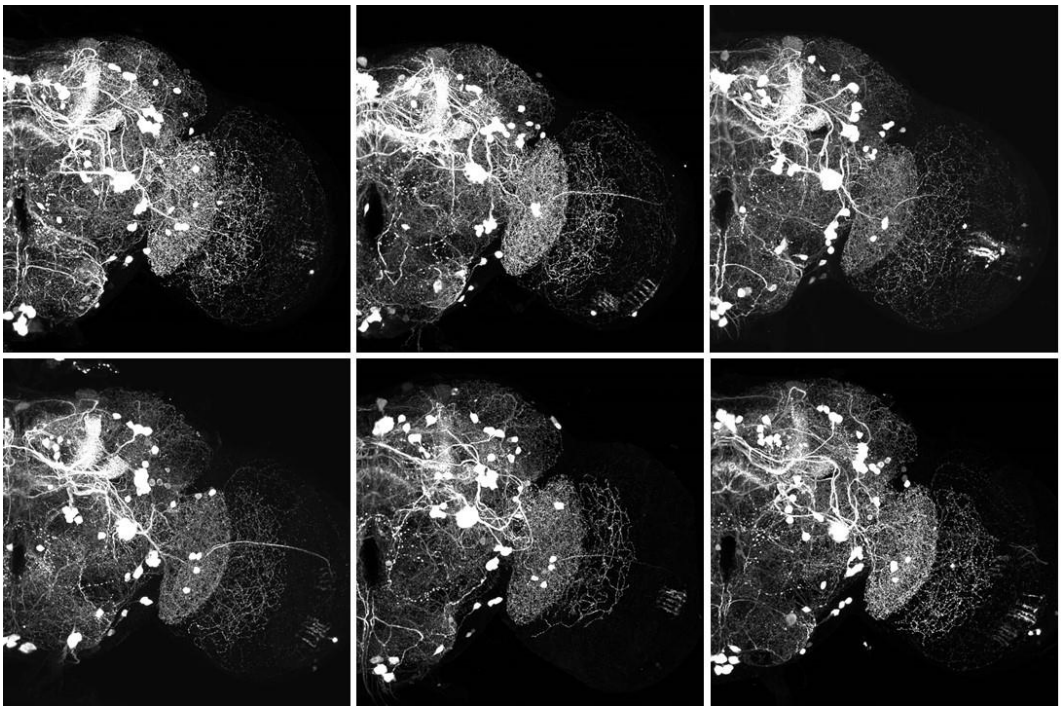

b. Kir2.1

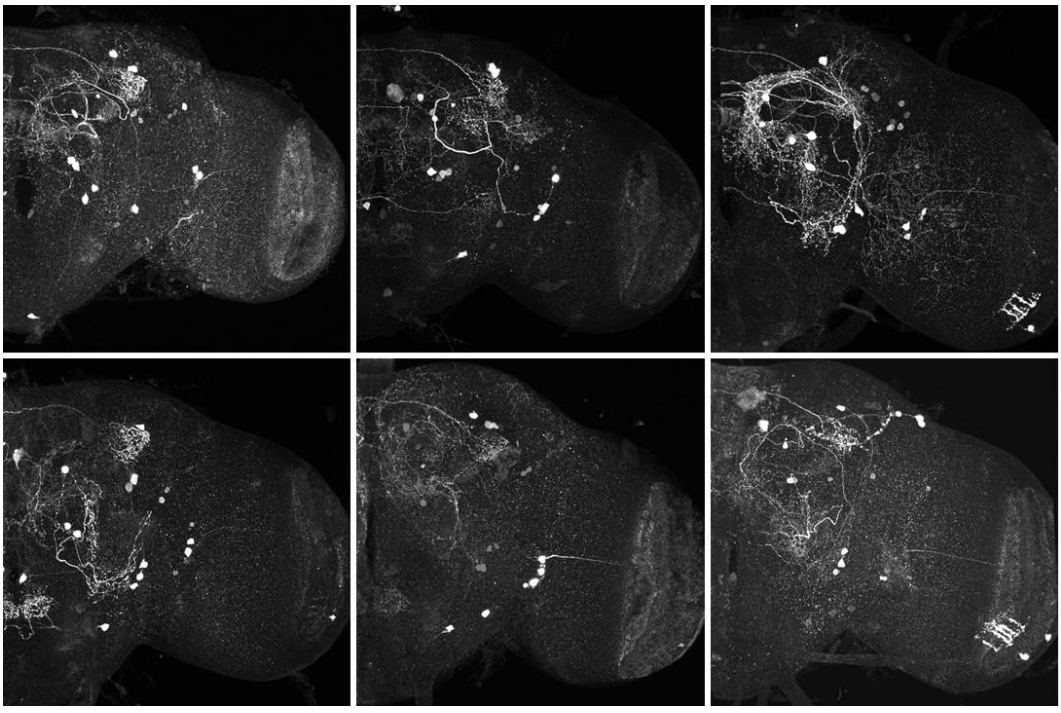

Figure 4.39. Comparison of dopaminergic neurons of 5 day old Drosophila melanogaster (experiment 2) for, (a) control (wild type, genotype 2.2 and, (b) kir2.1 (overexpressing of potassium channel, genotype 2.1).

a. Control

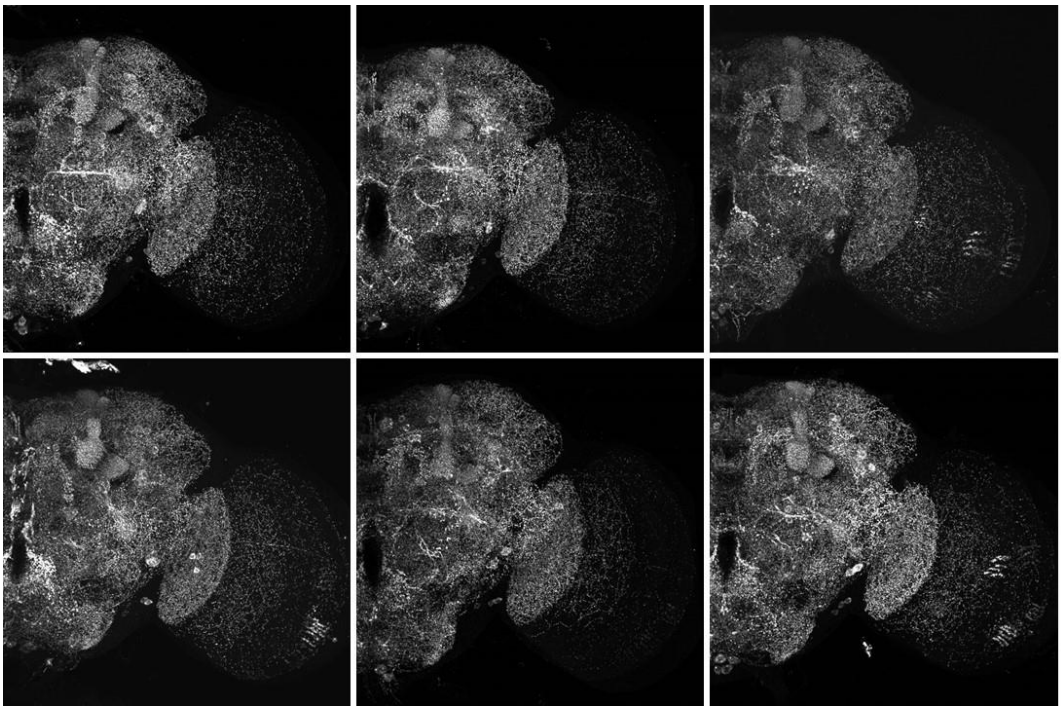

b. Kir2.1

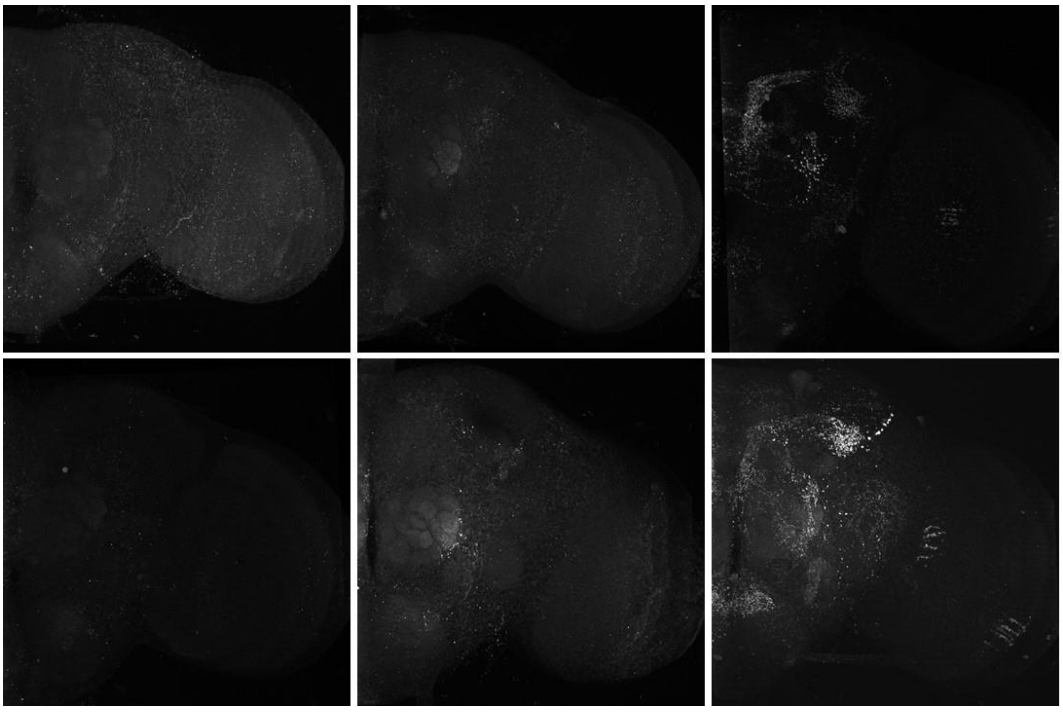

Figure 4.40. Comparison of pre-synaptic sites of dopaminergic neurons of 5 day old Drosophila melanogaster (experiment 2) for, (a) control (wild type, genotype 2.2) and, (b) kir2.1 (overexpressing of potassium channel, genotype 2.1).

Table 4.1 Rotation parameters after registration of the simulated data

a: Conversion matrix (substack size 800 x 800 x 250 voxels, Initial substack tilt Rx = 1°, Ry = 2°, and Rz = 5°, after single iteration):

0.9955825655501388 | 0.08765056866153828 | -0.03262316976298832

-0.08711895143914962 | 0.9957863605004061 | 0.023091300973873324

0.03532588980227439 | -0.02226238860907968 | 0.9997414741550107

Rx = -1.2757°, Ry = -2.0232°, Rz = -5.0010°

b: Registration results after different number of iterations (substack size 800 x 800 x 250 voxels, i.e., overlap: 200 voxels)

	Euler angles:			Rotation error:			Total	Total
	Rx	Ry	Rz	ΔRx%	ΔRy%	ΔRz%	rotation error	translation error
Substack tilt	1°	2°	5°					(1 voxel = 0.2 µm)
After single iteration	-1.2757°	-2.0232°	-5.0010°	27.566%	1.160%	0.019%	27.590%	1.898 voxels
After 2 iterations	-0.9957°	-1.9853°	-4.9998°	0.428%	0.734%	0.004%	0.850%	1.292 voxels
After 3 iterations	-0.9914°	-1.9908°	-5.0043°	0.855%	0.461%	0.085%	0.975%	1.243 voxels
After 4 iterations	-0.9902°	-1.9865°	-5.0015°	0.976%	0.674%	0.030%	1.186%	1.221 voxels
After 5 iterations	-0.9927°	-1.9888°	-5.0004°	0.733%	0.560%	-0.009%	0.922%	0.928 voxels

*Total rotation error = sqrt ($\Delta Rx^2+\Delta Ry^2+\Delta Rz^2$), Total translation error = sqrt ($\Delta x^2+\Delta y^2+\Delta z^2$)

c: Registration results for different amount of overlap (Results after 2 iterations)

		Euler angles:			Rotation error:			Total	Total
Substack size		overlap	Rx	Ry	ΔRz	ΔRx%	ΔRy%	rotation error	translation error
Substack tilt		1°	2°	5°					(1 voxel = 0.2 µm)
800 x 800 x 250	200 voxels	-0.9957°	-1.9853°	-4.9998°	0.428%	0.734%	0.004%	0.850%	1.292 voxels
800 x 800 x 225	150 voxels	-1.0029°	-1.9854°	-4.9982°	0.292%	0.730%	0.036%	0.787%	1.867 voxels
800 x 800 x 200	100 voxels	-1.0259°	-1.9925°	-5.0006°	2.594%	0.377%	0.012%	2.621%	2.895 voxels
800 x 800 x 175	50 voxels	-1.0122°	-2.0001°	-5.0106°	1.218%	0.007%	0.213%	1.237%	3.884 voxels

Table 4.2 Comparison of registration error between two overlap detection algorithms for increasing tilting angles. (Rx = 5-20°, with Ry = -2° and Rz = 5°, substack size: 800 x 800 x 250 voxel. Partial MIP size is set at 20 slices. Computation time was measured with a PC with a 6-core 3.4GHz Core i7-4930k CPU.)

a: Slice-by slice overlap detection

		Euler angles:			Rotation error:			Total	Total	Computation
Rotation	Overlap	Rx	Ry	Rz	ΔRx%	ΔRy%	ΔRz%	rotation error	translation error	time
Substack tilt			-2°	5°					(1 voxel = 0.2 µm)	
Rx = 5°	151	-4.9982°	2.0036°	-4.9997°	0.036%	0.180%	0.007%	0.184%	2.388 voxels	71 min
Rx = 10°	114	-9.9916°	2.0113°	-5.0008°	0.084%	0. 566%	0.017%	0.572%	4.501 voxels	53 min
Rx = 15°	78	-14.9879°	2.0017°	-5.0023°	0.081%	0.086%	0.046%	0.126%	6.543 voxels	45 min
Rx = 20°	49	-18.7297°	-1.6189°	-4.9692°	6.352%	19.055%	0.616%	20.095%	12.137 voxels	37 min

b: Block-by-block overlap detection

		Euler angles:			Rotation error:			Total	Total	Computation
Rotation	Split	Rx	Ry	Rz	ΔRx%	ΔRy%	ΔRz%	rotation error	translation error	time
Substack tilt			-2°	5°					(1 voxel = 0.2 µm)	
Rx = 5°	5	-4.9994°	2.0025°	-4.9976°	0.012%	0.126%	0.049%	0.136%	2.385 voxels	40min
Rx = 10°	5	-9.9910°	2.0071°	-4.9952°	0.090%	0.356%	0.095%	0.480%	4.463 voxels	26 min
Rx = 15°	5	-14.9757°	2.0025°	-5.0040°	0.162%	0.125%	0.079%	0.220%	6.658 voxels	23 min
Rx = 20°	5	-168.251°	-1.2440°	-5.4408°	741.26%	37.80%	8.816%	742.3%	16124 voxels	10 min
Rx = 20°	2	88.9337°	58.6556°	-88.4876°	544.669%	2832.8%	1669.8%	3333.1%	368420 voxels	11 min
Rx = 20°	1	-19.9362°	2.0025°	-5.0121°	0.319%	0.126%	0.242%	0.420%	8.784 voxels	33 min

Table 4.3 Error on angles computation and running time of the block-by-block algorithm for different splitting parameters with Rx = 5°, Ry = -2° and Rz = 5°. Partial MIP size is set at 20 slices.

		Computation	Euler angles:			Rotation error:			Total	Total
Split	#comparison	time	Rx	Ry	Rz	ΔRx%	ΔRy%	ΔRz%	rotation error	translation error
1 *	1	58 min	-4.9969°	2.0032°	-4.9977°	0.061%	0.162%	0.046%	0.180%	2.386 voxels
2	15	35 min	-4.9970°	2.0006°	-5.0017°	0.061%	0.031%	0.034%	0.076%	2.447 voxels
5	17	40 min	-4.9994°	2.0025°	-4.9976°	0.012%	0.126%	0.049%	0.136%	2.385 voxels
10	22	44 min	-4.9986°	2.0004°	-4.9988°	0.028%	0.023%	0.024%	0.042%	2.408 voxels
15	31	46 min	-4.9918°	1.9994°	-5.0015°	0.164%	0.028%	0.030%	0.169%	2.388 voxels
20	32	48 min	-4.9993°	2.0054°	-5.0017°	0.013%	0.271%	0.033%	0.273%	2.490 voxels
50	55	60 min	-4.9984°	2.0032°	-4.9983°	0.032%	0.160%	0.035%	0.167%	2.377 voxels
125	125	76 min	-4.9980°	2.0040°	-4.9985°	0.040%	0.199%	0.029%	0.205%	2.420 voxels
250 **	250	71 min	-4.9982°	2.0036°	-4.9997°	0.036%	0.180%	0.007%	0.184%	2.388 voxels

* No split **Effectively the same as slice-by-slice comparison

Table 4.6 Summary of the qualitative and quantitative analysis of dopaminergic and octopaminergic neurons for the fruit fly Drosophila melanogaster

		Octopaminergic neurons		Dopaminergic neurons	
Experiment 1: age-dependent analysis	**Fibers**	Aspect similar between young and old flies		Aspect similar between young and old flies	
	Pre-synaptic sites	No differences between young and old flies		No differences between young and old flies	
		5 day-old flies	**30 day-old flies**	**0 day-old flies**	**5 day-old flies**
Experiment 2: activity-dependent analysis	**Behavior**	Normal	- No climbing, flying and jumping - Shaking legs	- No climbing, flying and jumping - Shaking legs	- No climbing, flying and jumping - Shaking legs - Flies die
	Fibers	Aspect similar between Kir2.1 and control	- Aspect similar between Kir2.1 and control - Degeneration signs	Degeneration of thin fibers	- Degeneration of thin fibers complete - Thick fibers broken
	Pre-synaptic sites	No differences between Kir2.1 and control	20% decrease in Kir2.1 compared to the control	Important decrease in Kir2.1 compared to the control	Important decrease in Kir2.1 compared to the control

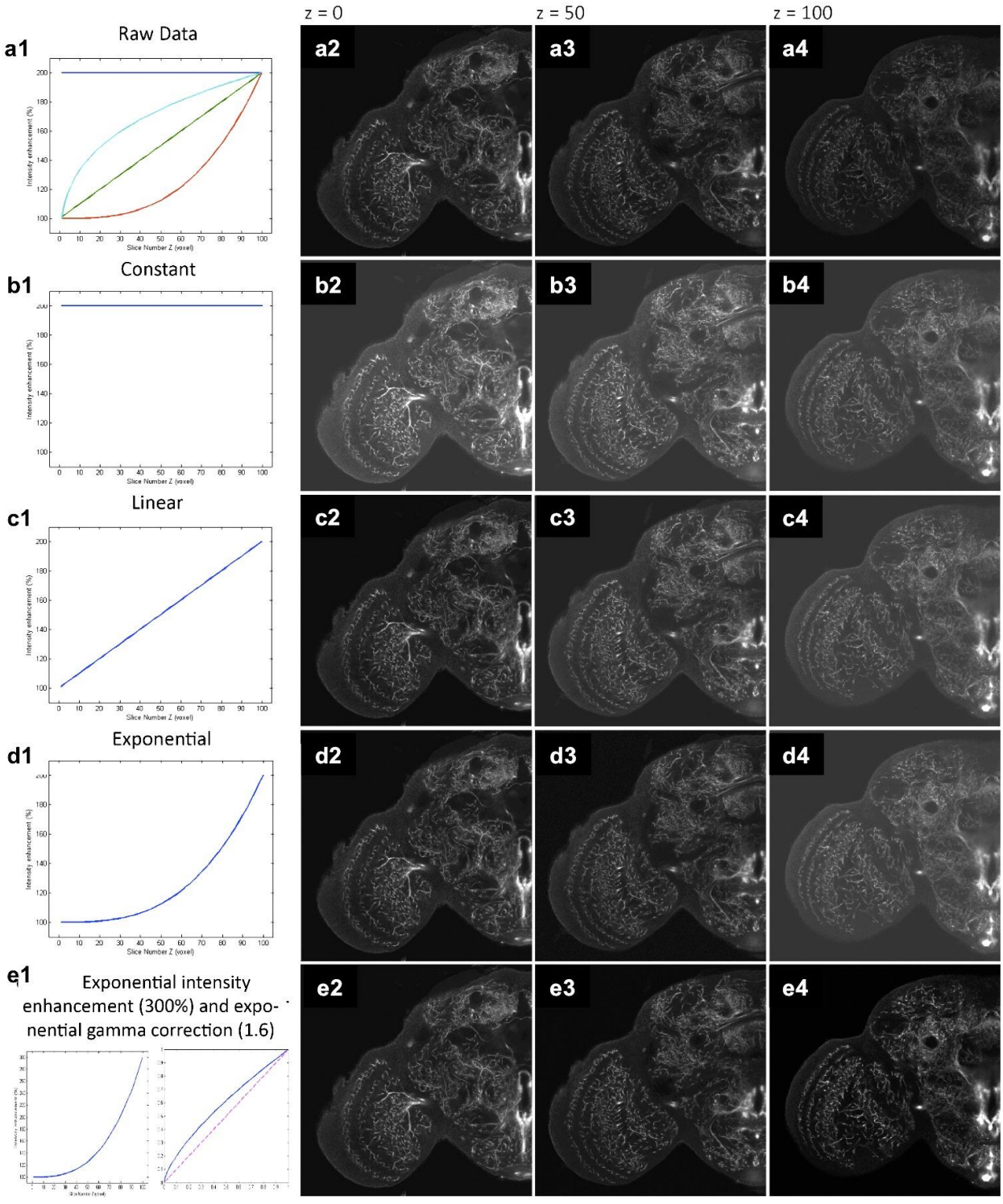

Figure 5.13. Progressive intensity and gamma correction throughout the image stack. Example of a 100-section stack of the Drosophila brain. (a1) Summary of the different enhancement curves available in the plugin. (a2-4) First (a2), middle (a3) and last (a4) sections of the original data. Sections deep in the sample (a3, a4) progressively lose intensity and contrast. (b1) Correction curve of the constant enhancement. (b2-4) Results of constant intensity

enhancement. Intensity of the last section (b4) is enhanced by 200 % to match the intensity as that of the first section of the original data (a2). Because of constant enhancement, the first section (b2) now appears too bright. (c1) Correction curve of linear enhancement. (c2-4) Results of linear intensity enhancement. By applying different levels of intensity enhancement, the first (c2) and last (c4) section has similar brightness. However, in the case of this sample, brightness of the middle section (c3) still appears different. (d1) Correction curve of exponential enhancement. (d2-4) Results of exponential intensity enhancement. By adjusting the levels of enhancement in intermediate sections, brightness of all the sections are adjusted to be almost identical. (e1) Gamma correction curve (e2-4) Results of gamma correction. Gamma correction changes the contrast of the image by adjusting the brightness of the mid tone voxels without changing the intensity of the darkest and brightest voxels. Progressive levels of Gamma correction can also be applied if needed.

Chloé Murtin

May 2016